

INFORMATION TO USERS

This was produced from a copy of a document sent to us for microfilming. While the most advanced technological means to photograph and reproduce this document have been used, the quality is heavily dependent upon the quality of the material submitted.

The following explanation of techniques is provided to help you understand markings or notations which may appear on this reproduction.

1. The sign or "target" for pages apparently lacking from the document photographed is "Missing Page(s)". If it was possible to obtain the missing page(s) or section, they are spliced into the film along with adjacent pages. This may have necessitated cutting through an image and duplicating adjacent pages to assure you of complete continuity.
2. When an image on the film is obliterated with a round black mark it is an indication that the film inspector noticed either blurred copy because of movement during exposure, or duplicate copy. Unless we meant to delete copyrighted materials that should not have been filmed, you will find a good image of the page in the adjacent frame.
3. When a map, drawing or chart, etc., is part of the material being photographed the photographer has followed a definite method in "sectioning" the material. It is customary to begin filming at the upper left hand corner of a large sheet and to continue from left to right in equal sections with small overlaps. If necessary, sectioning is continued again—beginning below the first row and continuing on until complete.
4. For any illustrations that cannot be reproduced satisfactorily by xerography, photographic prints can be purchased at additional cost and tipped into your xerographic copy. Requests can be made to our Dissertations Customer Services Department.
5. Some pages in any document may have indistinct print. In all cases we have filmed the best available copy.

University
Microfilms
International

300 N. ZEEB ROAD, ANN ARBOR, MI 48106
18 BEDFORD ROW, LONDON WC1R 4EJ, ENGLAND

8115163

TULYATHAN, PRAVIT

MOMENT METHOD SOLUTIONS FOR RADIATION AND SCATTERING
FROM ARBITRARILY SHAPED SURFACES

The Ohio State University

PH.D. 1981

**University
Microfilms
International** 300 N. Zeeb Road, Ann Arbor, MI 48106

**MOMENT METHOD SOLUTIONS FOR RADIATION AND SCATTERING
FROM ARBITRARILY SHAPED SURFACES**

A Dissertation

**Presented in Partial Fulfillment of the Requirements for
the Degree Doctor of Philosophy in the Graduate
School of The Ohio State University**

by

Pravit Tulyathan, M.S.E.E.

The Ohio State University

1981

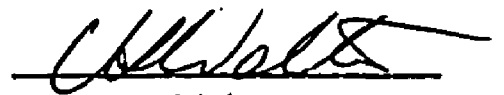
Reading Committee:

Professor C.H. Walter

Professor J.H. Richmond

Professor W.D. Burnside

Approved by



Adviser

**Department of Electrical
Engineering**

ACKNOWLEDGMENTS

The author wishes to express his sincere gratitude to his graduate adviser, Professor C.H. (Buck) Walter. Special thanks to Dr. E.H. Newman for the experience of working with him throughout this course of this work. Gratitude is also owed to Professor Richmond for his contributions and many suggestions. Thanks to those mentioned above and Professor W.D. Burnside for their critical reading of this manuscript.

The work reported in this dissertation was supported, in part, by Contract N00014-78-C-0049 between the Department of the Navy, Office of Naval Research, Arlington, Virginia, and The Ohio State University Research Foundation.

VITA

November 11, 1951	Born: Bangkok, Thailand
1973	B.E.E., Georgia Institute of Technology, Atlanta, Georgia
1974 - present	Graduate Research Associate, ElectroScience Laboratory, The Ohio State University
1976	M.S.E.E., The Ohio State University, Columbus, Ohio

Publications

- E.H. Newman and P. Tulyathan, "Wire Antennas in the Presence of a Dielectric/Ferrite Inhomogeneity," IEEE-AP-26, July 1978, pp. 587-593.
- P. Tulyathan and E.H. Newman, "The Circumferential Variation of the Axial Component of Current in Closely Spaced Thin-Wire Antennas," IEEE-AP-27, January 1979, pp. 46-50.

Fields of Study

Electromagnetic Theory, Professor R.G. Kouyoumjian
Antenna Theory, Professor C.H. Walter
Communication Theory, Professor C.E. Warren
Mathematics, Professor J.T. Scheick
Numerical Analysis, Professor H.H. Mei

TABLE OF CONTENTS

	<u>Page</u>
ACKNOWLEDGMENTS	ii
VITA	iii
LIST OF TABLES	vi
LIST OF FIGURES	vii
Chapter	
I INTRODUCTION	1
II FORMULATION OF THE PROBLEM	4
A. The Reaction Formulation	4
B. Choice of Test Modes	8
C. Expansion/Testing Functions	9
1. Thin-wire Mode	9
2. Surface-patch Mode	9
3. Attachment Mode	11
4. Plate Overlap Mode	13
D. Computation of Impedance Elements	13
III AUTOMATIC GENERATION OF THE SURFACE-PATCH MODE LAYOUT	18
A. Introduction	18
B. Gordon-Hall Procedure	19
1. The Quadrilateral	21
2. The Ellipse	23
C. Subdivision Method 1	26
D. Subdivision Method 2	32
IV NUMERICAL RESULTS	37
A. Monopole Antenna on a Disk	37
B. Scattering from Polygonal Plates	40
1. Circular Disks	40
2. Triangles	40
3. Fin-shaped Plate	49
V ANALYSIS OF MICROSTRIP ANTENNAS	58
A. Introduction	58

	<u>Page</u>
B. The Model	61
1. Air Dielectric Microstrip	61
2. Modification for Dielectric Slab	63
3. Expansion and Test Modes	70
4. Numerical Difficulties	70
C. Numerical Results	75
D. Discussion	79
 VI CONCLUSION	 81
 BIBLIOGRAPHY	 82
 APPENDIX A: Efficient Evaluation of PWS Filament-to-Filament Impedance	 87
 APPENDIX B: Evaluation of R by the Method of Dielectric Images	 91
 APPENDIX C: Basic Approaches Used in Subdivision Methods 1 and 2	 95

LIST OF TABLES

Table		<u>Page</u>
1	ELEMENTS IN THE FREE SPACE LOSSLESS MICROSTRIP IMPEDANCE MATRIX	73
2	ELEMENTS IN MICROSTRIP IMPEDANCE MATRIX INCLUDING DIELECTRIC SLAB (LOSSLESS CASE)	74

LIST OF FIGURES

Figure	<u>Page</u>
1 The scatterers in an impressed field generated by the source $(\underline{J}_i, \underline{M}_i)$	5
2 Surface currents $(\underline{J}_s, \underline{M}_s)$ are placed on S without changing the exterior fields, but making fields interior to S vanish	5
3 The exterior scattered fields generated by $(\underline{J}_s, \underline{M}_s)$	7
4 Thin-wire V-dipole	10
5 PWS surface-patch V-dipole	10
6 Attachment dipole	12
7 The reactance of two rectangular PWS surface-patch monopoles	15
8 The reactance of two closely spaced non-parallel PWS filaments	17
9 The Gordon-Hall domains	20
10 A quadrilateral region R in the x - y plane	22
11 The curvilinear coordinates formed by the G-H Procedure for the quadrilateral in Figure 10	24
12 The curvilinear coordinates formed inside a triangular region by the G-H Procedure	25
13 An elliptical region R in the x - y plane	25
14 The curvilinear coordinate system induced by the transfinite mapping \underline{U}	27
15 A mesh for the overlapping surface-patch dipole modes	27
16 A set of overlapping surface-patch dipole modes formed inside a fin-shaped polygon by using subdivision method 1	29

	<u>Page</u>
17 A situation in which the side AE cannot be the reference side	30
18 A set of overlapping surface-patch dipole modes formed inside a regular octagon by using subdivision method 1	31
19 Subdivision of a rectangular strip	33
20 Subdivision of a trapezoidal strip	33
21 Subdivision of a trapezoidal strip with rectangular sections in the middle part of the strip	34
22 Subdivision of a trapezoidal strip with very long end sections (AD and AD')	34
23 A set of overlapping surface-patch dipole modes formed inside a fin-shaped polygon by using subdivision method 2	35
24 Resistance of a monopole antenna at the center of a disk in free space	38
25 Reactance of a monopole antenna at the center of a disk in free space	39
26 Normal incidence, backscatter from disks	41
27 Backscatter from disk with $A/\lambda = 1.2$	42
28 Backscatter from disk with $A/\lambda = 1.2$	43
29 Normal incidence, bistatic scatter from disk with $A/\lambda = 1.2$	44
30 Normal incidence, bistatic scatter from disk with $A/\lambda = 1.2$	45
31 Backscatter from a $3-\lambda$ right angle triangle (θ -polarization)	46
32 Backscatter from a $3-\lambda$ right angle triangle (ϕ -polarization)	47
33 Backscatter from a $3-\lambda$ right angle triangle (θ -polarization) in the elevation plane	48
34 A set of overlapping surface-patch modes formed in a $3-\lambda$ right angle triangle by using subdivision method 2	50

	<u>Page</u>
35 A set of overlapping surface-patch modes formed in a $3\text{-}\lambda$ right angle triangle by using the Gordon-Hall procedure	51
36 Backscatter from a 30° isosceles triangle with the height of 3.25λ (θ -polarization)	52
37 Backscatter from a 30° isosceles triangle with the height of 3.25λ (ϕ -polarization)	53
38 A set of overlapping surface-patch dipole modes formed in a 30° isosceles triangle by using subdivision method 2	54
39 A set of overlapping surface-patch dipole modes formed inside a $3\text{-}\lambda$ fin-shaped polygon by using subdivision method 2	55
40 Backscatter from a $3\text{-}\lambda$ fin-shaped plate (θ -polarization)	56
41 Backscatter from a $3\text{-}\lambda$ fin-shaped plate (ϕ -polarization)	57
42 Perspective view of a microstrip antenna fed by microstrip transmission line	59
43 Side view of a microstrip antenna fed by coaxial line	59
44 Side view of an air dielectric microstrip antenna fed by coaxial line	62
45 The model for the air dielectric microstrip antenna	62
46 The voltage generator in Figure 45 is replaced by 1-amp impressed current filament	64
47 Microstrip antenna with dielectric slab	64
48 The dielectric slab is modelled by equivalent volume polarization current	65
49 \underline{J}_n in the presence of the dielectric slab	67
50 Relative D_z field along the line $x = 3.75$ cm. and $y = 0$	69
51 Input impedance of rectangular microstrip antenna	72
52 Input impedance of trapezoidal microstrip antenna	76

	<u>Page</u>	
53	Input impedance of rectangular microstrip antenna	77
54	Input impedance of almost square microstrip antenna	78
55	Reactance of two PWS filamentary monopoles	88
56	The geometry used to find the smallest distance between two filaments	89
57	A line charge, Q , with the associated coordinates	92
58	The images of a charge, Q , located near a dielectric slab	94
59	Overlapping surface-patch dipole layout on a rectangular plate	96
60	A rectangle divided into strips	96
61	A rectangle divided into strips and then into blocks	97

CHAPTER I

INTRODUCTION

This dissertation deals with the use of quadrilateral surface-patch currents in the moment method solution of antenna and/or scattering problems. Wires and wire/plate attachments are also considered here. One of the goals in this work is to develop a general purpose computer code which can solve near- as well as far-zone parameters of arbitrarily shaped antennas/scatterers accurately.

The basic formulation of the problem is in terms of an integral equation where the unknowns are the surface currents. Here, Rumsey's Reaction Integral Equation (RIE) [1], which is a general form of the electric field (EFIE) and magnetic field (MFIE) integral equation [2], is used. The choice of electric test source (used in this work) reduces the RIE to the EFIE which is applicable to closed bodies as well as open bodies, such as infinitely thin plates and wires. On the other hand, if magnetic test sources are used, then the RIE reduces to the MFIE. Although the MFIE is only applicable to closed bodies, it is much simpler to implement.

Considerable work on the thin-wire formulation resulted in many useful and versatile computer codes [3, 4, and 5]. These codes are ideal for thin-wire problems and can be used to model solid surfaces by representing them in terms of a wire-grid. Richmond [6] was the first to show the usefulness of the wire-grid models for scattering from planar as well as three-dimensional objects. Numerous work on this subject followed as summarized in [7]. The advantage of wire-grid modelling is its ability to treat solid objects with sharp edges, corners, and thin-wire appendages. However, the wire-grid model has to be constructed with care in order to have the minimum number of unknown wire currents, to accurately represent the physical object; yet not violate the assumptions of the thin-wire approximation. Another disadvantage of the wire-grid modelling is that it may not reliably predict accurate near-zone parameters such as surface currents and impedances.

Early work on surface-patch modelling was done using the MFIE to solve closed surface scatterers. Oshiro [8] used a pulse basis function and point matching approach to solve the MFIE for various well defined three-dimensional objects. This method was extended for arbitrarily shaped surfaces by Knepp and Goldhirsh [9] through the use of non-planar cells. In their work, nine points on the body were used to

find the directions of the two tangential surface current expansions for each cell. Albertsen, et al., [10] allowed wire attachments to a closed body by applying the MFIE for the body and the EFIE with the thin-wire approximation for the wires. Planar quadrilateral patches were used to simulate the body along with pulse basis functions with point matching to represent the surface currents. Special considerations were also given to the surface-patches on which wires are attached. Based on this wire/closed body formulation, the user-oriented Numerical Electromagnetic Code (NEC) was developed by Burke and Poggio [11] for solving electromagnetic problems involved with wires/closed bodies. In this code, the user specifies the shape of the body by first dividing it into surface-patches. The area, x-y-z coordinates of the center, and the unit normal vector of each patch are then entered as inputs into the computer code. Recently, J.J.H. Wang [12] used the planar triangular patches along with the MFIE to solve the scattering problem of closed bodies. The basis function is related to the incident field by the physical-optics current technique. Consequently, the moment method impedance matrix is dependent on the incident field.

N.N. Wang, et al., [13] employed the RIE (using electric test source) along with rectangular sinusoidal surface-patch basis function and Galerkin's method to solve for the currents and scattering parameters of planar and non-planar surfaces. Sankar and Tong [14] used the finite element approach, where the equation for the surface currents is made stationary with respect to the set of trial functions (similar to Galerkin's method for EFIE). The planar triangular patch has been used because of formulation ease and better representation of arbitrary surfaces. Planar triangular patches were also used in the EFIE formulation by Wilton, et al., [15]. Again, pulse basis function and point matching were used in the moment method solution. Newman and Pozar [16] modelled composite wire and surface geometries by using sinusoidal rectangular surface-patch, thin-wires, and wire/plate expansion modes. Galerkin's method was used to solve the RIE (with electric test source) for far- as well as near-zone parameters such as surface currents and impedances. The rectangular sinusoidal surface-patch was extended to quadrilateral and triangular surface-patches by Singh and Adams [17].

The basic formulation in this work parallels much of the work done by Newman and Pozar [16], except that quadrilateral surface-patches are now used. Attention is also given to the problem of automatically generating the surface-patch modes on a given polygonal plate. One of the goals in this work is to produce a user-oriented computer code for electromagnetic problems dealing with plates and/or wires. The general idea is to let the user model a solid object by a series of connecting plates, and only the coordinates of the plate corners are needed to specify the plates. The automatic generation of surface-patch modes by the code will greatly reduce the amount of input data required. It should be noted that the basic surface-patch dipole can be either a planar or a non-planar V-dipole which can be used to model any arbitrary three-dimensional surface.

Chapter Two presents the reaction formulation for the moment method solution of composite surface/wire geometries. The wire, plates, wire/plate attachment, and plate overlap modes are defined. Techniques for accurate and efficient evaluations of the mutual impedances are discussed.

Chapter Three describes the method for automatically generating surface-patch modes for a given polygonal plate. Criteria that must be satisfied in order to have a set of surface-patch modes which satisfy the current conditions on the plates are listed. In addition, the geometric features of the surface-patch which will allow efficient evaluation of the impedance matrix are described. A standard subdivision technique, as well as two other algorithms for automatic surface-patch mode generation, are presented.

Chapter Four shows the results obtained by using the subdivision methods presented in Chapter Three for different polygonal plates. Both input impedance and backscatter data are compared with other independent calculations and measurements.

Chapter Five describes the use of the moment method to analyze the microstrip antenna. The microstrip patch is modelled by the surface-patch mode and the dielectric is modelled by volume polarization currents. The volume polarization currents are related to the surface current by the boundary condition at the conductor and dielectric interface. This results in having the surface currents as unknowns and the dielectric is taken into account by a modification of the free-space impedance matrix. Calculations are made for many patch geometries and the results are compared with measurements and calculations by other investigators.

Chapter Six is the conclusion and includes suggestions of related topics for further research.

CHAPTER II

FORMULATION OF THE PROBLEM

In this chapter, the electromagnetic scattering or antenna problem is formulated in terms of a surface integral equation based on the reaction concept [1]. The unknown is the surface current which can be calculated using the moment method. The surface structure of the antenna or scatterer is modelled by a combination of plates and thin wires. Thus, the surface currents can be represented by a finite series with three basis functions: surface dipole modes, wire dipole modes, and wire-to-surface attachment modes.

A. The Reaction Formulation

The use of the reaction concept to derive an integral equation which describes the electromagnetic fields in an antenna or scattering problem has been presented by Richmond [19], Wang, et al., [13] and Newman and Pozar [16], but is included here for completeness. The distinction between an antenna and scattering problem is that when the source is located on or near the object, it is considered as an antenna problem and when the source is distant from the object, it is viewed as a scattering problem. Both cases can be considered at once by analyzing the objects in an impressed field generated by the source ($\underline{J}_i, \underline{M}_i$). The problem is depicted in Figure 1, where the objects can be arbitrary closed or open surface and wire structures, and a wire may contact a surface.

Let S denote the surface enclosing the bodies, and \hat{n} be the unit outward normal to S . In the presence of the bodies, the sources ($\underline{J}_i, \underline{M}_i$) generate the fields ($\underline{E}, \underline{H}$). These fields are considered to be time harmonic, and the time dependence $e^{j\omega t}$ is suppressed. From the surface-equivalence theorem of Schelkunoff [18], the field interior to the surface S will vanish without changing the exterior field if the surface current densities

$$\underline{J}_s = \hat{n} \times \underline{H} \quad (1)$$

$$\underline{M}_s = \underline{E} \times \hat{n} \quad (2)$$

are introduced on the surface S , as shown in Figure 2. The null field condition inside the bodies allows the bodies to be replaced by the ambient medium without altering the field anywhere.

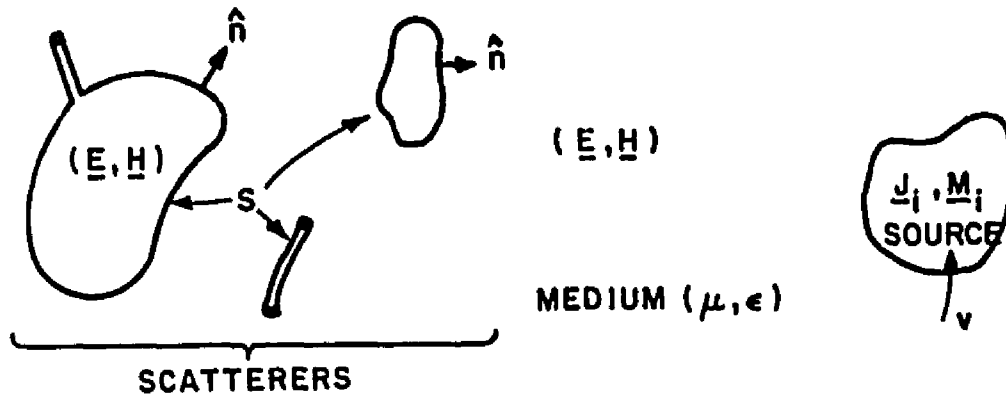


Figure 1. The scatterers in an impressed field generated by the source $(\underline{J}_1, \underline{M}_1)$.

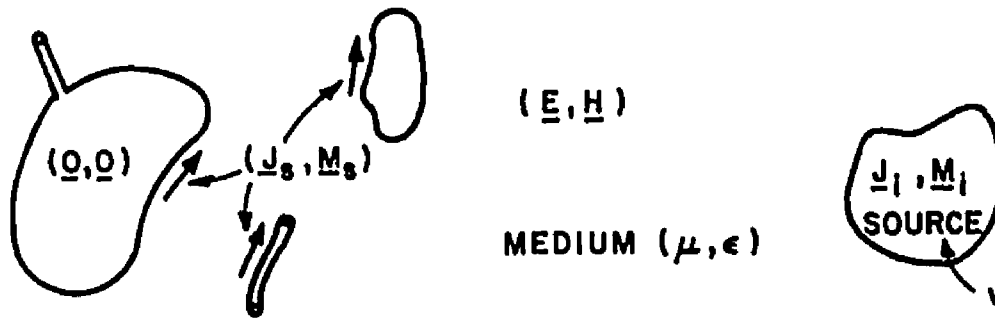


Figure 2. Surface currents $(\underline{J}_S, \underline{M}_S)$ are placed on S without changing the exterior fields, but making fields interior to S vanish.

If $(\underline{J}_i, \underline{M}_i)$ generate the incident fields $(\underline{E}_i, \underline{H}_i)$ in the ambient medium (μ, ϵ) , then the scattered fields can be defined as

$$\underline{E}_s = \underline{E} - \underline{E}_i \quad (3)$$

$$\underline{H}_s = \underline{H} - \underline{H}_i \quad (4)$$

The scattered field is radiated by the surface currents $(\underline{J}_s, \underline{M}_s)$ in the ambient medium (Figure 3). This definition allows the total fields $(\underline{E}, \underline{H})$ to be a sum of the incident fields $(\underline{E}_i, \underline{H}_i)$ and the scattered fields $(\underline{E}_s, \underline{H}_s)$.

A test source $(\underline{J}_m, \underline{M}_m)$ is now introduced interior to S to form a reaction 1 with the existing fields $(\underline{E}, \underline{H})$. Since the total fields inside the surface S are zero, the reaction of the test sources and the field

$$\oint_S (\underline{J}_m \cdot \underline{E}_s - \underline{M}_m \cdot \underline{H}_s) ds + \oint_S (\underline{J}_m \cdot \underline{E}_i - \underline{M}_m \cdot \underline{H}_i) ds = 0. \quad (5)$$

Let the fields radiated by $(\underline{J}_m, \underline{M}_m)$ in the ambient medium be $(\underline{E}_m, \underline{H}_m)$. By the reciprocity theorem, (5) can also be written as

$$\oint_S (\underline{J}_s \cdot \underline{E}_m - \underline{M}_s \cdot \underline{H}_m) ds + \iiint_V (\underline{J}_i \cdot \underline{E}_m - \underline{M}_i \cdot \underline{H}_m) dV = 0 \quad (6)$$

$$\oint_S (\underline{J}_s \cdot \underline{E}_m - \underline{M}_s \cdot \underline{H}_m) ds + \iiint_V (\underline{J}_i \cdot \underline{E}_m - \underline{M}_i \cdot \underline{H}_m) dV = 0 \quad (6)$$

where V is the volume occupied by the impressed sources $(\underline{J}_i, \underline{M}_i)$. Equations (5) and (6) are different forms of the reaction integral equation (RIE) developed by Rumsey [1]. Equation (6) was applied by Richmond [3 and 5] for his thin wire analysis. The RIE is a general integral equation describing the electromagnetic fields. If only electric current test sources are used, Equation (6) reduces to the widely known EFIE and the use of only magnetic test sources will reduce Equation (6) into the MFIE [2]. In this work, only the electric test sources are used. The bodies are considered to be perfectly conducting and $\underline{M}_s = 0$.

Although Equation (6) was derived with the assumption that all surfaces were closed so that Schekunoff's surface equivalence theorem [18] can be used, it can also be applied for open surfaces. In the case of an infinitely thin flat plate, \underline{J}_s is the vector sum of the current on the top and bottom surfaces if electric test sources are used [20].

The following shows how Equation (6) is solved by the moment method. The unknown current \underline{J}_s is expanded in terms of a set of N basis (expansion) functions, F_n :

$$\underline{J}_s = \sum_{n=1}^N I_n F_n, \quad (7)$$

and Equation (6) is enforced for N electric test sources placed in S. Thus, Equation (6) reduces to a set of simultaneous linear equations:

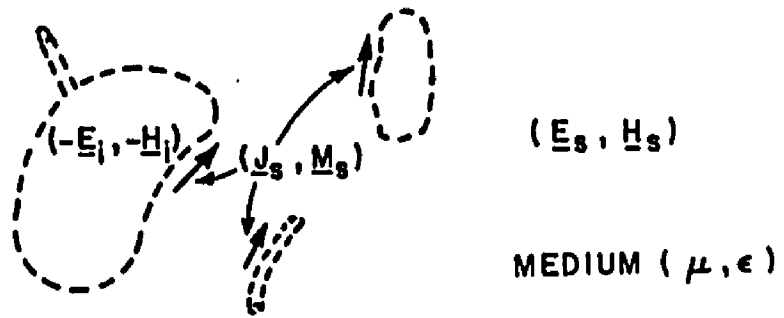


Figure 3. The exterior scattered fields generated by $(\underline{J}_s, \underline{M}_s)$.

$$\sum_{n=1}^N I_n z_{mn} = V_m ; \quad m = 1, 2 \dots N \quad (8)$$

where

$$z_{mn} = - \iint_n \underline{E}_m \cdot \underline{F}_n \, ds \quad (9)$$

$$V_m = \iiint_V (\underline{J}_1 \cdot \underline{E}_m - \underline{M}_1 \cdot \underline{H}_m) \, dv. \quad (10)$$

The integration in Equation (9) is over the surface of the n^{th} expansion mode.

B. Choice of Test Modes

The choice of the testing functions is dictated by several factors including: computation time for the mutual impedances, convergence rate, and the degree of accuracy required for the final result. Obviously, the choice of a delta function (point-matching) over the full surface test function will significantly reduce the computation time. In this work, the testing functions are chosen to be the same as the expansion functions (Galerkin's method) for the following reasons:

- a. Galerkin's method will result in a symmetric impedance matrix. Thus, only half of the impedance elements, i.e. the lower triangular matrix (L), are calculated and stored. Also, solving for the unknowns (by the standard Crout decomposition) with the triangular matrix (L) is faster than with the full impedance matrix.
- b. It is felt that Galerkin's method will result in a versatile and general computer code. Thus, backscatter, as well as numerically difficult antenna problems, can be solved by the same general purpose computer code. In particular, when considering the point-matching technique for a wire attached to a plate, the solution could be overly sensitive to the proximity of the attachment point and the match point. However, experience with rectangular surface patch modes [16] indicated that, with surface testing, the attachment point may be anywhere in the surface patch grid.
- c. Galerkin's method will ordinarily converge faster than point matching. Thus, for a given surface patch grid, the result obtained by Galerkin's method will be closer to convergence

than with point matching. This also implies that a smaller number of unknowns is required for a given problem.

C. Expansion/Testing Functions

In order to model a geometry with thin-wires, flat surfaces, and wire-surface connections, three basic types of modes (wire dipole modes, surface dipole modes, and the wire-surface attachment modes) are used. Singly curved surfaces can also be modelled using piecewise flat approximation. All of the modes will have a sinusoidal variation with free space wave number, k , in the direction of current flow.

1. Thin-wire Mode

The wire mode used is the piecewise-sinusoidal (PWS) V-dipole consisting of two sinusoidal monopoles developed for the thin-wire formulation by Richmond [19]. Figure 4 shows a V-dipole with a 180° internal angle lying on the z -axis. Using the thin-wire approximation, the current on this dipole is given by

$$\vec{J}_s^w = \frac{\hat{z}}{2\pi a} \left[P_1 \frac{\sin k(z-z_1)}{\sin k(z_2-z_1)} + P_2 \frac{\sin k(z_3-z)}{\sin k(z_3-z_2)} \right], \quad (11)$$

where P_1 and P_2 represent pulse functions with unit value when $z_1 < z < z_2$ and $z_2 < z < z_3$, respectively, and are zero elsewhere. Also, a is the wire radius and $k = 2\pi/\lambda$. These modes are placed in an overlapping array on the wire to ensure continuity of current on the wire. The advantage of PWS mode is that the near-zone fields and the mutual impedance, Z_{mn} , are known in closed form [22].

2. Surface-patch Mode

The general quadrilateral surface-patch mode is a surface V-dipole consisting of two quadrilateral piecewise-sinusoidal surface monopoles. A surface V-dipole with interior angle of 180° is shown in Figure 5. Consider some general point in monopole A (shown as the heavy dot in Figure 5), which has terminal length V and end length U . Construct a line through the point which intersects the end and terminal such that $u/v = U/V$. Let L be the length of this line and ℓ be the distance along the line from the end to the point. Then the surface current density on monopole A is

$$\vec{J}_A = \frac{C \sin k\ell}{W(\ell/L)} \hat{\ell} \quad (12)$$

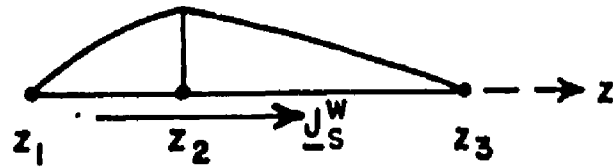


Figure 4. Thin-wire V-dipole.

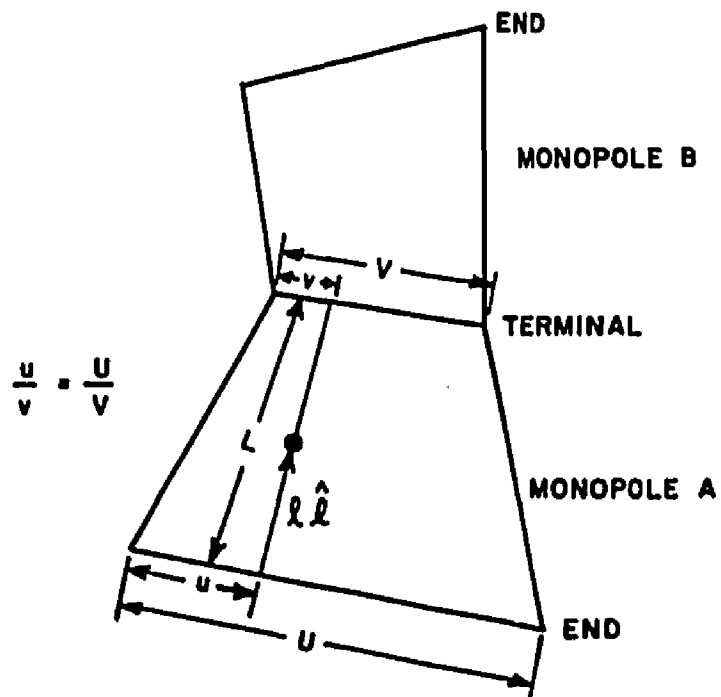


Figure 5. PWS surface-patch V-dipole.

where $W(\ell/L)$ is the local width of monopole A, and C is a normalizing constant such that the terminal current is one ampere. The surface current density on monopole B, \underline{J}_B , is defined in a similar way, but with the current flowing in the $-\ell$ direction. This mode is a generalization of the rectangular PWS surface-patch dipole used by Wang [13] as well as Newman and Pozar [16].

3. Attachment Mode

The attachment mode is used to establish continuity of current at the wire/surface junction and to ensure that, in the immediate vicinity of the attachment, the surface current density has the proper $\hat{\rho}$ polarization and $1/\rho$ dependence. This mode consists of two parts: a wire monopole and a disk monopole, as shown in Figure 6. The wire monopole current density is similar to the thin wire monopole mode:

$$\underline{J}_S^W = \frac{1}{2\pi a} \frac{\sin k(z_2-z)}{\sin kz_2} \hat{z}. \quad (13)$$

The disk current density is

$$\underline{J}_S^D = \frac{-\sin k(b-\rho)}{2\pi\rho \sin k(b-a)} \hat{\rho}, \quad a \leq \rho < b, \quad (14)$$

where a, b are the inner and outer radii of the annulus, respectively. Note that the total current on the disk at $\rho=a$ is equal to the total current on the wire segment at $z=0$ insuring continuity of current at the attachment. Also, observe that the $\sin k(b-\rho)$ function in the numerator of Equation (14) forces the disk current to be zero at the disk edge, $\rho=b$. It is this property which allows the disk to be placed on the surface and still maintain continuity of current on the surface. The $\sin k(b-\rho)$ function was chosen (rather than, say, $b-\rho$ or $\sin(b-\rho)$) since this permits the fields of the disk to be obtained with only one numerical integration.

The attachment mode is used by placing it directly over the surface-patch modes where the wire meets the surface. There is no special way in which the disk must be situated with respect to the surface-patch modes; that is, the disk may be centered at midpoints, corners, or other points on the surface-patch modes. The only restriction is that the attachment point be at least 0.1λ from the edges of plates. The outer radius of the disk mode, b , should be in the range from about 0.1λ to 0.25λ [16].

For antennas, feeds may be placed at the endpoints of any wire segment including the attachment segment. For example, the feed of a monopole on a finite ground plane may be modelled by inserting a generator at the base of the monopole between the attachment mode

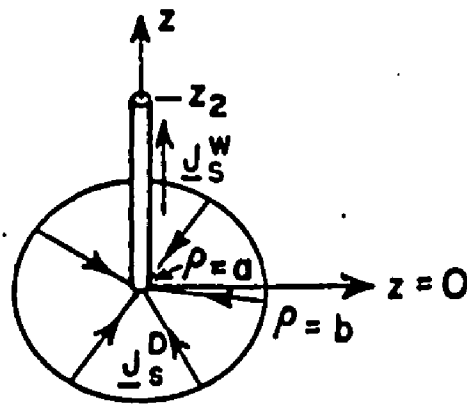


Figure 6. Attachment dipole.

wire and disk monopole. Delta-gap feed is used in this work, although a magnetic frill model could also be used.

4. Plate Overlap Mode

The overlap modes allow a non-zero continuous current at the plate-to-plate junction. They are identical to the surface-patch dipole mode discussed earlier. The edges of the overlap surface dipoles need not coincide with the edges of the surface dipole modes on either plate, thus allowing the intersection of plates of different sizes.

D. Computation of Impedance Elements

Many computationally efficient techniques developed for the evaluation of the mutual impedances associated with rectangular surface-patches [21] can also be used for the quadrilateral surface-patches. This section will discuss these techniques and how they are used in finding the mutual impedances of quadrilateral surface-patches. The majority of the mutual impedances are either the surface-to-surface dipole or disk-to-surface dipole impedances. The disk-to-surface dipole impedance is calculated in the same way as described in reference [21]. The surface-to-surface dipole impedance is discussed below.

The general expression for the impedance matrix element given in Equation (9) is evaluated numerically by considering the surface-dipole modes as made up of PWS filaments. The surface-to-surface dipole impedance is a sum of four surface-patch monopole-to-monopole impedances, i.e.

$$z_{mn} = z^{t_A e_A} + z^{t_A e_B} + z^{t_B e_A} + z^{t_B e_B} \quad (15)$$

where the superscript t_A and e_A denote the test monopole A and expansion monopole B, respectively. Also, t_B and e_B are defined similarly. Each surface-patch monopole-to-monopole impedance is evaluated by summing up all the filament-to-filament impedances [21]. If the test and expansion surface monopoles are each represented by M filaments, then, in general, each monopole-to-monopole impedance requires M^2 evaluations of the filament-to-filament impedances. If both monopoles are rectangular, and if either the surface current directions are parallel or the vector transverse to the surface monopoles are parallel, then only 2M of these impedances are evaluated [21].

Most of the time spent in filling out the impedance matrix is used in finding the filament-to-filament impedances. Thus, computation time depends on the number of filaments used to represent a surface monopole. In evaluating the self impedance or mutual impedance of two closely spaced surface monopoles, experience has shown that a filament spacing of 0.07λ or about five filaments per 0.25λ wide surface

patch is adequate for representing the surface patch. More numerically difficult problems, such as finding near field quantities of an antenna, may require a slightly larger number of filaments usually no more than seven filaments per 0.25λ wide surface patch. Simpson's rule of integration is used to sum up the filament-to-filament impedances for a surface monopole-to-monopole impedance. Usually, when the monopoles do not intersect each other, a three-point Simpson's rule (or representing the surface patch by three filaments) is used. For surface monopoles spaced more than 0.25λ apart, a one-filament representation for each surface monopole is used. As an example, the reactance of two rectangular monopoles is plotted versus the separation distance, D , in Figure 7. Plotted are the exact reactance (solid line) and the reactance obtained by representing the surface monopole by one filament on the center of the monopole (dotted line). The difference of the two curves results from the phase and amplitude variations of the filament-to-filament impedance as the integration is done across the surface patches. These phase and amplitude variations can be approximated by $\left(\frac{e^{-jkR}}{R}\right)$ where R is the average distance of the two filaments. To obtain a more accurate result by the one-filament representation, $\left(\frac{e^{-jkR}}{R}\right)$ is used in the following manner. If z_{ff} is the filament-to-filament impedance, then the variation due to the n^{th} expansion surface-patch monopole is taken into account by:

$$z_{fn} = \frac{z_{ff} \operatorname{Re}^{jkR}}{6} \left(\frac{e^{-jkR_1}}{R_1} + \frac{4e^{-jkR}}{R} + \frac{e^{-jkR_2}}{R_2} \right) \quad (16)$$

where R_1 , R , and R_2 are the average distances from the test filament to the closer edge, center, and further edges of the surface-patch monopole. Similarly, the variation due to the m^{th} test surface-patch monopole is accounted for by:

$$z_{mn} = \frac{z_{fn} \operatorname{Re}^{jkR}}{6} \left(\frac{e^{-jkR_1}}{R_1} + \frac{4e^{-jkR}}{R} + \frac{e^{-jkR_2}}{R_2} \right) \quad (17)$$

The imaginary part of z_{mn} is plotted as dashed lines in Figure 7 and is very close to the accurate impedance value (solid line). The real part of z_{mn} also behaves in the same manner.

Another time-saving technique is the use of an equivalent reactance when two PWS filaments are very close to each other. This is used only when two surface-patches coincide or share a common side. The equivalent reactance is derived in the same manner as is done in reference [21]. The reactance of two closely spaced filaments can be written as

$$Y(x) = C_1 + C_2 \ln(x) \quad (18)$$

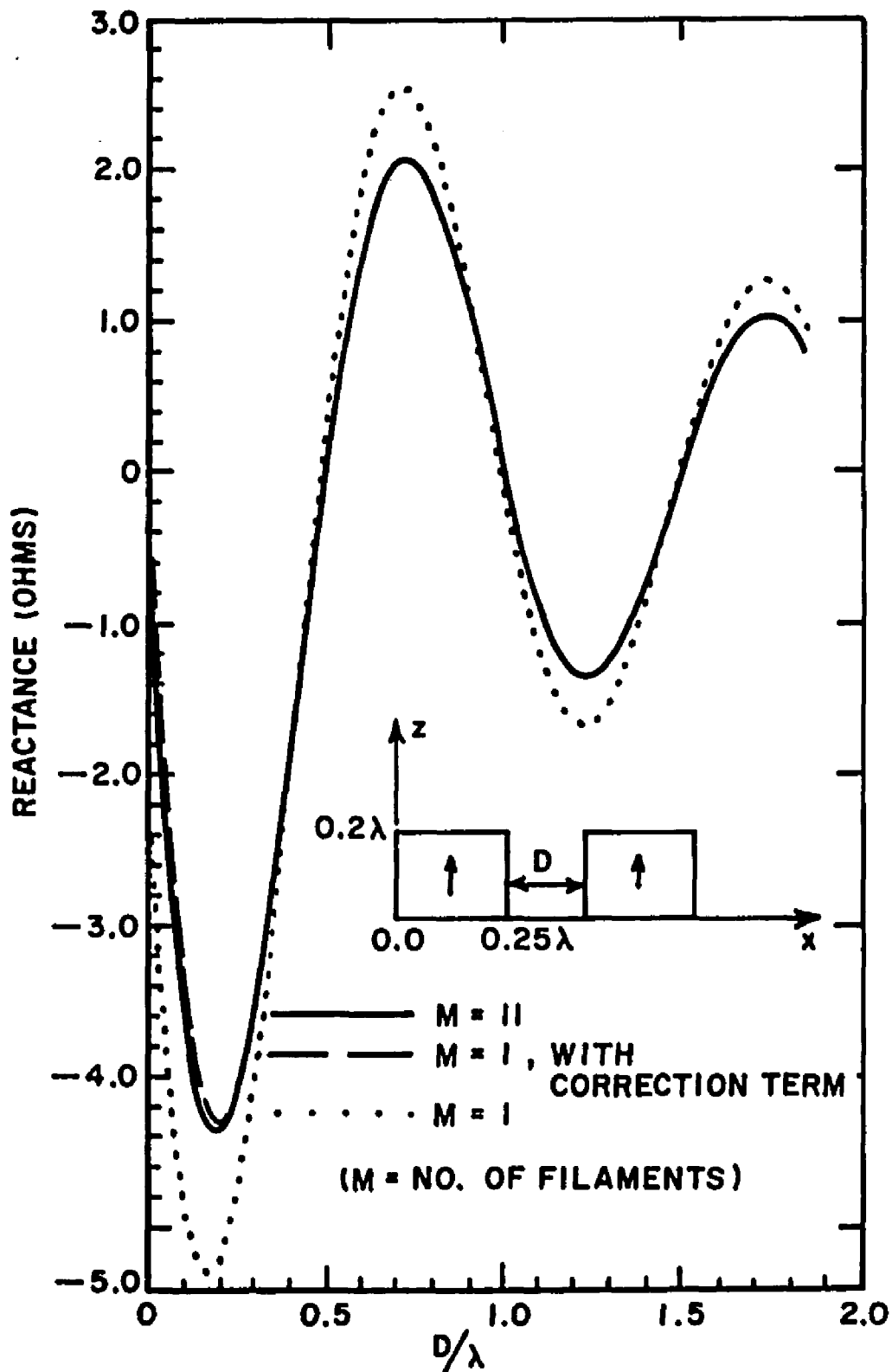


Figure 7. The reactance of two rectangular PWS surface-patch monopoles. M denotes the number of PWS filaments used to represent the surface patch.

where Y is the reactance and x is the separation distance. C_1 and C_2 are constants which can be evaluated by

$$C_2 = \frac{Y(\Delta x) - Y(\frac{\Delta x}{2})}{\ln(R)} \quad (19)$$

$$C_1 = Y(\Delta x) - C_2 \ln(\Delta x) \quad (20)$$

Equation (18) can be integrated analytically to give an equivalent reactance at $x=0$:

$$Y(0) = -Y(\Delta x) + 2C_1 + 2C_2 (\ln(\Delta x) - 1) \quad (21)$$

Although Equations (18) through (20) were derived for parallel filaments, it is also applicable to nonparallel filaments as shown in Figure 8. Using the equivalent reactance at $x=0$ (Equation 21) avoids the \ln -singularity and, thus, significantly increases the convergence rate [21].

Another factor to keep in mind when finding the PWS filament-to-filament impedance is whether to evaluate the closed form expression [22] or to use the less time consuming numerical integration. This problem is addressed in Appendix A.

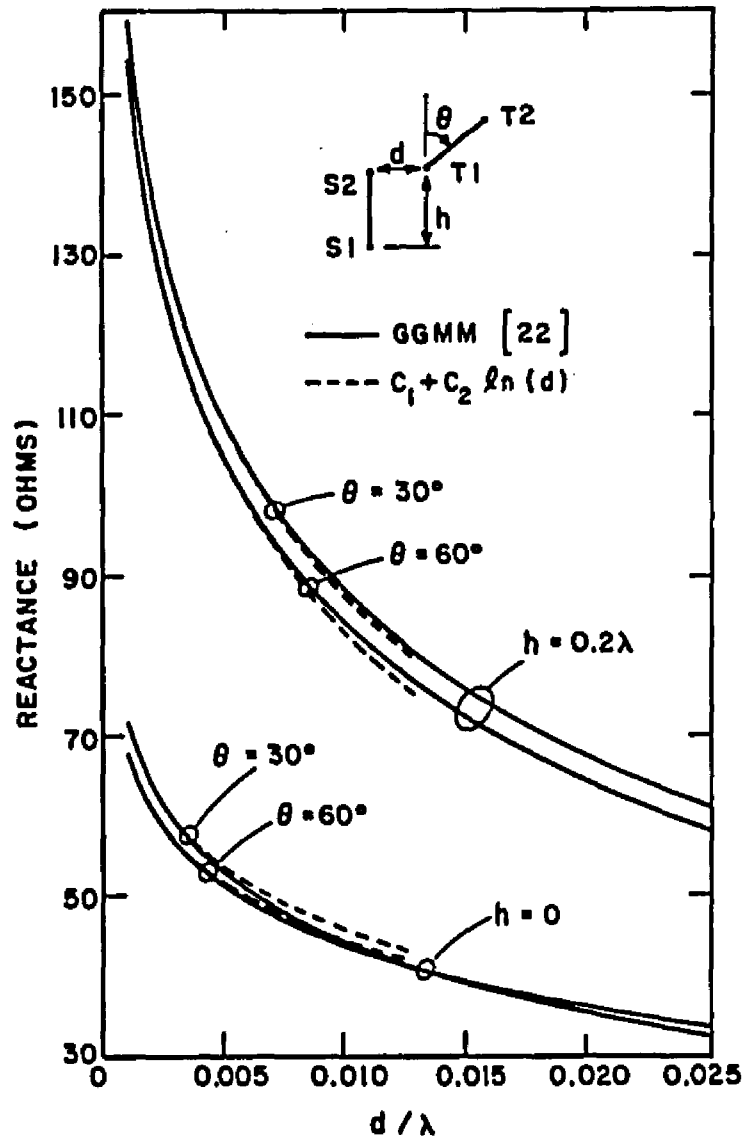


Figure 8. The reactance of two closely spaced non-parallel PWS filaments. The lengths of the filaments are 0.2λ . S1 and S2 denote the terminal and end points of the test monopole, respectively. T1 and T2 denote the terminal and end points of the expansion monopole, respectively.

CHAPTER III

AUTOMATIC GENERATION OF SURFACE PATCH MODE LAYOUT

The problem of setting up surface-patch modes over an arbitrary polygonal flat plate is considered in this chapter. Three different subdivision schemes are discussed. The first scheme is the Gordon-Hall (G-H) procedure [23], and the last two are procedures devised to achieve an optimal mode set-up by satisfying the criteria given in the next section. Examples are used to illustrate the applicability of each scheme.

A. Introduction

The set of coordinates describing all the surface dipole modes forms a large portion of the input data required for the moment method. Although coordinates for each mode can be manually entered into a moment method computer code, it is desirable that the mode set up be done automatically with the input being the geometry of the plates. A reasonable mode generation algorithm should minimize the user data input and be consistent with the following criteria:

- a. In general, there must be two orthogonal sets of surface dipole modes and their linear combination can approximate the actual plate current.
- b. At the edge of the plate, the component of current perpendicular to the edge must be zero and that parallel to the edge must be non-zero.
- c. The sides of modes at the boundary of the plate must match the curvature of the boundary adequately, especially on sharp bends.
- d. The size of most modes should be about the same as a specified nominal size and the length of each monopole should not exceed some maximum size.
- e. Where possible, the shape of the monopoles should be rectangular and the directions of currents in the majority of the modes should be parallel.

Criterion (a) is required for the solution to converge, while criterion (b) is a relaxed requirement of the edge condition [24]. This condition states that, in the vicinity close to the edge of an infinitely thin plate, the currents perpendicular and parallel to the edge have the asymptotic behaviors $\rho^{-1/2}$ and $\rho^{1/2}$, respectively, where ρ is the perpendicular distance from the edge. However, the calculations of the input impedance of a monopole on a square plate by Pozar and Newman [25] suggested that the surface patch dipoles adequately approximate this behavior a least-mean-square sense, and special edge modes with the required asymptotic behaviors do not significantly improve the final solution. On the contrary, Richmond [26] has added the edge modes (with proper behavior at the edge) to the other basis functions for strip grating and found that the convergence is improved. For simplicity, these special edge modes have been avoided, and satisfactory results (see Chapter Four) have been obtained. Criterion (c) ensures that the boundary condition is satisfied on the boundary of the plate.

Although criteria (d) and (e) are not necessary requirements, they are very important for the best computational efficiency. By keeping the sizes of the patches as close to the nominal value as possible, as stated in criterion (d), the total number of unknowns can be minimized. Rectangular modes are desirable by virtue of their rapid convergence rate and fast self and mutual impedance evaluation [21]. The expression for the mutual impedance between two closely spaced parallel current filaments is simpler to evaluate than that of the non-parallel case; thus, parallel filaments result in reduced overall computation time.

The corners (or nodes) and sides of the surface dipole modes form a grid or mesh which can be automatically generated. Okon and Harrington [27] listed several works done on automatic mesh generation and described the Gordon-Hall procedure, which is relatively easy to implement and satisfies several of the criteria listed previously.

B. Gordon-Hall (G-H) Procedure [23]

The G-H procedure forms a curvilinear coordinate system in an arbitrary region, R , by a one-to-one mapping ($\underline{U}: S \rightarrow R$) from a unit square $A'B'C'D'$ in the s - t plane (S domain) to the region bounded by $ABCD$ in the x - y plane (R domain) (see Figure 9). In the following discussion, R is a planar surface, but the method is applicable to an arbitrary curved surface embedded in three-dimensional space. The theory assumes the existence of a continuous vector-valued function \underline{F} which maps S onto R . However, in practice, the geometric description of R is given in terms of its boundary and \underline{F} becomes

$$\underline{F}(s,t) = \begin{bmatrix} x(s,t) \\ y(s,t) \end{bmatrix} \quad (22)$$

where $x(s,t)$ and $y(s,t)$ are parametric equations describing the boundary of R (∂R) in the x - y plane. A class of mapping or function

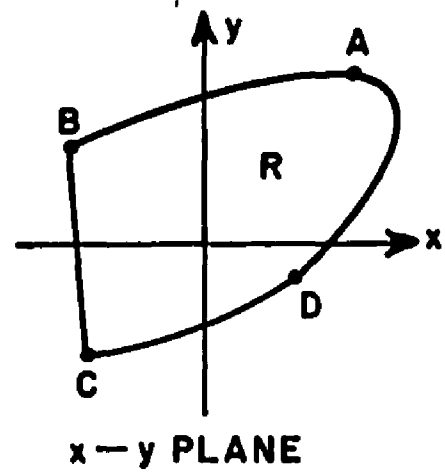
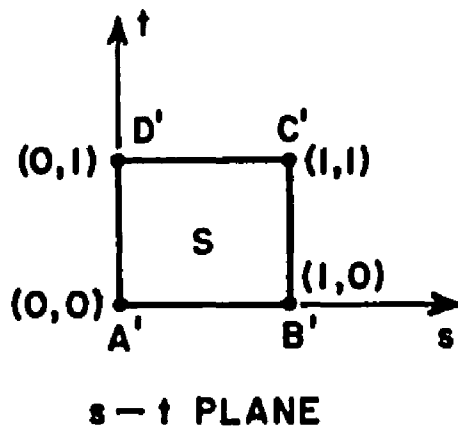


Figure 9. The Gordon-Hall domains.

\underline{U} which interpolate \underline{F} at a non-denumerable set of points (transfinite property) comprising the boundary of S is given by Gordon and Hall [23] as:

$$\begin{aligned} \underline{U}(s,t) = & (1-s)\underline{F}(0,t) + s\underline{F}(1,t) + (1-t)\underline{F}(s,0) + t\underline{F}(s,1) - \\ & (1-s)(1-t)\underline{F}(0,0) - (1-s)t\underline{F}(0,1) - s(1-t)\underline{F}(1,0) - \\ & st\underline{F}(1,1) \end{aligned} \quad (23)$$

\underline{U} can be described as a function which induces generalized coordinates s and t onto the region R . This can best be illustrated by examples given below.

1. The Quadrilateral [27]

The steps in forming a G-H mesh generator for a quadrilateral are (see Figure 10):

- a. Choose four points on ∂R which will separate the boundary of the quadrilateral into four segments. These segments should be approximately equal in order to have a uniformly spaced mesh. In this example, it is obvious that the four points are the corners of the quadrilateral.
- b. The four segments obtained above are to be the images of the four sides of the unit square S under the mapping F . That is, the segments are graphs of the four vector-valued functions: for $0 \leq s, t \leq 1$,

$$\underline{F}(s,0) = \begin{pmatrix} x_1 + s(x_2-x_1) \\ y_1 + s(y_2-y_1) \end{pmatrix} \quad (24)$$

$$\underline{F}(1,t) = \begin{pmatrix} x_2 + t(x_3-x_2) \\ y_2 + t(y_3-y_2) \end{pmatrix} \quad (25)$$

$$\underline{F}(s,1) = \begin{pmatrix} x_4 + s(x_3-x_4) \\ y_4 + s(y_3-y_4) \end{pmatrix} \quad (26)$$

$$\underline{F}(0,t) = \begin{pmatrix} x_1 + t(x_4-x_1) \\ y_1 + t(y_4-y_1) \end{pmatrix} \quad (27)$$

- c. The transfinite map \underline{U} (or the G-H mesh generator) is constructed by substituting Equations (24) through (27) into Equation (23), which results in:

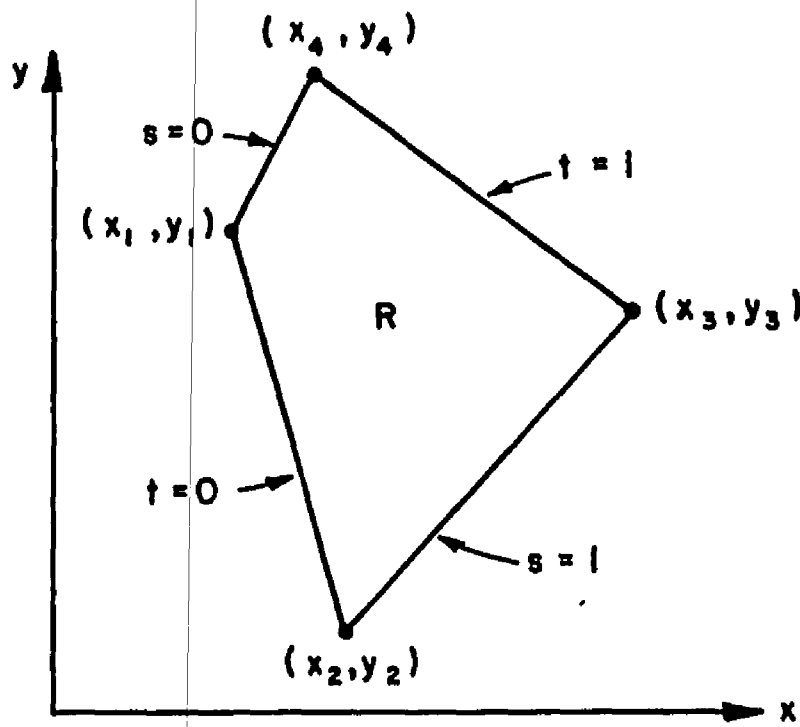


Figure 10. A quadrilateral region R in the x - y plane.

$$\underline{U}(s,t) = \begin{pmatrix} x(s,t) \\ y(s,t) \end{pmatrix} = s \begin{pmatrix} x_2 - x_1 \\ y_2 - y_1 \end{pmatrix} + st \begin{pmatrix} x_1 - x_2 + x_3 - x_4 \\ y_1 - y_2 + y_3 - y_4 \end{pmatrix} + t \begin{pmatrix} x_4 - x_1 \\ y_4 - y_1 \end{pmatrix} + \begin{pmatrix} x_1 \\ y_1 \end{pmatrix} \quad (28)$$

A grid formed by (28) is shown in Figure 11.

A special case of a quadrilateral is the triangle. The fourth corner is arbitrarily set at the midpoint of its longest side. The mesh formed by Equation (28) is shown in Figure 12.

2. The Ellipse [27]

This example differs from the previous one in two respects: first, it does not have a set of four well defined points for segmenting ∂R and, second, ∂R is a curved line instead of straight line segments (see Figure 13). However, the basic steps in finding \underline{U} are the same:

- a. The important consideration in choosing the four corner points is to choose them so that the resulting arc lengths are about the same. Thus, the four points $(a,0)$, $(0,b)$, $(-a,0)$, and $(0,-b)$ are chosen.
- b. The function \underline{F} is: for $0 \leq s, t \leq 1$,

$$F(s,0) = \begin{pmatrix} a \cos \frac{s\pi}{2} \\ b \sin \frac{s\pi}{2} \end{pmatrix} \quad (29)$$

$$F(1,t) = \begin{pmatrix} a \cos \frac{\pi}{2}(t+1) \\ b \sin \frac{\pi}{2}(t+1) \end{pmatrix} \quad (30)$$

$$F(s,1) = \begin{pmatrix} a \cos \frac{\pi}{2}(s+1) \\ -b \sin \frac{\pi}{2}(s+1) \end{pmatrix} \quad (31)$$

$$F(0,t) = \begin{pmatrix} a \cos \frac{\pi t}{2} \\ -b \sin \frac{\pi t}{2} \end{pmatrix} \quad (32)$$

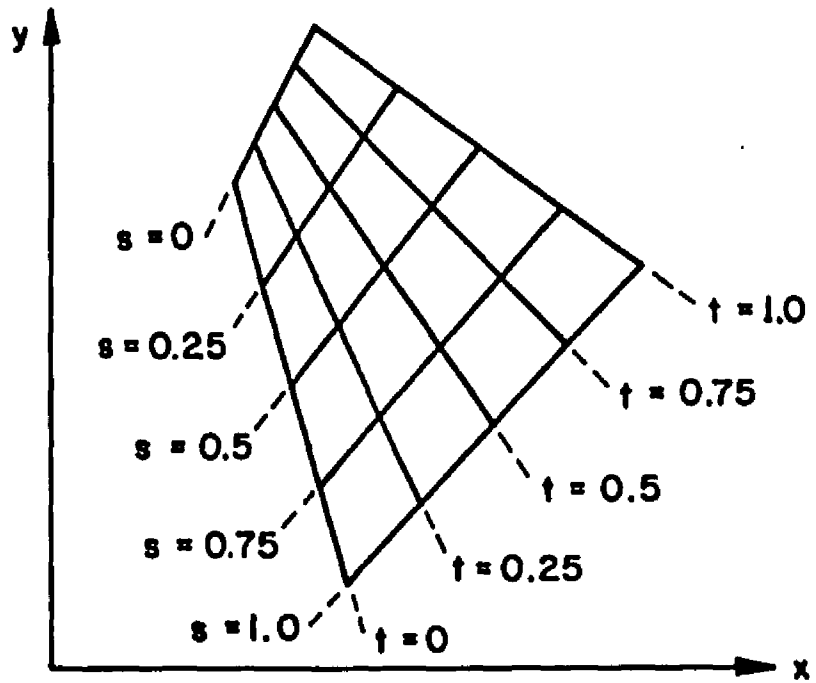


Figure 11. The curvilinear coordinates formed by the G-H Procedure for the quadrilateral in Figure 10.

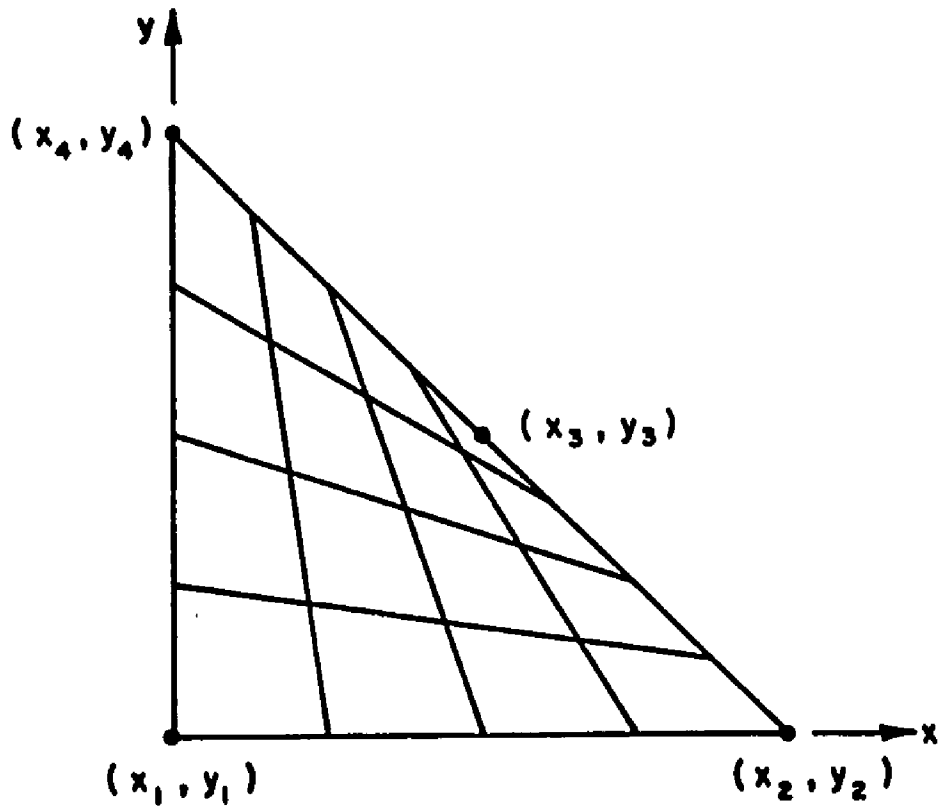


Figure 12. The curvilinear coordinates formed inside a triangular region by the G-H Procedure.

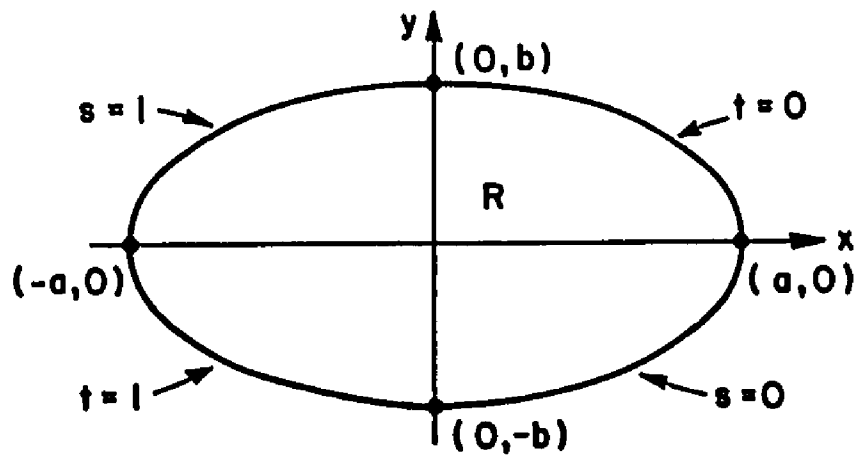


Figure 13. An elliptical region R in the x-y plane.

c. Substituting Equations (29) through (32) into (23) yields:

$$\underline{U}(s,t) = \begin{pmatrix} x(s,t) \\ y(s,t) \end{pmatrix} = \begin{pmatrix} a \left[(1-s) \cos \frac{\pi t}{2} - s \sin \frac{\pi t}{2} + (1-t) \cos \frac{\pi s}{2} - t \sin \frac{\pi s}{2} + s+t-1 \right] \\ b \left[s \cos \frac{\pi t}{2} - (1-s) \sin \frac{\pi t}{2} + (1-t) \sin \frac{\pi s}{2} - t \cos \frac{\pi s}{2} + t-s \right] \end{pmatrix} \quad (33)$$

Note that, in this case, \underline{U} maps the straight lines in the s - t plane into curved lines in the x - y plane, as shown in Figure 14. Since only straight line segments are allowed for the surface patch mode, the mesh is formed by connecting the intersection points by straight line segments as shown in Figure 15.

G-H procedure is an automatic mesh generator which satisfies criteria (a) through (c) in section A of this chapter. However, criteria (d) and (e) are usually not met for an arbitrary boundary. In order to have criterion (d) satisfied, the four arcs describing the ∂R must be carefully chosen such that they are approximately of equal length. Note that each arc can be a straight line, curved lines, or two or more straight line segments [23]. However, a bad choice of the arc sections may result in a mapping \underline{U} which does not map S onto the correct planar surface of R [23]. To alleviate this problem, a region R with complex boundary may be subdivided into subregions and each region is mapped independently. This will require the user to parameterize the boundaries of several subregions, and these subregions must be joined electrically by overlapping surface-patch dipole modes. Since criterion (e) is seldom met in an arbitrary region R , this results in inefficient evaluation of the impedance which translates into a large amount of computation time. Alternative subdivision schemes are proposed to find a more desirable mesh for regions R which are polygons.

C. Subdivision Method 1

The objective of this section and the next is to present algorithms such that, when implemented in the form of a computer code, can provide the coordinates for a set of surface dipole modes which satisfies all the criteria given in Section A. It is assumed that an arbitrarily shaped plate can be adequately described as a polygon. Thus, the plate can be described by a set of points, ordered in either clockwise or counter-clockwise direction, and the straight lines joining these points form the boundary of the plate. The basic approaches used in these two subdivision schemes are discussed in Appendix C.

The general approach of this scheme is to choose a side and divide the plate into strips which are parallel to this side. The width of the strips is to be about the same or less than a specified maximum size, W . Each end side of the strips should be a straight line segment

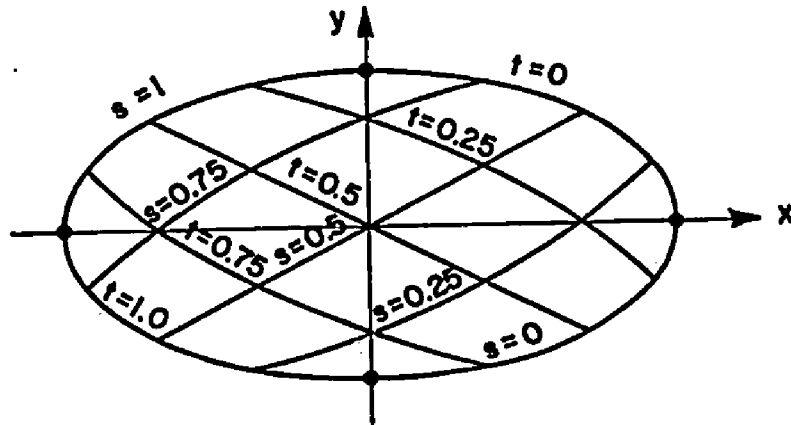


Figure 14. The curvilinear coordinate system induced by the transfinite mapping \underline{U} .

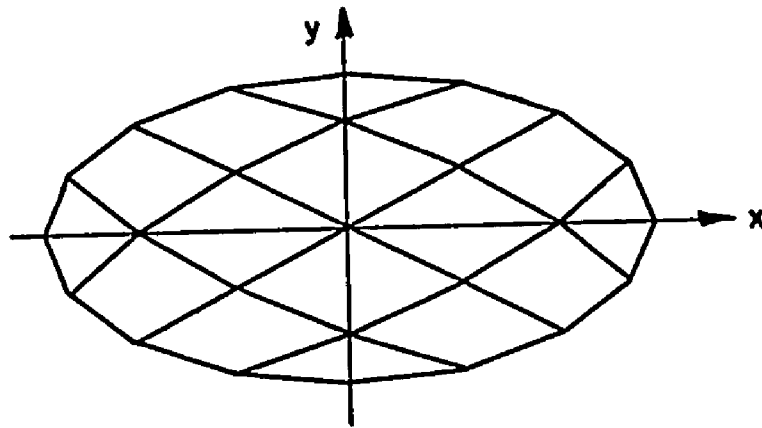


Figure 15. A mesh for the overlapping surface-patch dipole modes.

which is a part of the plate boundary. A grid can be formed by segmenting the strips into an equal number of blocks and the maximum length for the blocks should be less than or equal to the maximum width, W . The details of the algorithm is given below (see Figures 16 and 18 - note that the arrows indicate the direction of the overlapping surface patch dipole modes):

- a. Choose a side such that strips parallel to this side (reference side) can be formed throughout the plate. Usually the longest side is chosen. As shown in Figure 16, either sides AB, DE, or AE can be chosen, but choosing other sides will not allow the plate to be divided into parallel strips. That is, the reference side must be chosen such that the perpendicular vectors from the reference side to all other corners of the plate must all point in the same direction. Also, three consecutive vectors should have the property that the length of the middle vector is not the shortest among the three vectors. That is the situation as shown in Figure 17, where AE chosen as the reference side is not permissible. If AB is not parallel to DE, then the strip with a side coinciding to DE will not be trapezoidal. The strip width is found by dividing the perpendicular distance from the reference line (AB in this example) to the nearest corner by the smallest integer N_s that will make the result less than or equal to W . Note that strip widths can vary depending on the distance from the reference side to the corners. If the length DE is zero, then the strip with side DE will have very short and zero length current elements. This is avoided by reducing the width of this particular strip so that there will be no side with zero length. Since there will be current filaments along the end sides of each strip (see Figures 16 and 18), each strip must have no end sides whose lengths exceed 0.25λ . If this is not satisfied, the strip must be further divided into smaller strips.
- b. Find the minimum integer, N_t , which the longest strip can be segmented such that the length of each section along this strip does not exceed W . Each strip is then divided into N_t sections, resulting in a mesh as shown in Figures 16 and 18. Note that, if the two end sides of a strip are not parallel, only trapezoidal blocks can be formed.

The mesh formed by this scheme will have about half of the surface dipoles with current filaments that are parallel to each other (see Figures 16 and 18). This is due to the fact that usually only trapezoidal blocks can be formed. However, the more disturbing feature of this scheme is that, if there are strips whose lengths are much shorter than others, there will be a relatively large number of very small (or short) surface dipoles in the shorter strips. In spite of these shortcomings, this scheme is still attractive as a plate can be divided into strips whose lengths do not vary significantly.

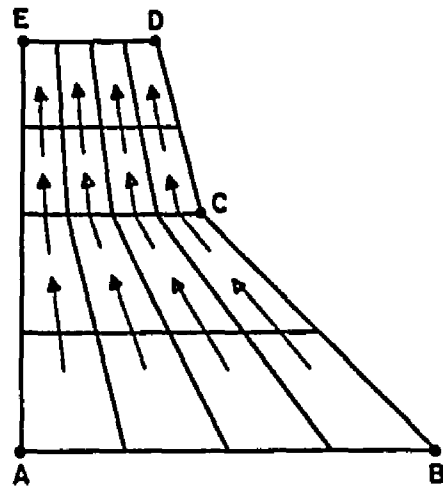
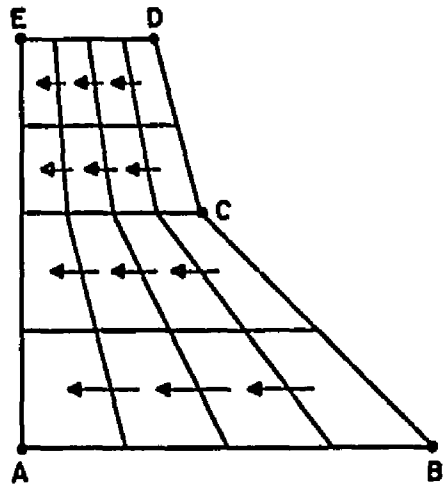


Figure 16. A set of overlapping surface-patch dipole modes formed inside a fin-shaped polygon by using subdivision method 1. The arrows indicate the direction of the currents.

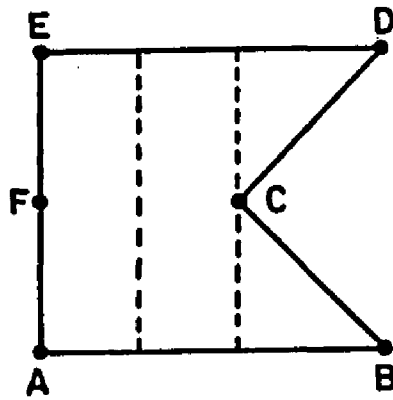


Figure 17. A situation in which the side AE cannot be the reference side.

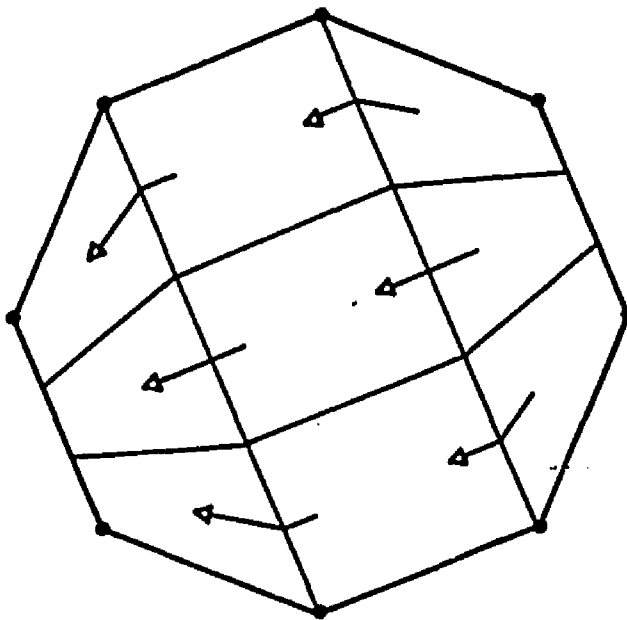
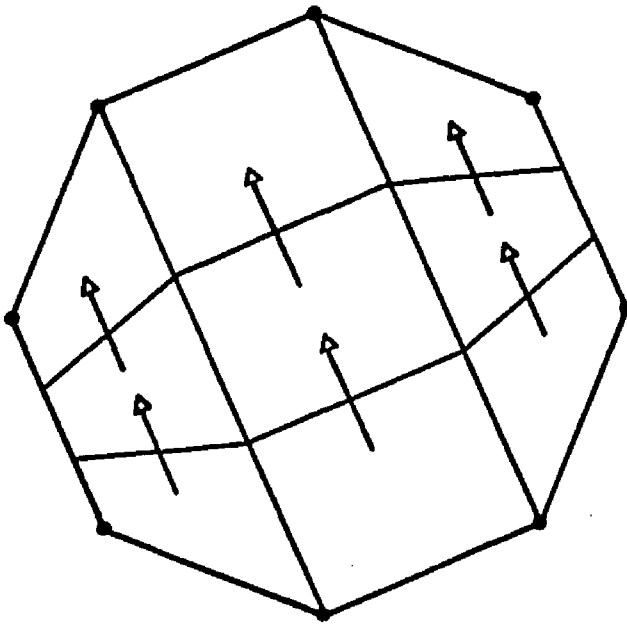


Figure 18. A set of overlapping surface-patch dipole modes formed inside a regular octagon by using subdivision method 1. The area inside the polygon is equal to that of a circle with a 0.3λ radius.

A modification of this algorithm results in the next scheme where two meshes are formed for the two current polarizations.

D. Subdivision Method 2

This subdivision scheme is similar to the previous one in that strips are formed from one side of the plate. However, the strips are not segmented by the same number of sections N_t ; instead, each strip is segmented into a minimum number of sections. This allows the sizes of the surface monopoles to be more uniform. The interior sides are adjusted such that most of the segments in a strip will be rectangular (see Figures 21 and 22). This choice of segmentation will allow only one set of surface dipole currents in the direction along the length of the parallel strips. The other set of dipole modes are formed by dividing the plate into strips again, but this time the strips are perpendicular to the previous set of strips (see Figure 23). The details of this subdivision scheme are:

- a. This step is similar to step (a) in subdivision method 1. However, relatively short strips are allowed. It is possible that a plate geometry (such as that shown in Figure 17) will not allow only one strip with the ends being the perimeter of the plate to be formed. To get around this problem, another side may be chosen for the reference side. Alternatively, the plate can be divided into two plates and surface-patch dipoles set up for each plate. These two plates are then joined by the plate overlap modes.
- b. Each strip is segmented into the minimal number of sections such that the length of each section should not exceed the specified nominal value, W . If the two end sides are parallel, i.e. $AD \parallel BC$ in Figure 19, the sections will be rectangular. If AD is not parallel to BC and the length of the longest side of the strip is less than three times the maximum width, W , the strip is divided as shown in Figure 20.

In the case where AD is not parallel to BC and the length of the longest side is greater than three times the nominal length, an attempt is made to segment the strip such that the segments in the middle of the strips are rectangular. As shown in Figure 21, if $|AD| \leq W\sqrt{2}$, then the strip can first be segmented by the line $A'D'$. The line $A'D'$ is placed such that the length of AA' is the maximum width, W . If the length of DD' is less than $0.2W$, the point E' , which is the midpoint of segment DE , is used to segment the strip. This will allow the quadrilateral $AA'E'D$ to have a more uniform side length. The same is done for the other end and the segmentation of the rectangle $E'FB'C'$ will result in rectangular sections, as shown in Figure 21. If $|AD| > W\sqrt{2}$ (see Figure 22), then the strip can first be segmented

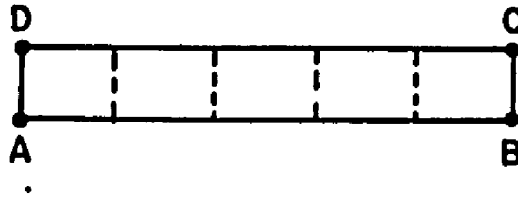


Figure 19. Subdivision of a rectangular strip.

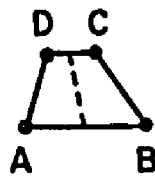


Figure 20. Subdivision of a trapezoidal strip.

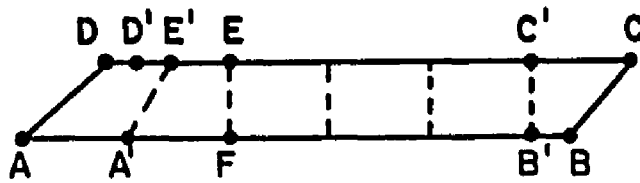


Figure 21. Subdivision of a trapezoidal strip with rectangular sections in the middle part of the strip.

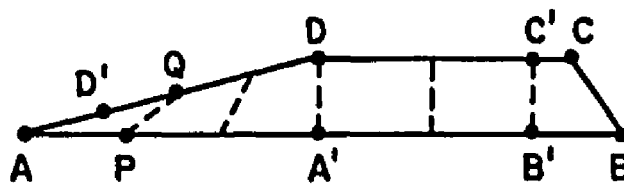


Figure 22. Subdivision of a trapezoidal strip with very long end sections (AD and AD').

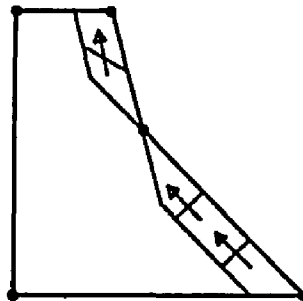
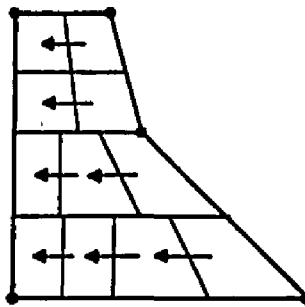
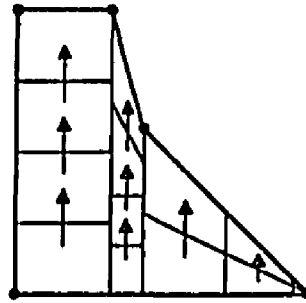


Figure 23. A set of overlapping surface-patch dipole modes formed inside a fin-shaped polygon by using subdivision method 2.

by the line A'D. The line A'D is the perpendicular line from point D to the line segment AB. The line AD is segmented into N segments such that no section is greater than W. Note that line AA' is segmented one segment less than the line AD. This allows the quadrilateral APQD' to be formed at the end of the strip. The line segment B'C' is found like the above and the rectangle A'B'C'D is segmented into rectangular segments.

- c. To form the other set of currents orthogonal to the first set, a line is drawn from the furthest corner and perpendicular to the reference side. Strips are then formed parallel to this line and the division is the same as that of steps (a) and (b).
- d. As shown in Figure 23, there may be some sides of an arbitrarily shaped plate which do not have non-zero currents parallel to the edges. Extra strips are formed parallel to these edges. The widths of these strips are the average width of the previously formed strips or smaller.

The three subdivision schemes discussed in this chapter are just a few of the possible mode layouts. Experience has shown that subdivision methods 1 and 2 are applicable to a wide range of plate shapes. A computer subroutine has been written which implements method 1 and method 2. The subroutine chooses method 1 if the difference of the longest and shortest strip formed is less than $4W$, and chooses method 2 otherwise. Also, if the length of the shortest strip is less than $0.1 W$, then method 2 will be chosen. The user specifies the corners of the polygon and the maximum segment size, W . The subroutine generates the coordinates of the surface-patch dipole modes on the polygon plate. The accuracy and efficiency of these mode set-ups in the moment method is discussed in the next chapter on numerical results.

CHAPTER IV

NUMERICAL RESULTS

In this chapter, data for the input impedance of a monopole antenna centered on a disk and scattering data from different polygonal plates are presented. The surface-patch modes are formed automatically by the subdivision algorithms given in the preceding chapter. A maximum segment size $W=0.25\lambda$ is used for all plate subdivisions. The results are compared with measurements and independent calculations. All the computations were done on the Digital Equipment Corporation VAX 11/780, which is three to four times slower than the IBM-370/168.

A. Monopole Antenna on a Disk

The study of the monopole antenna on a circular disk is of interest since it leads to the understanding of the effect of the finite ground plane on antenna input impedance and radiation pattern. Richmond [28] listed the work on this subject and presented a moment method solution. PWS current forms were used for the wire and the disk dipole mode consisted of two concentric annular zones with radially directed currents across the two zones.

In order to use the techniques developed in this work, the circular disk is first approximated by a polygon. Thin-wire, attachment, and surface-patch modes are used to represent the surface currents. The surface-patch modes are formed by using subdivision method 1. The surface dipole modes for an octagonal disk with a radius of 0.3λ are shown in Figure 18. The input resistance and reactance of a $\lambda/4$ monopole versus disk radius are shown in Figures 24 and 25, respectively. Data are shown for square and octagonal disks. In both cases, the areas are kept constant and equal to that of a circular disk with radius, A . A disk monopole radius of 0.2λ is used for the attachment mode. The most dominant modes in this problem are the wire and attachment modes. This is especially true for small disk radius. As the disk radius becomes larger, the surface-patch modes become more influential to the final result. The computed results are compared with the data obtained from the formulation by Richmond [28]. The result from the square disk approximation agrees with Richmond's result up to about $A = 0.4\lambda$, while that of the octagonal disk approximation is in good agreement up to $A = 1.0\lambda$. The formulation used in this work can solve the problem of the off-centered monopole, which was not treated in any previous work.

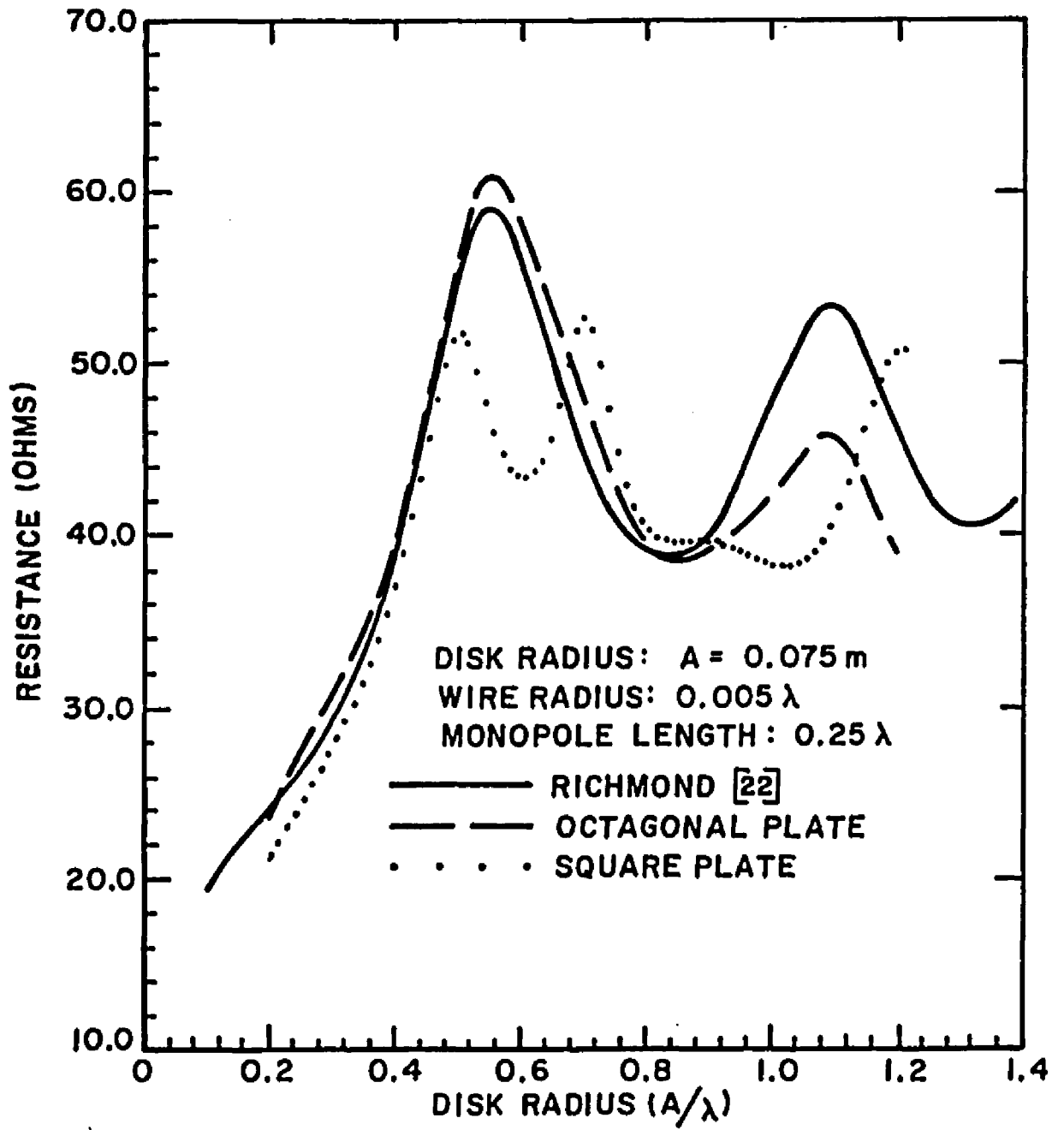


Figure 24. Resistance of a monopole antenna at the center of a disk in free space.

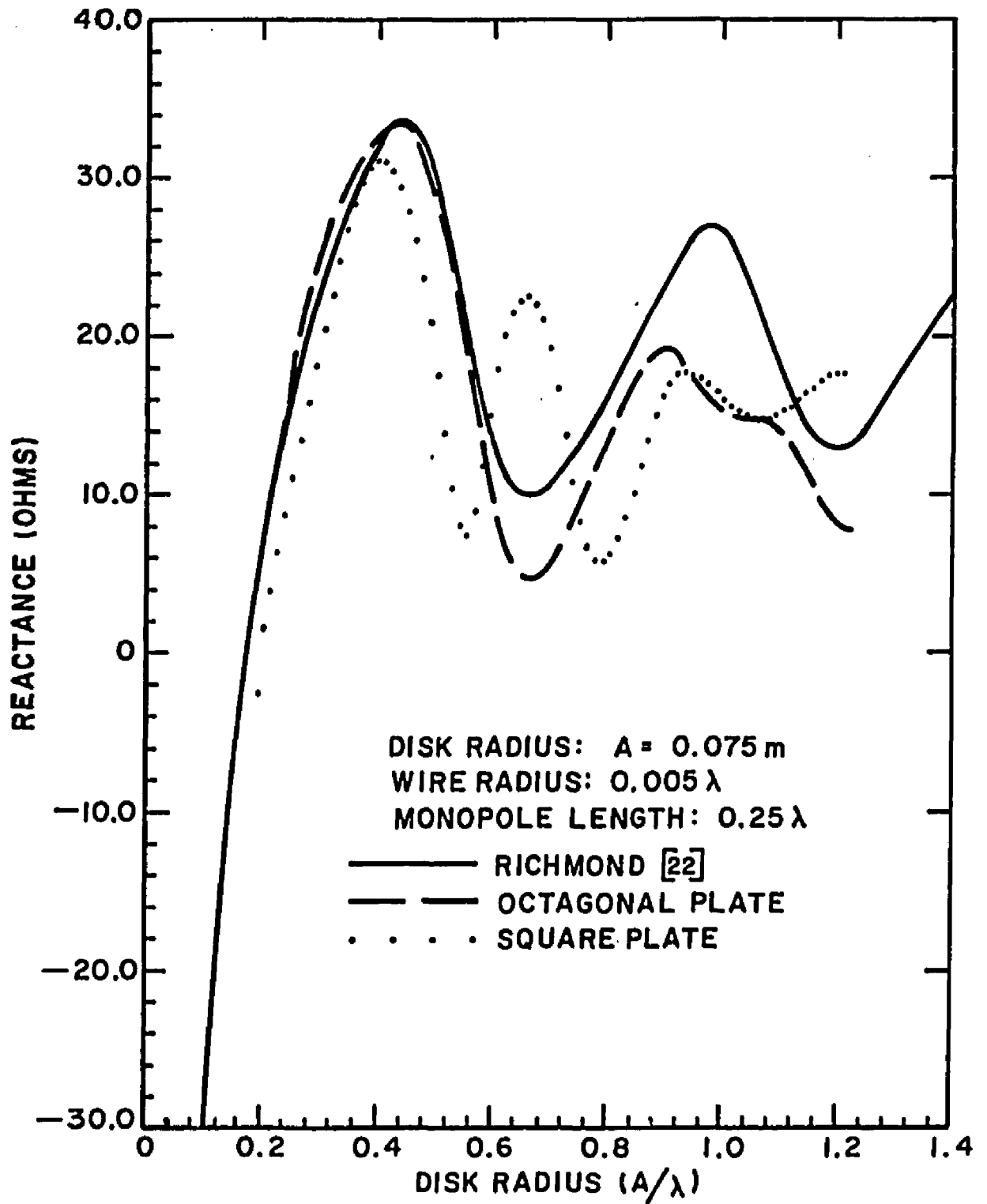


Figure 25. Reactance of a monopole antenna at the center of a disk in free space.

B. Scattering from Polygonal Plates

In this section, the scattering data from plates with different sizes and shapes are compared with independent calculations and measurements. The bistatic and backscatter data are plotted in terms of the radar cross-section (or echo area) defined as

$$\sigma = \lim_{r \rightarrow \infty} \left[4 \pi r^2 S_s / S_i \right] \quad (34)$$

where r is the radial distance from the plate to the observer and S_s and S_i denote the time average power densities in the scattered and incident fields, respectively.

The backscatter measurements were made at 9.067 GHz. The plates were cut from 0.032-inch thick aluminum sheet stocks. A transit was used to align the suspended plate with the polarization axis of a horn antenna. All these measurements were done at The Ohio State University ElectroScience Laboratory by T. Chu.

1. Circular Disks

Figure 26 shows the broadside radar cross-section of an octagonal plate at different disk radii. Also shown are the data obtained from the eigenfunction solution of a circular disk by Hodge [29]. Subdivision method 1 is used to set up the surface-patch modes except at the frequency where the disk radius is 1.7λ . Here subdivision 2 is used to reduce the number of unknowns and computation time.

Backscatter data from an octagonal plate with a radius of 1.2λ are shown in Figures 27 and 28 for the θ and ϕ polarization, respectively. Bistatic data for the same plate are shown in Figures 29 and 30 for the θ and ϕ polarization, respectively. Comparisons of the scattering results from the octagonal plate with the eigenfunction solution by Hodge [29] show disagreements between the present calculations and Hodge's data at angles close to and at grazing incidence. This is due to the fact that an octagon only approximates a circle. The elevation plane pattern for a circular disk should be independent of ϕ . However, the pattern made at $\phi = 0^\circ$ and $\phi = 22.5^\circ$ for the octagonal plate are not identical. Note that the solution for the circular disk falls between these two curves. This seems to indicate the effect of the octagonal approximation to a circular disk.

2. Triangles

The backscatter data from a right angle triangle with the side lengths of 3λ are shown in Figures 31 through 33. The surface-patch mode setup using subdivision method 2 and the Gordon-Hall procedure are

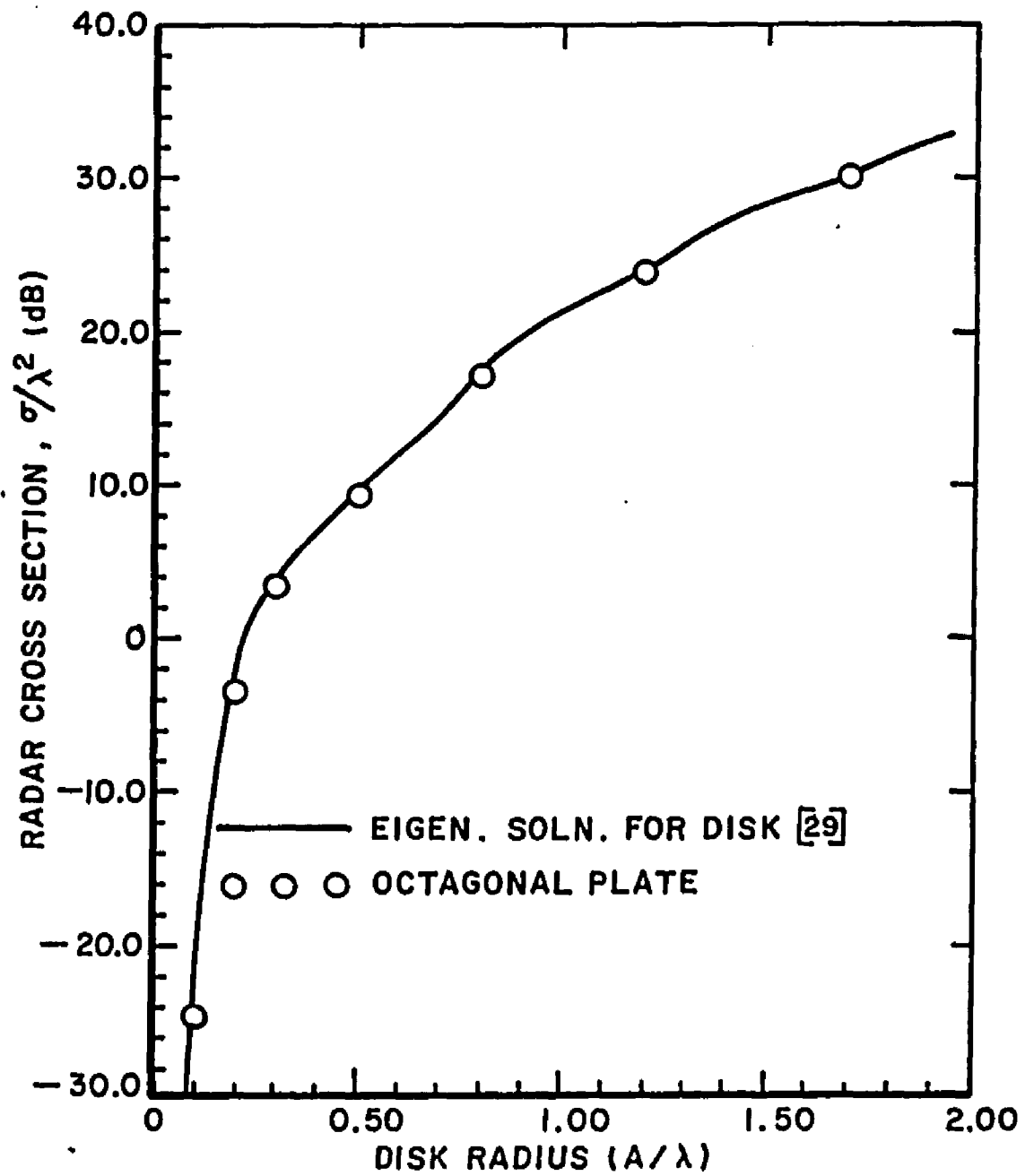


Figure 26. Normal incidence, backscatter from disk.

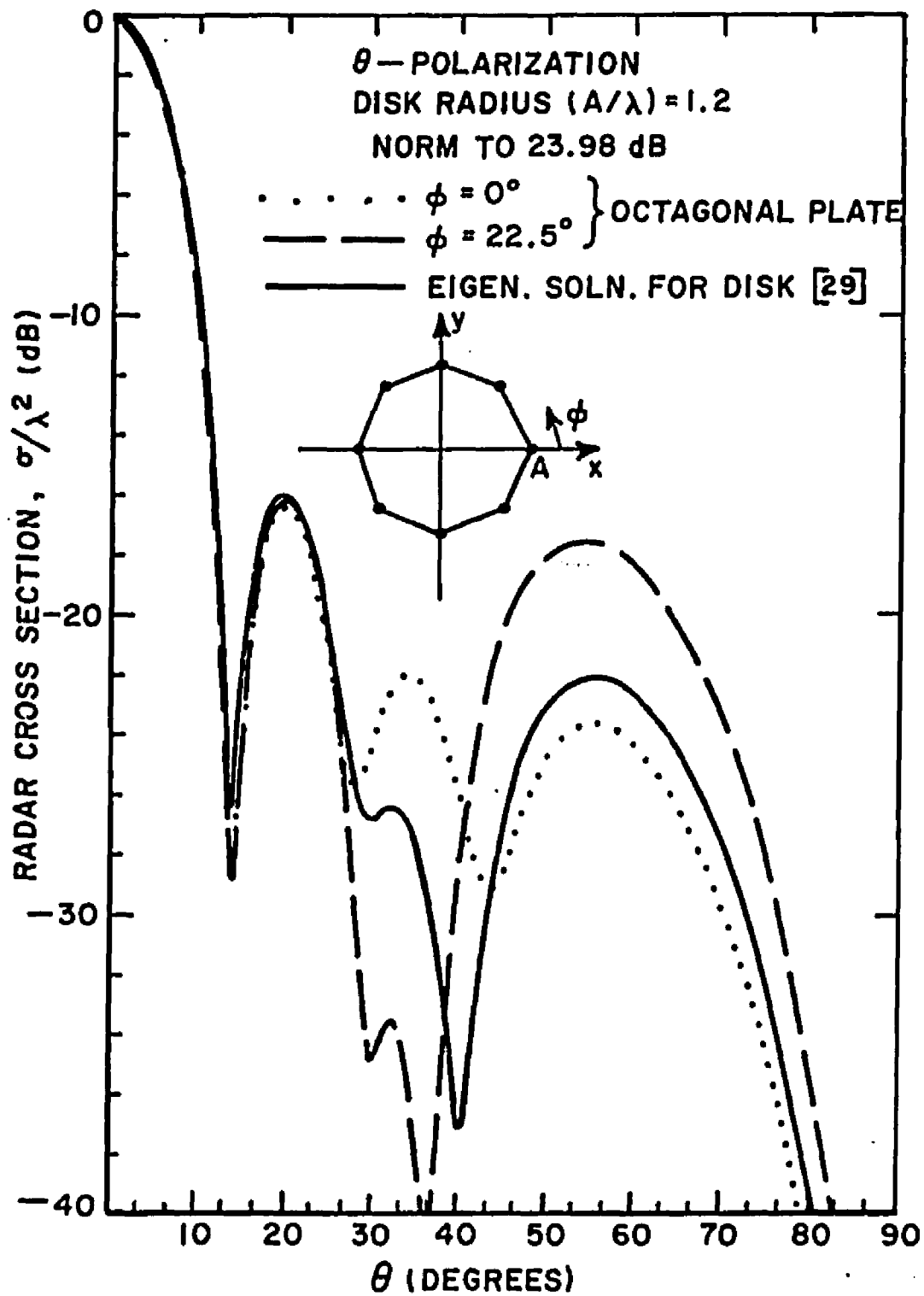


Figure 27. Backscatter from disk with $A/\lambda = 1.2$.

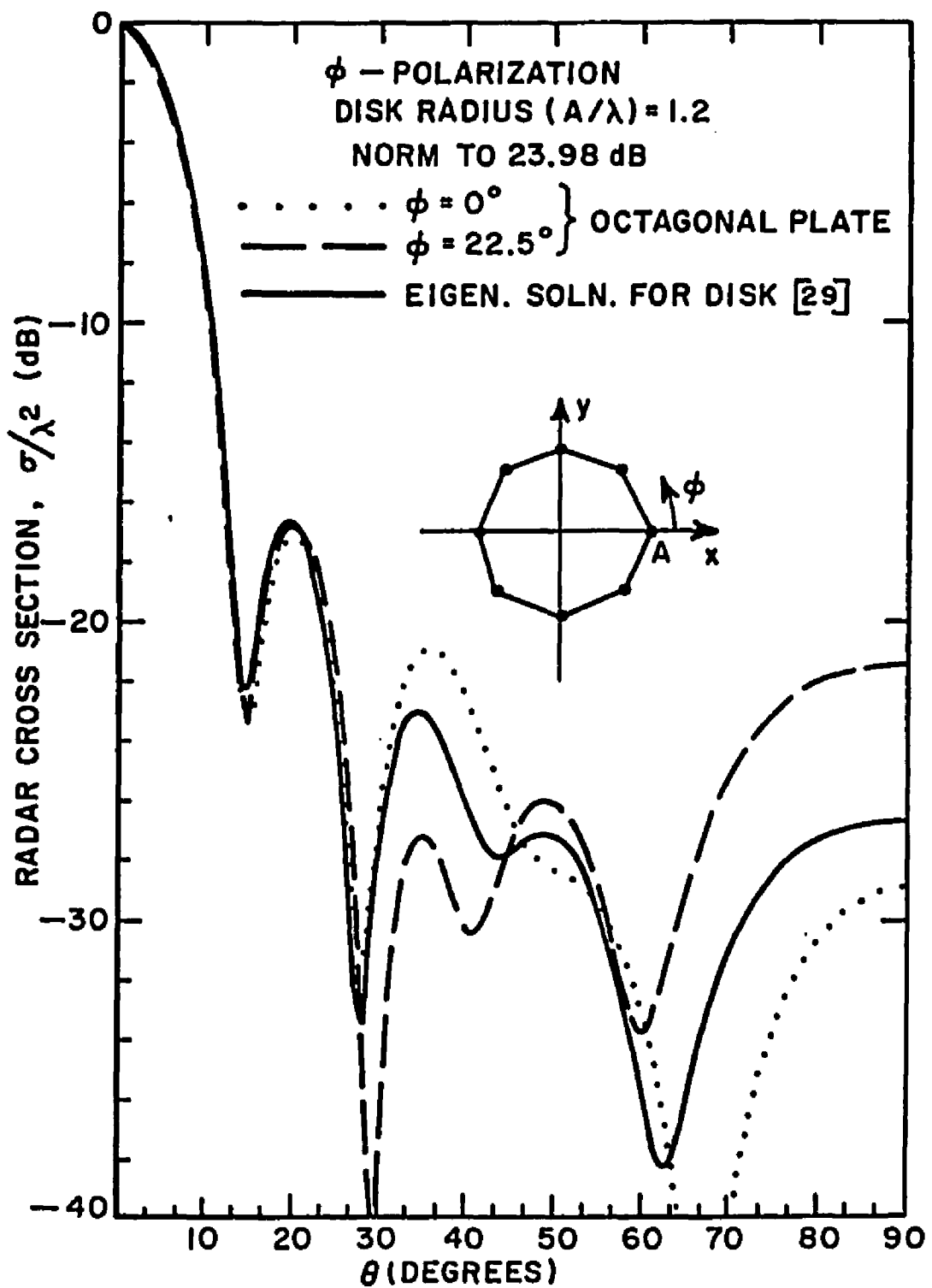


Figure 28. Backscatter from disk with $A/\lambda = 1.2$.

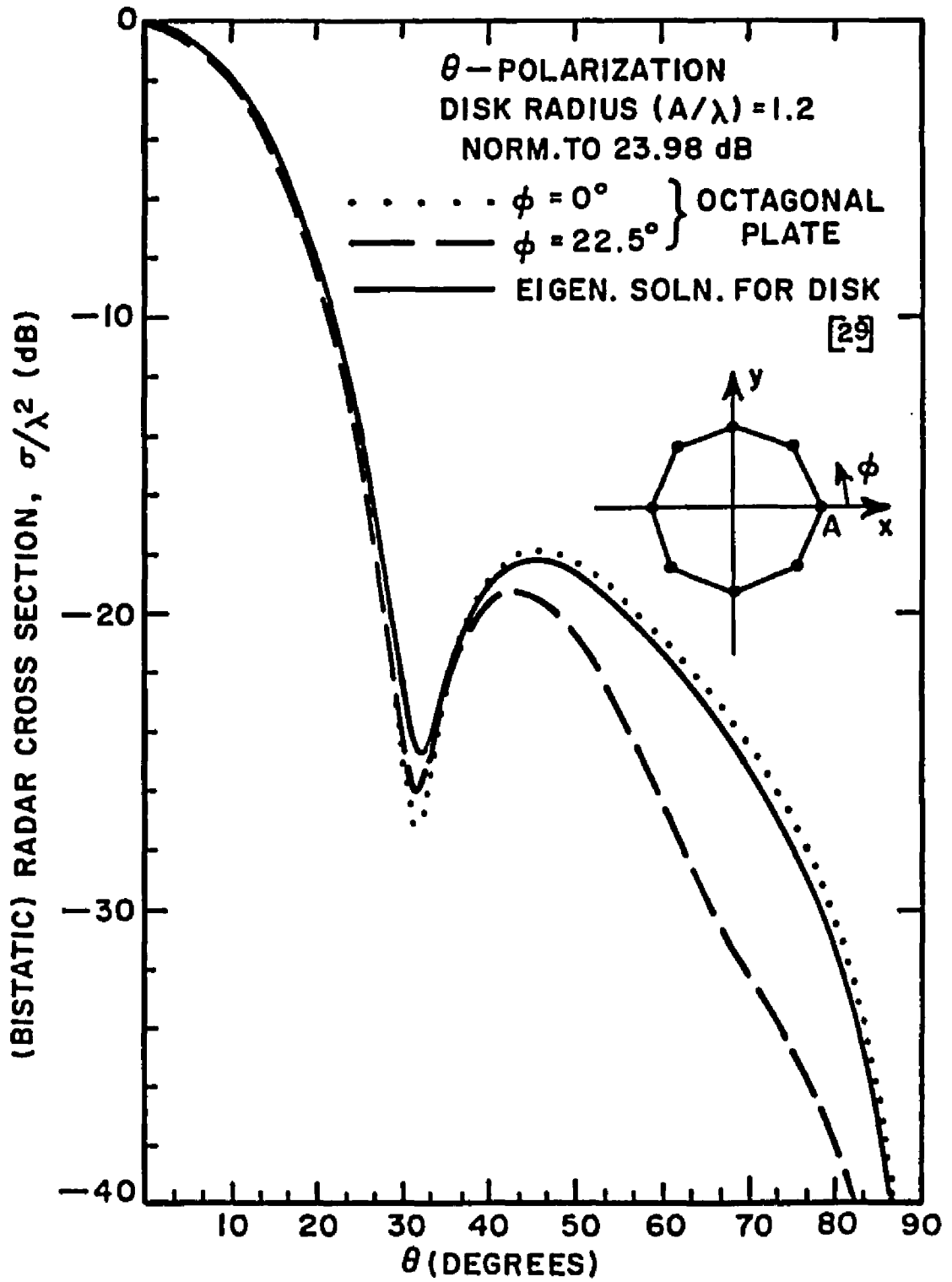


Figure 29. Normal incidence, bistatic scatter from disk with $A/\lambda = 1.2$

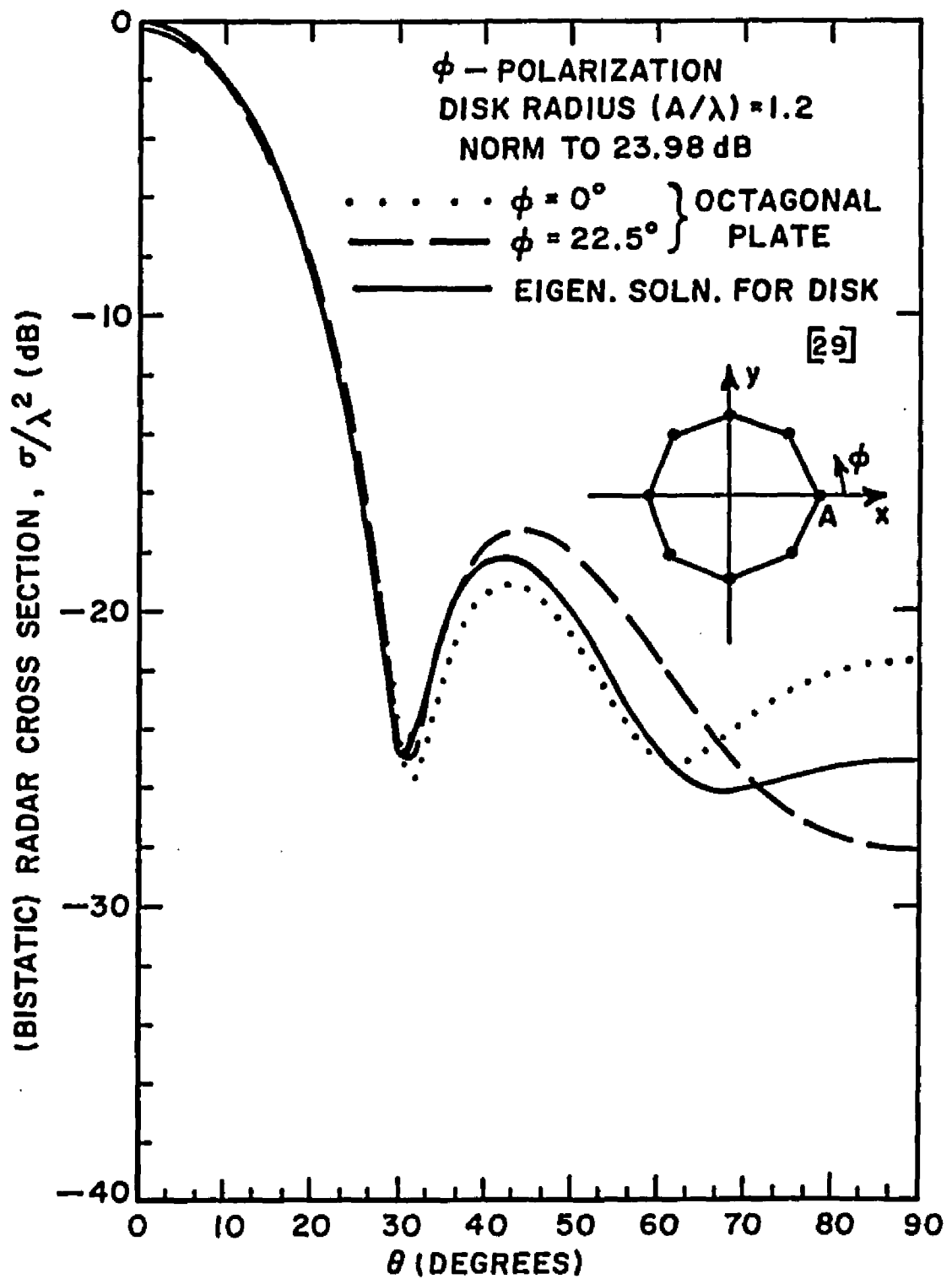


Figure 30. Normal incidence, bistatic scatter from disk with $A/\lambda = 1.2$.

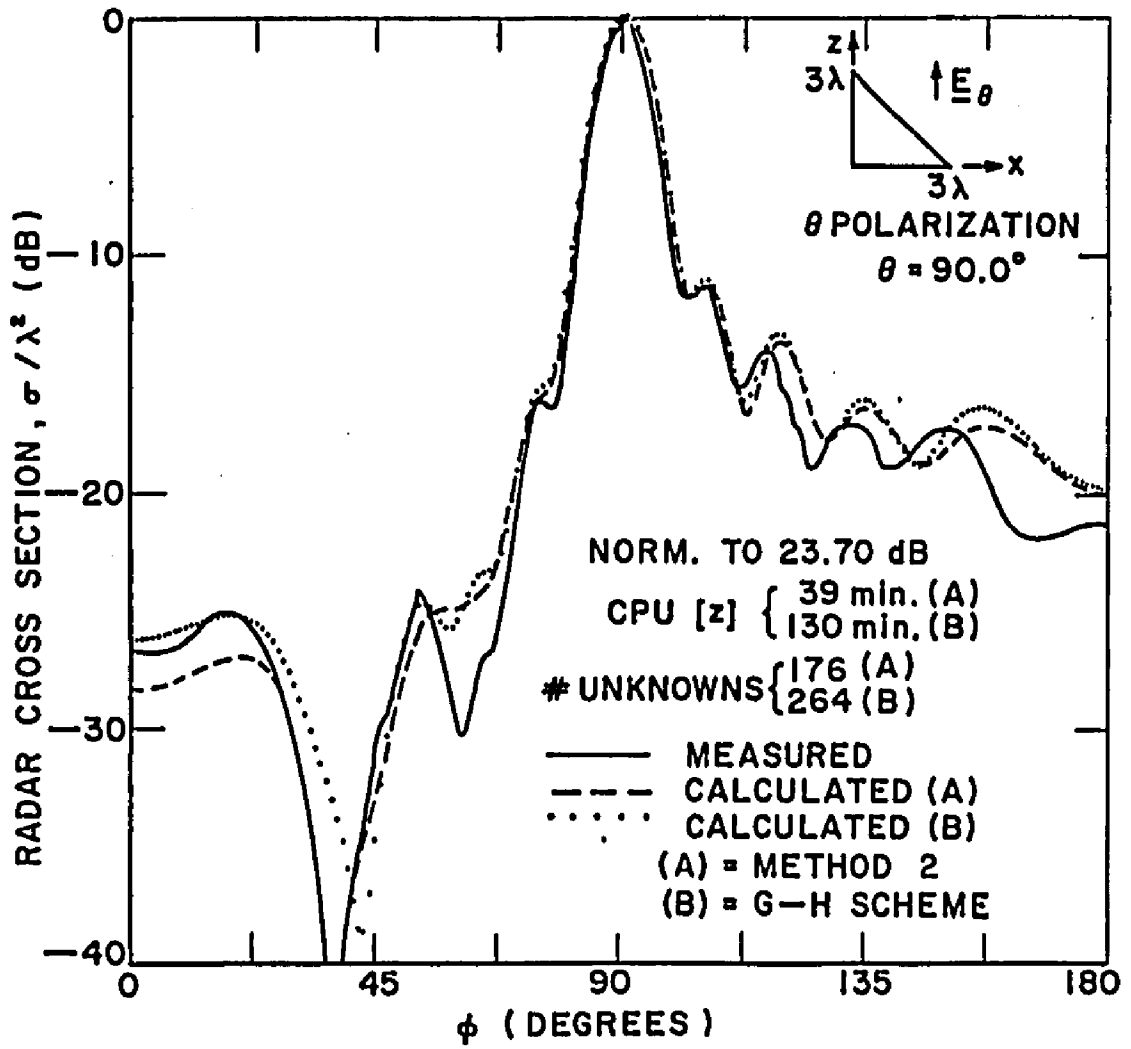


Figure 31. Backscatter from a 3λ right angle triangle (θ -polarization).

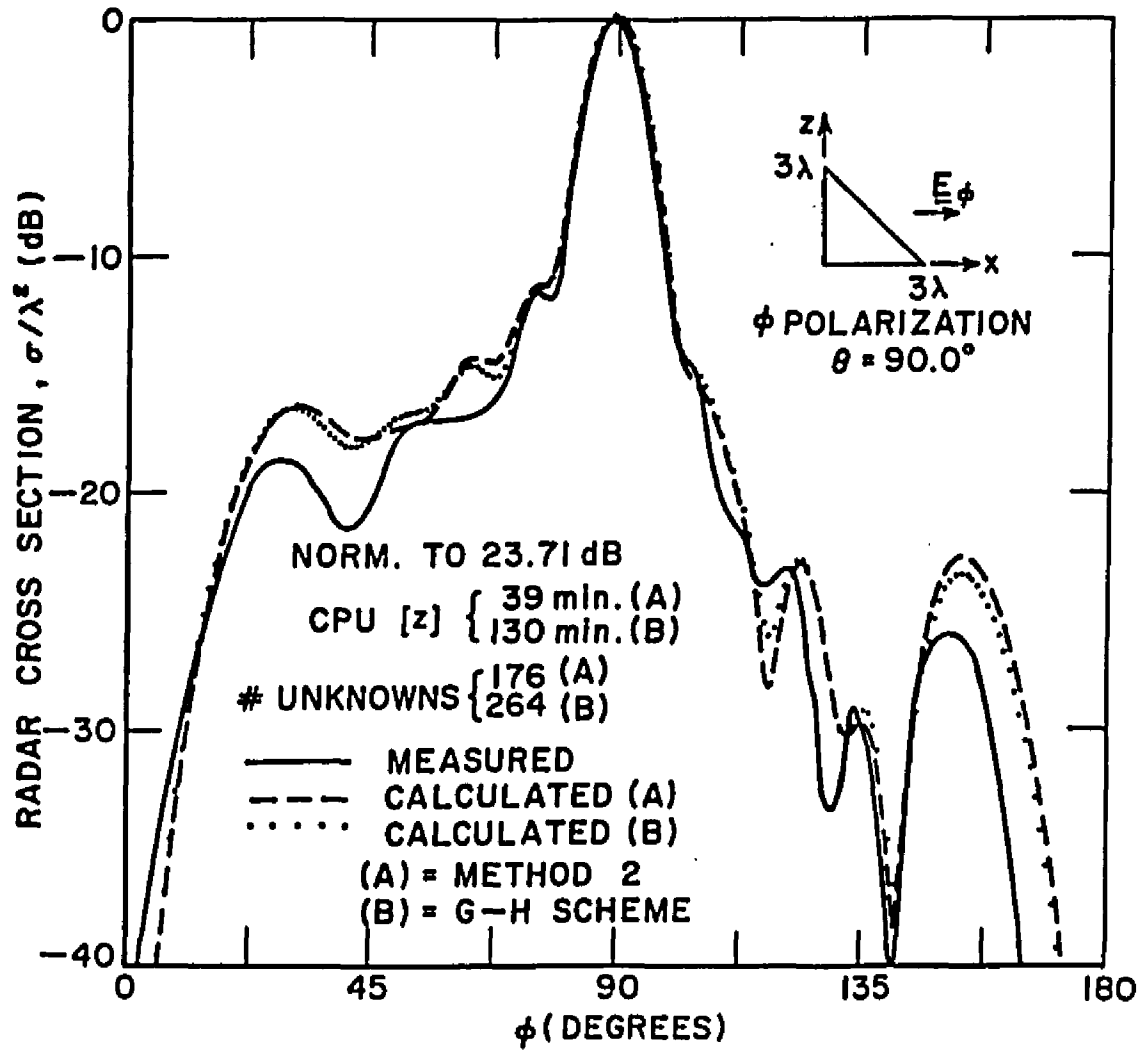


Figure 32. Backscatter from a $3\text{-}\lambda$ right angle triangle (ϕ -polarization).

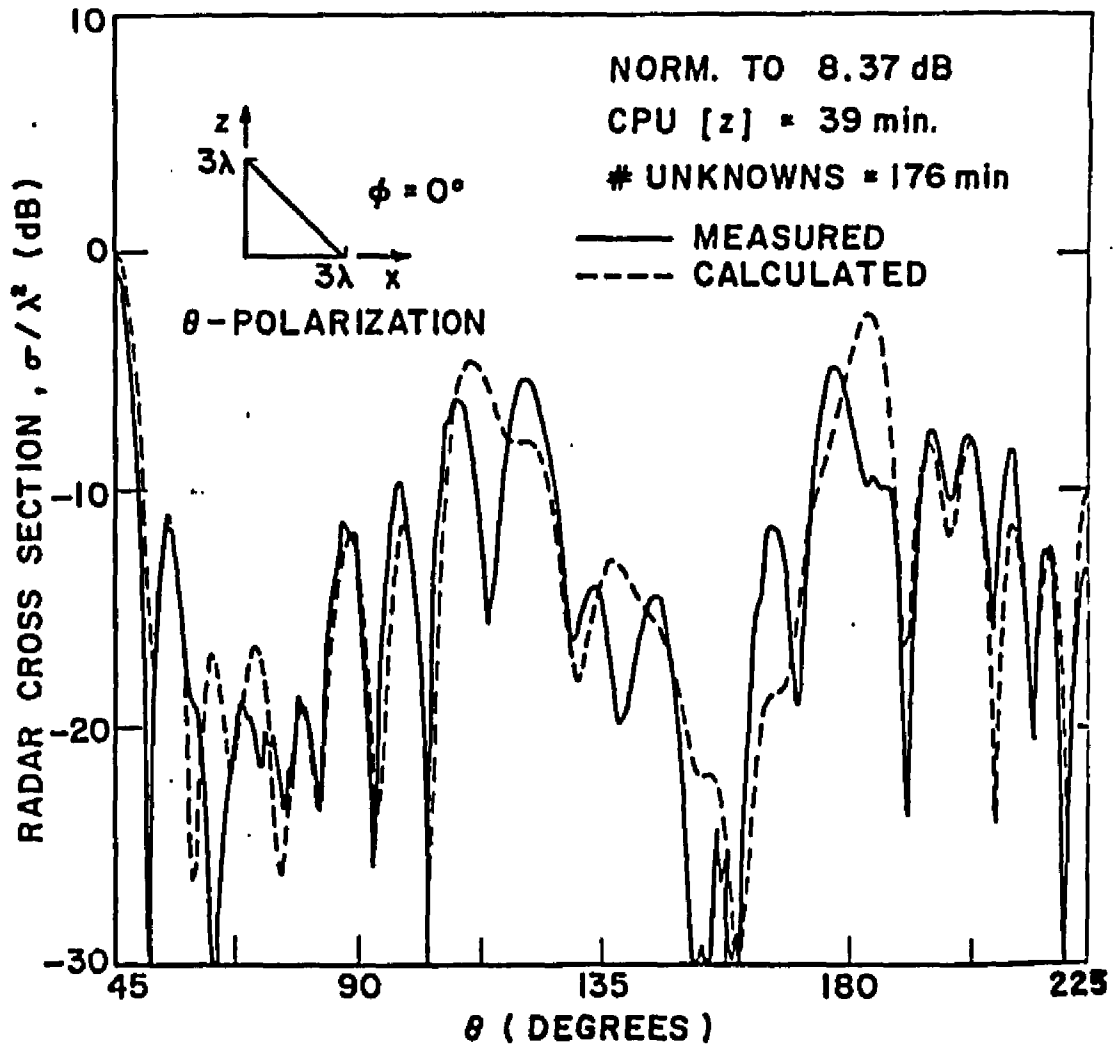


Figure 33. Backscatter from a 3λ right angle triangle (θ -polarization) in the elevation plane.

shown in Figures 34 and 35, respectively. Note that the Gordon-Hall procedure set up 264 surface dipole modes, while subdivision method 2 set up only 176 modes. The backscatter data obtained by using the two-mode layouts and measurements are shown for the azimuth plane with θ - and ϕ -polarization and the θ -polarization for the elevation plane in Figures 31, 32, and 33, respectively. Although the result from the Gordon-Hall mode layout is not shown in Figure 33, it agrees well with the two curves shown.

The backscatter for an isosceles triangle in the azimuth plane for θ - and ϕ -polarization are shown in Figures 36 and 37, respectively. The surface-patch mode layout, using subdivision method 2 as shown in Figure 38, illustrates how the quadrilateral surface-patch modes are adequate for modelling the surface currents on a plate with a very acute angle. The acute angle is 30° and the perpendicular height of the triangle is 3.25λ . No measurement was done for the ϕ -polarization (see Figure 37), but the result shown can be assumed to be accurate.

3. Fin-shaped Plate

A fin-shaped plate along with the surface-patch mode layout is shown in Figure 39. This plate geometry again illustrates that subdivision method 2 does set up modes with relatively uniform sizes. Figures 40 and 41 show the calculations and measurements of the backscatter in the azimuth plane for the θ - and ϕ -polarization, respectively. In the ϕ -polarization (Figure 41), a curve obtained by using the Geometric Theory of Diffraction (GTD) is shown. This GTD formulation, which incorporated equivalent edge diffracted currents [30], is currently being developed at The Ohio State University ElectroScience Laboratory [31].

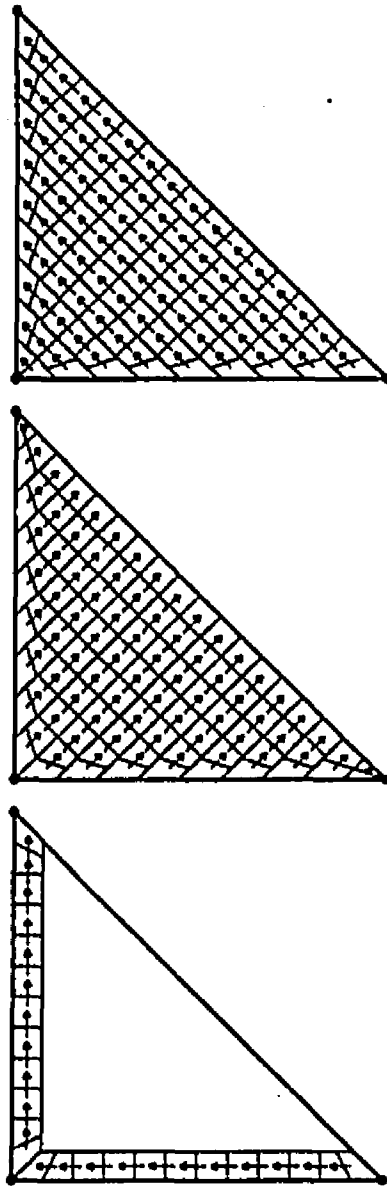


Figure 34. A set of overlapping surface-patch modes formed in a $3-\lambda$ right angle triangle by using subdivision method 2. This set of modes is used to generate the backscatter data in Figures 31 through 33.

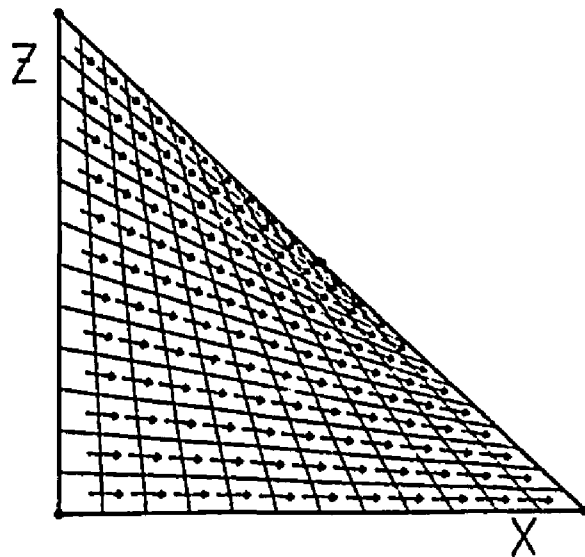
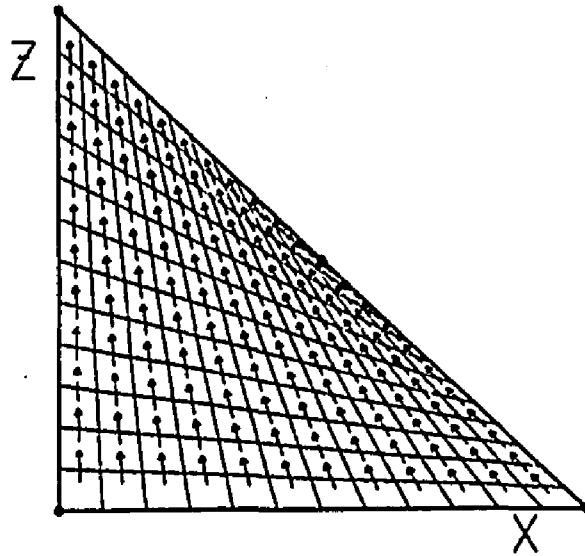


Figure 35. A set of overlapping surface-patch modes formed in a $3\text{-}\lambda$ right angle triangle by using the Gordon-Hall procedure. This set of modes is used to generate the backscatter data in Figures 31 and 32.

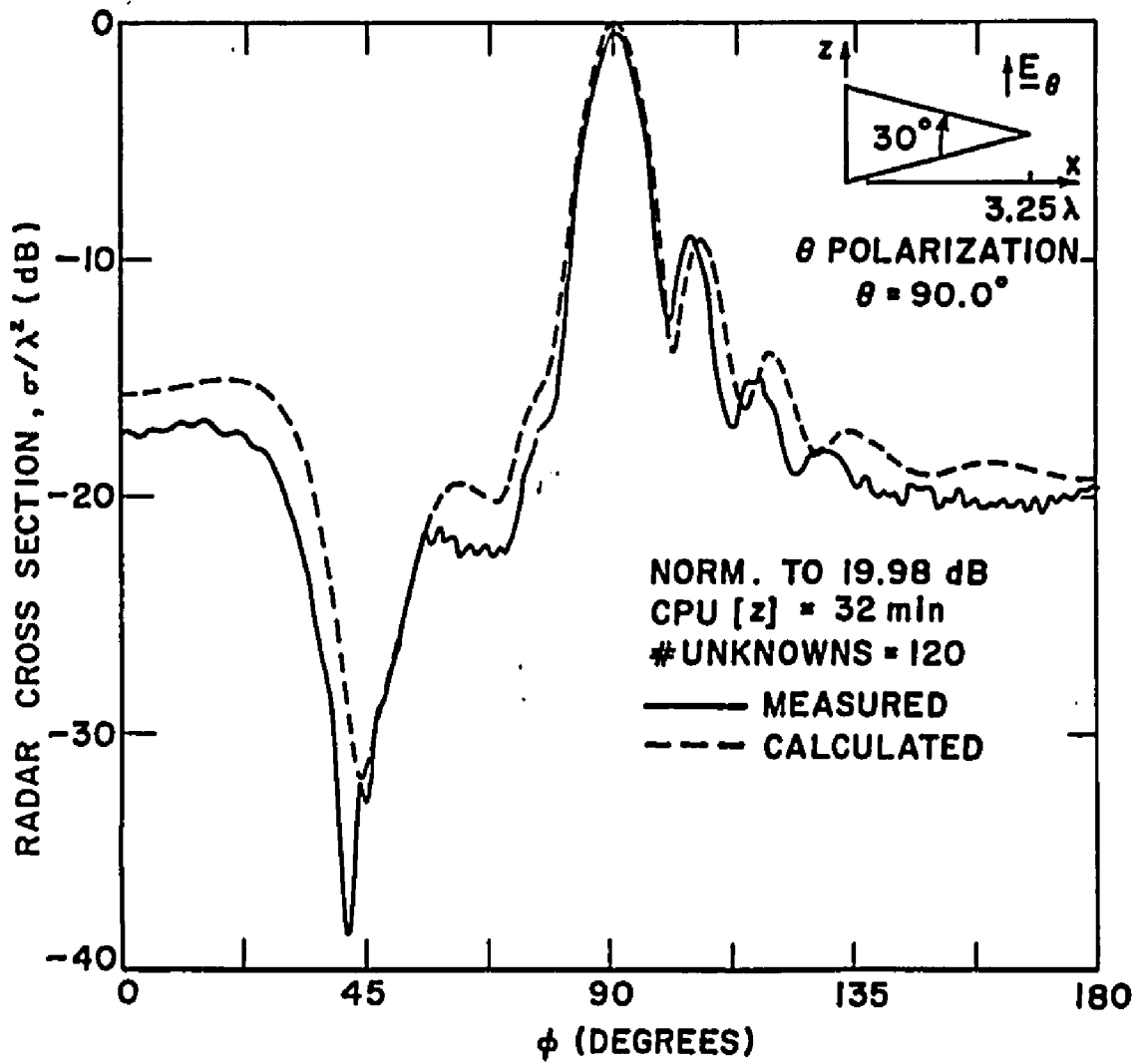


Figure 36. Backscatter from a 30° isosceles triangle with the height of 3.25λ (θ -polarization).

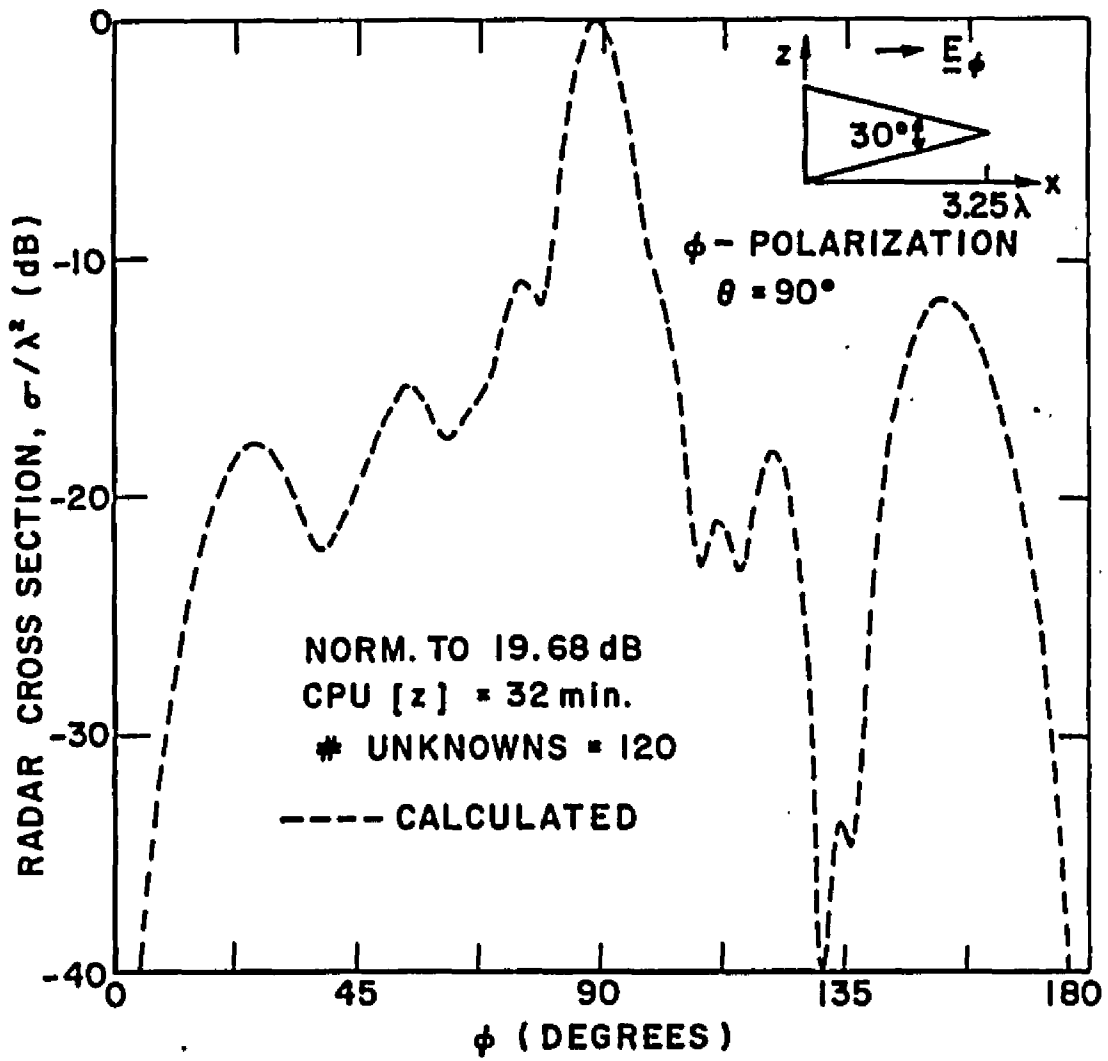


Figure 37. Backscatter from a 30° isosceles triangle with the height of 3.25λ (ϕ -polarization).

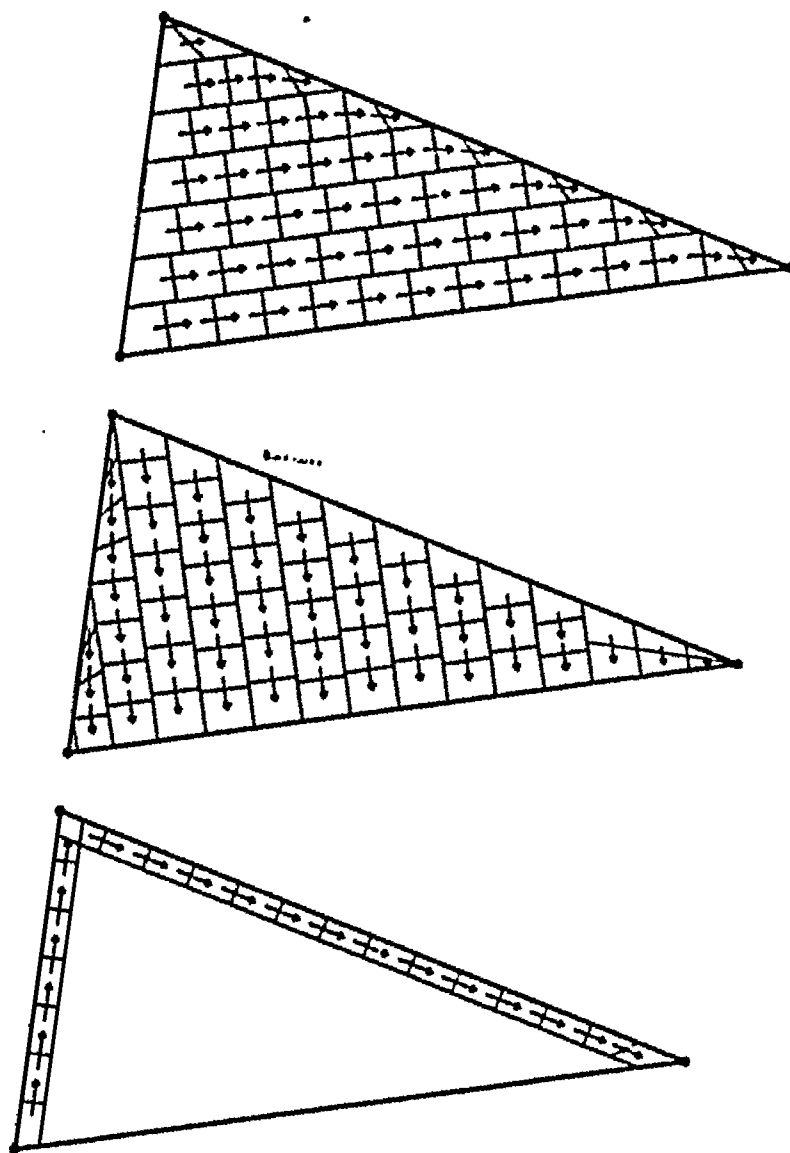


Figure 38. A set of overlapping surface-patch dipole modes formed in a 30° isosceles triangle by using subdivision method 2. This set of modes is used to generate the backscatter data in Figures 36 and 37.

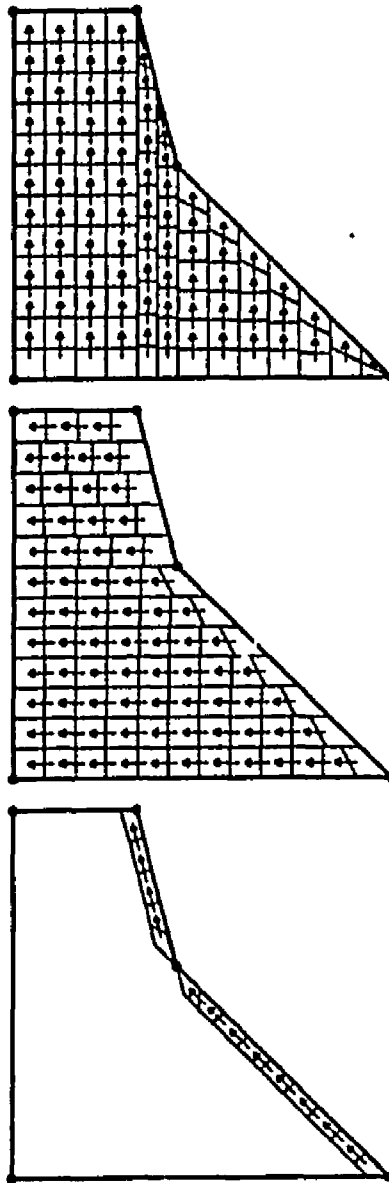


Figure 39. A set of overlapping surface-patch dipole modes formed inside a $3\text{-}\lambda$ fin-shaped polygon by using subdivision method 2. This set of modes is used to generate the backscatter data in Figures 40 and 41.

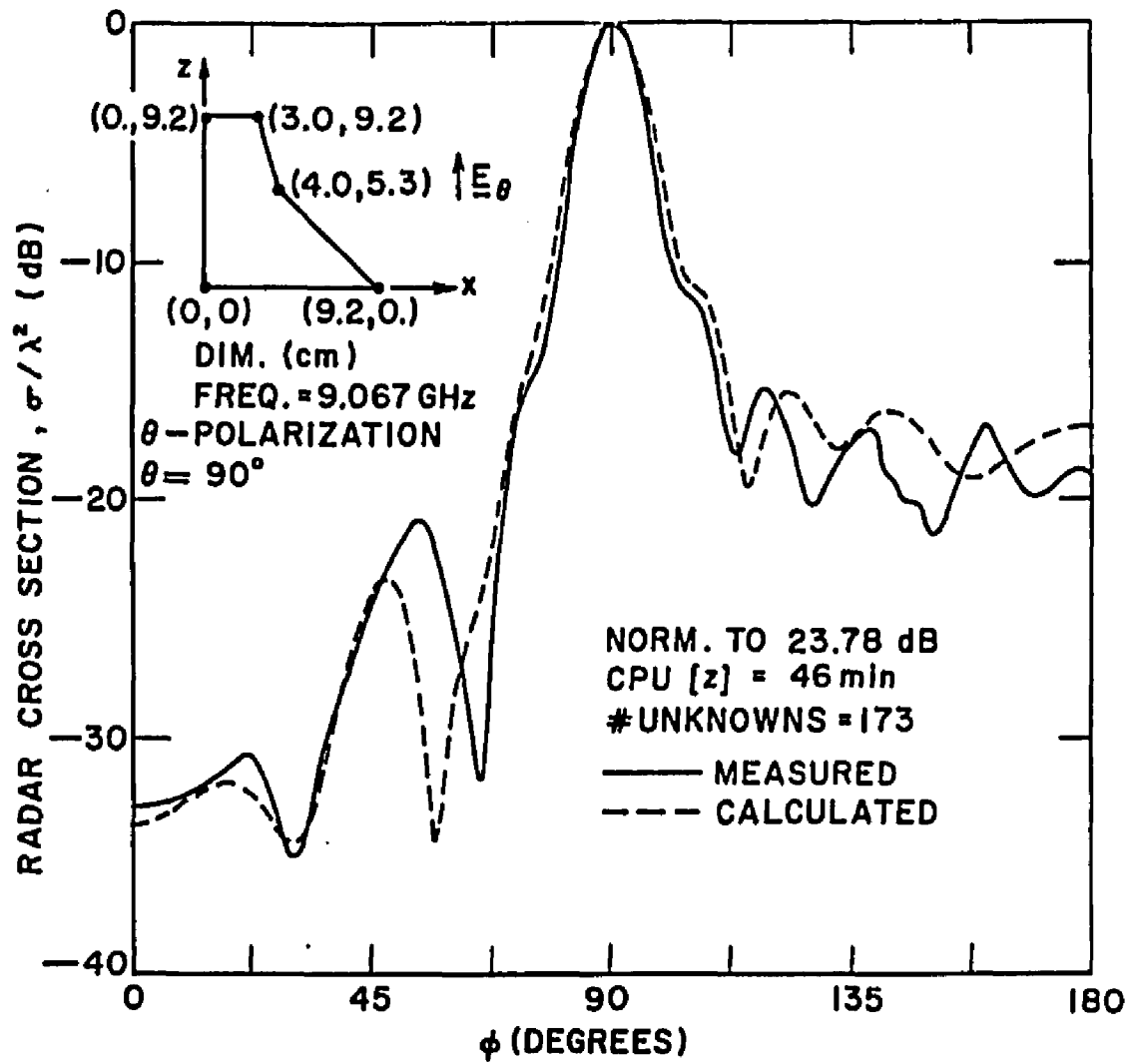


Figure 40. Backscatter from a 3λ fin-shaped plate (θ -polarization).

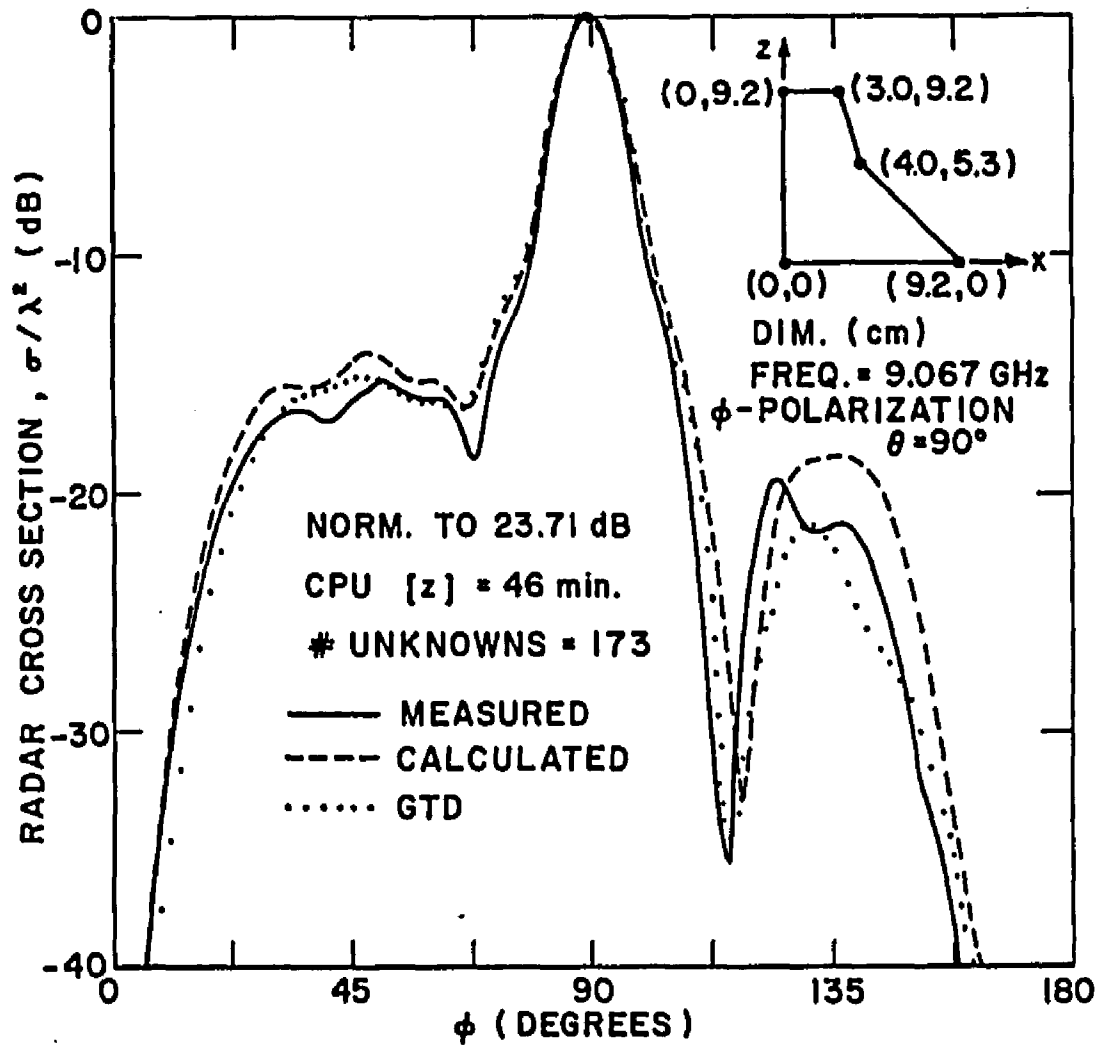


Figure 41. Backscatter from a 3λ fin-shaped plate (ϕ -polarization).

CHAPTER V

ANALYSIS OF MICROSTRIP ANTENNAS

This chapter will present an analysis of the microstrip antenna. Surface-patch dipole modes are used to model the microstrip patch and volume polarization currents for the dielectric slab. The nature of this problem requires unusually precise computation of the impedance matrix, but the method is capable of accurately predicting currents, impedance, and resonant frequency of the antenna.

A. Introduction

A microstrip antenna consists of a metallic plate or patch on an electrically thin grounded dielectric slab. The patch shapes, such as rectangular, circular, semicircular, trapezoidal, triangular, and pentagonal [32], have been fabricated in practical microstrip antennas. The patch can be fed either by a microstrip transmission line contacting an edge of the patch, or by a coaxial probe extending through the ground plane and contacting the patch (see Figures 42 and 43). There can be more than one feed point.

The microstrip antenna has a very low profile since its height above the ground plane is basically the dielectric substrate thickness. Except for the coaxial feedline, the antenna does not extend behind the ground plane. Its simple construction makes it very lightweight. These features allow microstrip antennas to be built conformal to the surface of an air- or spacecraft. Because the antenna is above the ground plane, it can be easily mounted to any vehicle without interfering with its internal structure. Microstrip phased arrays have also been built. In this case, the microstrip radiators and their associated microwave feed system (microstrip transmission lines) can be etched on a single surface. Thus, these antennas are inexpensive and simple to fabricate. Although typical bandwidths are in the order of a few percent, advantages can outweigh this shortcoming. A comprehensive report on the various aspects of microstrip antennas is given in reference [33].

Since the early work on microstrip antennas reported by Deschamps in 1953 [34] up to 1975, the analysis and design of these antennas were done by using simple models adapted from transmission line theory. Howell [35 and 36] modelled the microstrip antenna as a dielectric loaded cavity with magnetic side wall. Using this model, the resonant

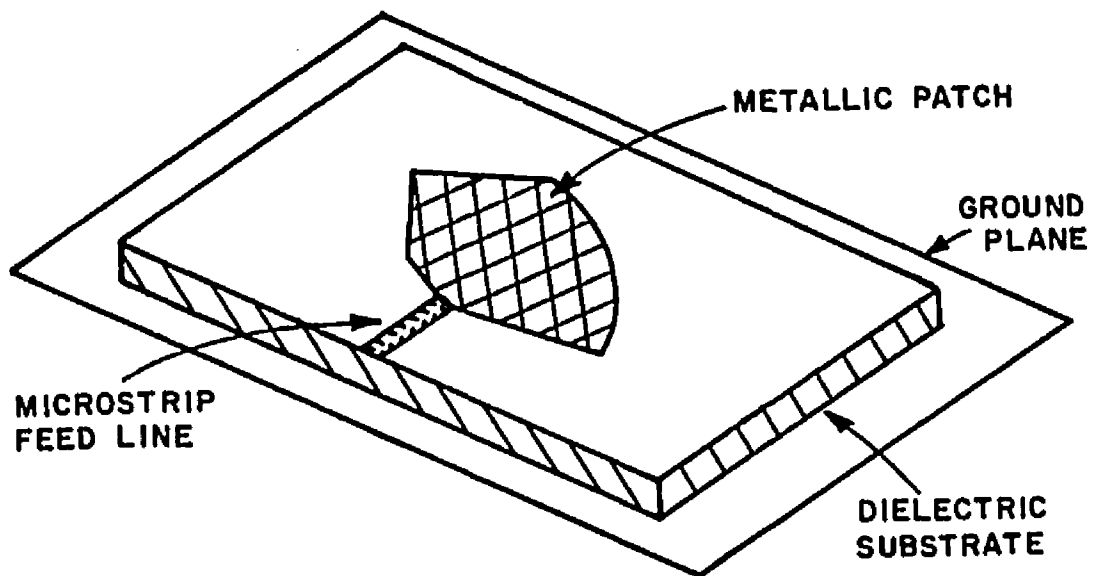


Figure 42. Perspective view of a microstrip antenna fed by microstrip transmission line.

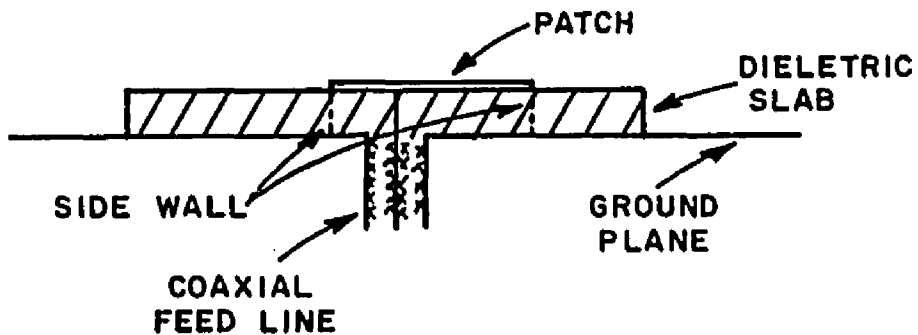


Figure 43. Side view of a microstrip antenna fed by coaxial line.

frequency for rectangular and circular microstrip patches can be predicted, but the input impedance at the feed has to be determined experimentally. Based on the same model and taking into account the fringing field, a more accurate expression for the resonant frequency of a circular disk was later given by Shen, *et al.*, [37]. Munson [38] and Derneryd [39] considered the microstrip antenna as two slots perpendicular to the feedline and separated by a very low impedance transmission line. The slots and the surface patch were modelled by an equivalent network, and transmission line theory was used to calculate the input impedance. This method was used to model rectangular microstrip patches fed at the center of an edge. The theory was extended by Derneryd [40] to account for different feed locations along the edge and the mutual conductance between the slots.

More recent work on microstrip antenna analysis is based on modelling the region between the patch and the ground plane as a resonant cavity. In this method, a complete set of eigenvectors which satisfy the wave equation and, therefore, can represent the fields inside the cavity must be found. If the patch shape is of a canonical form, the eigenvectors can be written in terms of known functions. In order to simplify the boundary condition at the side wall (see Figure 43), many investigators assume that the tangential component of the magnetic field (H) along the wall is negligible. Thus, the side wall becomes a magnetic wall. Using this model, Long, *et al.*, [41] analyzed the circular-disc microstrip antenna and derived the expressions for the far field, directive gain, efficiency, and the Q-factor of the antenna. An extension of this work was reported by Derneryd where the circular disk [42] and rectangular patch [43] were analyzed. A comprehensive work using this model was given by Lo, *et al.*, [44]. Here, solutions for numerous canonical shapes were given. It should be noted that the fringing field along the edge of the patch was taken into account either by using an effective dielectric constant for the substrate and/or a small extension in the dimension of the patch. An alternate approach to account for the fringing field is the use of an impedance boundary condition on the side wall. In other words, the side wall is no longer an open circuit (magnetic wall), but has an associated admittance (or radiating wall). Carver [45] incorporated this impedance condition for his model and derived the expression of the wall admittance for the rectangular and circular patch. In addition, Carver used the finite element method to solve the wave equation for arbitrarily shaped patches. Since the problem of finding the wall admittance for arbitrarily shaped patches was not solved, this latter technique did not include the impedance condition. C.M. Kaloj used the cavity resonator model to derive design equations which can be used for a conventional microstrip antenna as well as the "Twin Electric Microstrip Antenna," where identical microstrip patches are formed on both sides of a dielectric slab [55].

Agrawal and Bailey [46] modelled the microstrip patch and feedlines by using the thin wire grid. Using Richmond's thin wire computer code [3], a solution was first obtained for the antenna radiating in

the homogeneous medium having the permittivity of the dielectric substrate. The result was then shifted in frequency and the input impedance scaled by constants determined from measurements. This was a moment method approach, as is the approach used in the following analysis. However, surface patch modes are now used to model the microstrip antenna, and the presence of the dielectric is taken into account by the volume polarization current.

The three models described above can be contrasted by the types of unknowns that have to be determined. In the transmission line model, the unknowns are the characteristic impedance, propagation constant, and loads on an equivalent transmission line. The unknowns in the cavity model are the distribution of the cavity modes (or eigenfunctions) and the resonant frequencies of these modes (eigenvalues). In the moment method solution presented here, the unknowns are the surface currents flowing on the microstrip patch, and, if a dielectric slab is present, the equivalent volume polarization currents in the region occupied by the slab.

B. The Model

In this section, the model of the microstrip patch, the effect of the dielectric substrate, and the numerical difficulties will be discussed. The ground plane under the patch is assumed to be infinite and, thus, the image theory can be used. In this solution, the equivalent volume polarization currents in the dielectric slab are related to the surface charge density of the patch. Consequently, the surface current on the patch is the only unknown involved. As will be shown later, the current on the plate is inversely proportional to the difference of the self and mutual impedances of the patches. Since the difference between the two impedances is very small, both impedances have to be evaluated very accurately.

1. Air Dielectric Microstrip

Figure 44 shows the side view of an air dielectric microstrip patch antenna at a height T above a ground plane. The antenna is shown coaxially fed, although it could just as easily be edge fed. Using image theory, the ground plane is removed and the image of the patch and feed probe are inserted. The coaxial aperture is modelled by a delta gap voltage generator. This is shown in Figure 45. Generally, the currents at the wire/patch junction are modelled by the attachment mode discussed in Chapter Two. But our experience, and apparently the experience of others [44], indicates that the feed probe and voltage generator can be replaced by an impressed current filament given by

$$\underline{J}_1 = \hat{z} \text{ amp} \quad (35)$$

existing between the patches and constant in the \hat{z} direction.

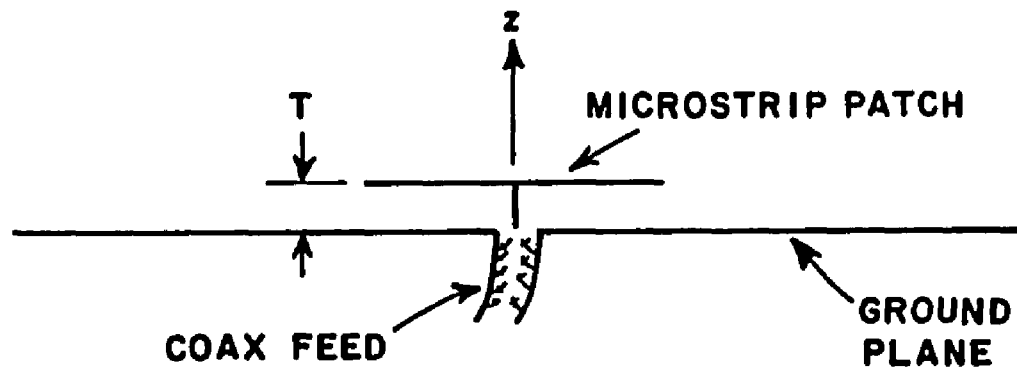


Figure 44. Side view of an air dielectric microstrip antenna fed by coaxial line.

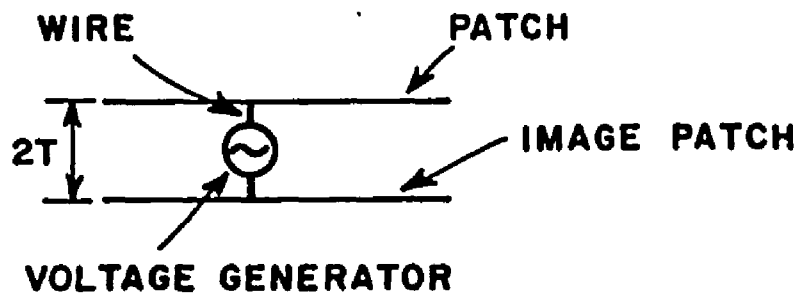


Figure 45. The model for the air dielectric microstrip antenna.

Figure 46 shows the geometry that can be analyzed using the moment method surface patch modelling technique described in Chapter Two. The dominant current on the patch is in the direction where the dimension of the patch is about one-half the wavelength in the dielectric medium. Thus, only one current dipole mode is used for each patch. In the case where the patch is close to being a square, the two orthogonal polarizations are needed. In this work, this problem is analyzed by solving for each current polarization independently, and the total input impedance is the sum of the individual input impedances. For each case, the impedance matrix, Equation (8), will have two unknowns.

It is well known that the close proximity of the plates in Figures 44 through 46 will cause the surface currents to distribute unevenly between the top and bottom surfaces of the plates. Actually, the majority of the current will be on the interior surfaces of the plates. This complexity is avoided in this present solution since the surface current, \underline{J}_s in Equation (6), is the vector sum of the currents on the top and bottom surfaces (see Chapter Two). This is the current which radiates and is, therefore, of primary interest in any solution.

2. Modification for Dielectric Slab

It will now be shown how the matrix equation for the air dielectric microstrip can be modified to account for the dielectric slab (or substrate). Figure 47 shows the geometry of Figure 46, but with a dielectric slab of permittivity ϵ , or relative permittivity $\epsilon_r = \epsilon/\epsilon_0$, between the plates. Using the volume equivalence theorem, the slab is removed and replaced by free space and the equivalent volume polarization currents (see Figure 48)

$$\underline{J}_V = j\omega(\epsilon - \epsilon_0) \underline{E} \quad (36)$$

where \underline{E} is the actual electric field in the slab. Note that \underline{J}_V exists only in the region previously occupied by the slab. \underline{J}_V is unknown since \underline{E} is unknown. \underline{J}_V can be treated as another set of independent unknowns and expanded in terms of N_V basic functions. The coefficients in the expansion for \underline{J}_s and \underline{J}_V are determined by solving a system of $N + N_V$ simultaneous equations [47]. However, the additional unknowns, and consequently the increase in computation time, made this technique unattractive for this problem. An alternative approach used in this work is to treat \underline{J}_s and \underline{J}_V as dependent unknowns [48 and 49]. With the slab, the RIE (6) becomes

$$- \oint_S (\underline{J}_s \cdot \underline{E}_m) ds - \iiint_{V_d} (\underline{J}_V \cdot \underline{E}_m) dV = V_m \quad (37)$$

where V_d is the volume occupied by the slab and \underline{E}_m is still the field in free space. Assuming that the field inside the dielectric slab due to the surface patch current expansion mode can be found, \underline{J}_V is

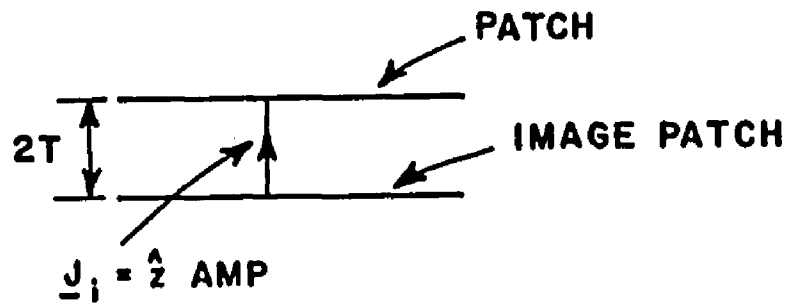


Figure 46. The voltage generator in Figure 45 is replaced by 1-amp impressed current filament.

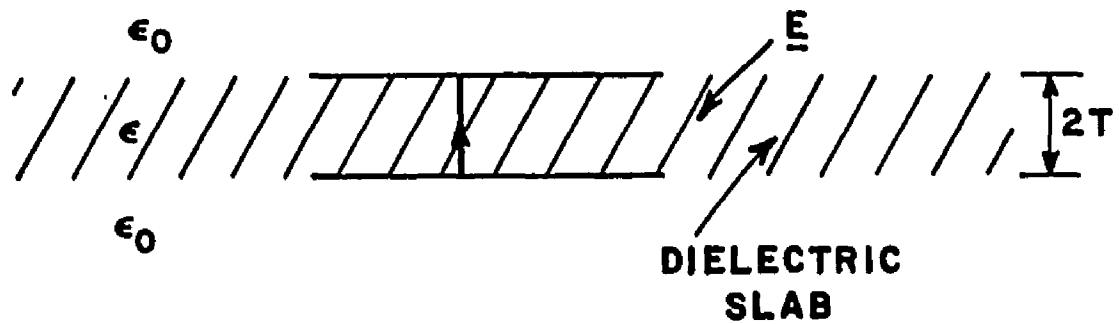


Figure 47. Microstrip antenna with dielectric slab.

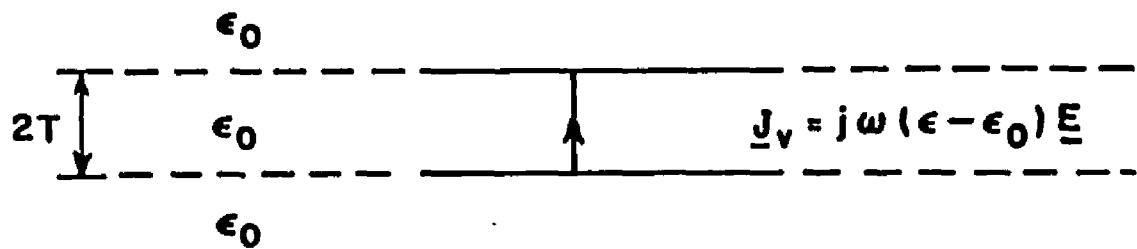


Figure 48. The dielectric slab is modelled by equivalent volume polarization current.

made dependent on \underline{J}_s by expressing the currents in Equation (37) by the expansion modes

$$\underline{F}_n = \underline{F}_n^C + \underline{F}_n^P \quad (38)$$

where \underline{F}_n^C is the surface conduction current and \underline{F}_n^P is the volume polarization current,

$$\underline{F}_n^P = j\omega(\epsilon - \epsilon_0) \underline{E}_n^d \quad (39)$$

where \underline{E}_n^d is the field in the dielectric due to the n^{th} expansion mode, \underline{F}_n^C . Using Equations (36), (38), and (39), the RIE (37) can be expressed by the matrix equation

$$\sum_{n=1}^N I_n (z_{mn} + \Delta z_{mn}) = V_m; \quad m = 1, 2, \dots, N \quad (40)$$

where z_{mn} and V_{mn} are defined by Equations (9) and (10), respectively, and

$$\Delta z_{mn} = -j\omega(\epsilon - \epsilon_0) \iiint_{V_2} \underline{E}_n^d \cdot \underline{E}_m \quad dV \quad (41)$$

N is the total number of surface patch current expansions. While the integral in Equation (41) in theory extends over the entire volume of the slab, in practice it is sufficient to integrate a few slab thicknesses beyond the region shared by modes m and n . Although the expression for \underline{E}_n^d in terms of Sommerfeld integrals can be found [50], here we make some simplifying approximations.

Assuming that only the \hat{z} component of \underline{E}_n^d is significant in the slab, the procedure for computing \underline{E}_n^{dz} will now be presented. Figure 49 shows \underline{J}_n radiating in the presence of the dielectric slab. The surface charge density associated with \underline{J}_n is obtained using the equation of continuity

$$\nabla \cdot \underline{J}_n = -j\omega \rho_{sn} \quad (42)$$

or

$$\rho_{sn} = \frac{-\nabla \cdot \underline{J}_n}{j\omega} \quad (43)$$

where ρ_{sn} is the surface charge density associated with \underline{J}_n . From the boundary condition

$$D_1 + D_2 = \rho_{sn} \quad (44)$$

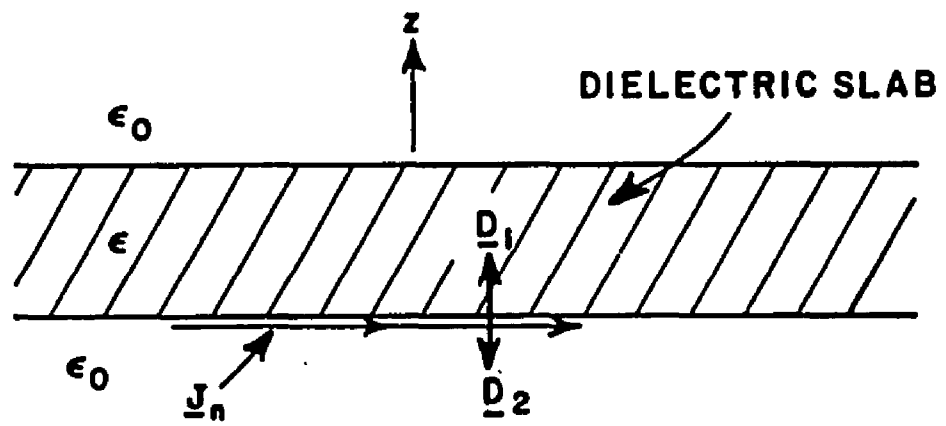


Figure 49. \underline{J}_n in the presence of the dielectric slab.

and if we were to assume $D_1 = D_2 = D_0$, the flux density radiated in a homogeneous medium (regardless of its permittivity), then Equation (43) would become

$$D_0 = \rho_{sn}/2 = \frac{-\nabla \cdot \underline{J}_n}{2j\omega} \quad (45)$$

Finally, the electric field at the slab surface would be

$$E_n^{dz} = D_0/\epsilon = \frac{-\nabla \cdot \underline{J}_n}{2j\omega\epsilon} \quad (46)$$

The major approximation involved in obtaining Equation (46) was the assumption $D_1 = D_2 = D_0$. Actually, the presence of the slab causes a significant asymmetry; that is, $D_1 > D_0 > D_2$. Equation (46) can be modified to include this effect as

$$E_n^{dz} = RD_0/\epsilon = \frac{-R\nabla \cdot \underline{J}_n}{2j\omega\epsilon} \quad (47)$$

where the ratio $R = D_1/D_0$ can be evaluated using the method of dielectric images [54] and is derived in Appendix B. Figure 50 illustrates a typical asymmetry of the D_z fields at the surface of a slab. R is evaluated very close to the surface patch and has been shown to be accurate for very thin slabs ($T < 0.01\lambda$). However, for thicker slabs, the final results begin to deteriorate and this is caused by the approximation for E_n^{dz} .

Equation (47) predicts that E_n^{dz} at the surface of the slab is R times the field radiated by \underline{J}_n in a homogeneous medium of permittivity ϵ . We use the approximation that E_n^{dz} , at any point in the slab, is R times the field radiated by \underline{J}_n in a homogeneous medium of permittivity ϵ .

The excitation column could be evaluated using Equations (10) and (35), i.e.

$$V_m = \int_0^{2T} \underline{E}_m \cdot \underline{J}_i \, dz \quad (48)$$

if \underline{E}_m is taken to be the field of the m^{th} test mode in the presence of the dielectric slab. We would like to use Equation (48) with \underline{E}_m still the free space field of the m^{th} test mode. Using the results of Equation (47), this can be done by evaluating the V_m using Equation (48) and then multiplying by R/ϵ_r .

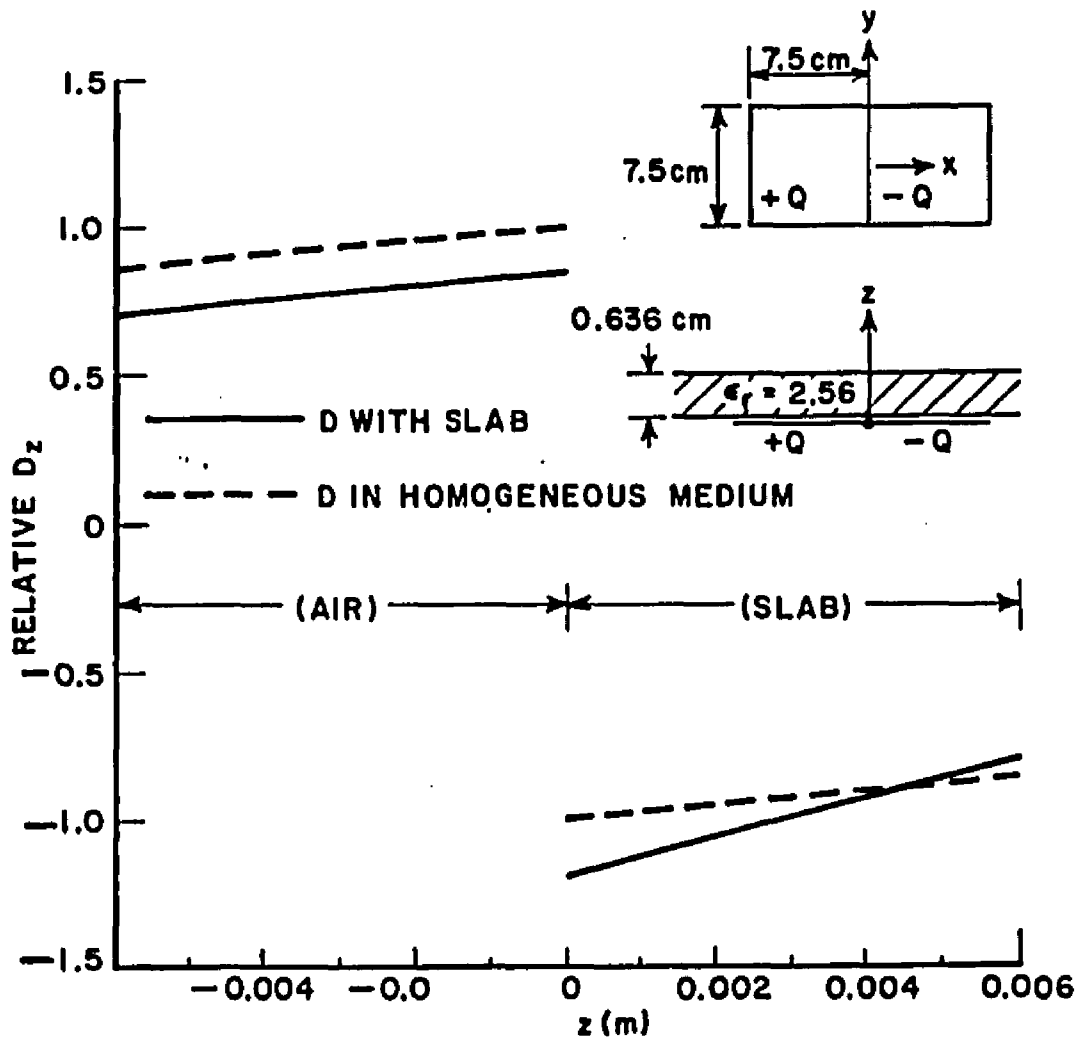


Figure 50. Relative D_z field along the line $x = 3.75$ cm. and $y = 0$.

Once the patch currents are known, it is straight forward to evaluate the input impedance at the feed point. Since the feed current is taken as one amp, the input impedance is numerically equal to the voltage at the feed point, or

$$z_{in} = \frac{1}{2} \sum_{n=1}^N I_n V_n \quad (49)$$

where the factor $\frac{1}{2}$ is a result of the use of image theory to model the antenna. If the antenna is coaxially fed (rather than edge fed by microstrip line), the effects of the probe can be included by adding [45]

$$jx_n = j \frac{376}{\sqrt{\epsilon_r}} \tan \left(\frac{2 \pi T \sqrt{\epsilon_r}}{\lambda_0} \right) \quad (50)$$

to z_{in} .

3. Expansion and Test Modes

The expression for surface patch modes used for the microstrip is given by Equation (12). Normally, we choose $k = \omega \sqrt{\mu_0 \epsilon_0} = 2\pi/\lambda_0$, where λ_0 is the free-space wavelength [13 and 16]. In theory, the moment method should converge to the same result regardless of any reasonable choice for k . Here we choose

$$k = \omega \sqrt{\mu_0 \epsilon_e} \quad (51)$$

where ϵ_e is the effective dielectric constant given by [51]

$$\epsilon_e = \frac{\epsilon + 1}{2} + \frac{\epsilon - 1}{2} \left(1 + \frac{10T}{w} \right)^{-k} \quad (52)$$

where w is the width of the microstrip. The choice of k primarily effects the convergence of the impedance level rather than the resonant frequency. This convergence can be especially slow for a poor choice of k since the impedance level is essentially proportional to the divergence or slope of the microstrip patch surface current density at the feed point.

4. Numerical Difficulties

The moment method solution for microstrip antennas requires the unusually precise computation of the elements in the impedance matrix.

Consider the air dielectric microstrip of Figure 46. If we let the subscript b refer to a single mode on the bottom or image patch and the subscript t refer to a single mode on the top patch, then

$$I_b Z_{bb} + I_t Z_{bt} = V_b \quad (53)$$

$$I_b Z_{tb} + I_t Z_{tt} = V_t \quad (54)$$

If we assume that modes b and t are both pointing to the right, then from image theory we know $I_t = -I_b$. Also, from the symmetry of the problem $Z_{tt} = Z_{bb}$, $Z_{tb} = Z_{bt}$, and $V_t = -V_b$. In this case, Equations (53) and (54) can be solved as

$$I_t = -I_b = \frac{V_t}{Z_{tt} - Z_{tb}} \quad (55)$$

Equation (55) shows that the solution is critically dependent upon the difference between the self and mutual impedance of the top and bottom modes. Since modes b and t are identical, except that they are shifted by typically 0.01λ , we expect that $Z_{tt} \approx Z_{tb}$. Thus, obtaining $Z_{tt} - Z_{tb}$ accurately is a difficult numerical problem.

As an example, Table 1 shows Z_{tt} , Z_{tb} and related quantities for the microstrip shown in Figure 51, except that $\epsilon_r = 1$. Data are shown at the three frequencies 952.0, 963.0, and 974.0 MHz which are below, at, and above resonance, respectively. (The data in Table 1 and 2 do not include contributions from losses in the plates or the dielectric.)

Note that the self resistance is always slightly larger than the mutual resistance. This difference controls the level of the plate currents and of the input impedance, with both increasing as the difference becomes smaller. The self reactance is smaller than the mutual reactance below resonance, but larger above. At resonance the self and mutual reactances are equal, and $Z_{tt} - Z_{tb}$ is purely real. Since the elements in the voltage vector are essentially purely imaginary, Equation (55) shows that, at resonance, the currents are maximum and essentially purely imaginary. Finally, from Equation (49), it can be seen that at resonance the impedance is maximum and real.

Next, consider the same antenna, except with the dielectric slab. Table 2 shows Z_{tt} , Z_{tb} , ΔZ_{tt} , and ΔZ_{tb} and related quantities at the frequencies 630.0, 634.0, and 638.0 MHz which are below, at, and above resonance, respectively. Note that $\text{Re}(Z_{tt})$ is always larger than $\text{Re}(Z_{tb})$, but by only a few hundredths of an ohm. Also, $I_m(Z_{tt})$ is less than $I_m(Z_{tb})$ by about 16 ohms. Thus, without the ΔZ dielectric correction terms we are very far from resonance. In this example, $\Delta Z_{tt} = -\Delta Z_{tb}$ is about j8 ohms. With this correction, $Z_{tt} + \Delta Z_{tt}$

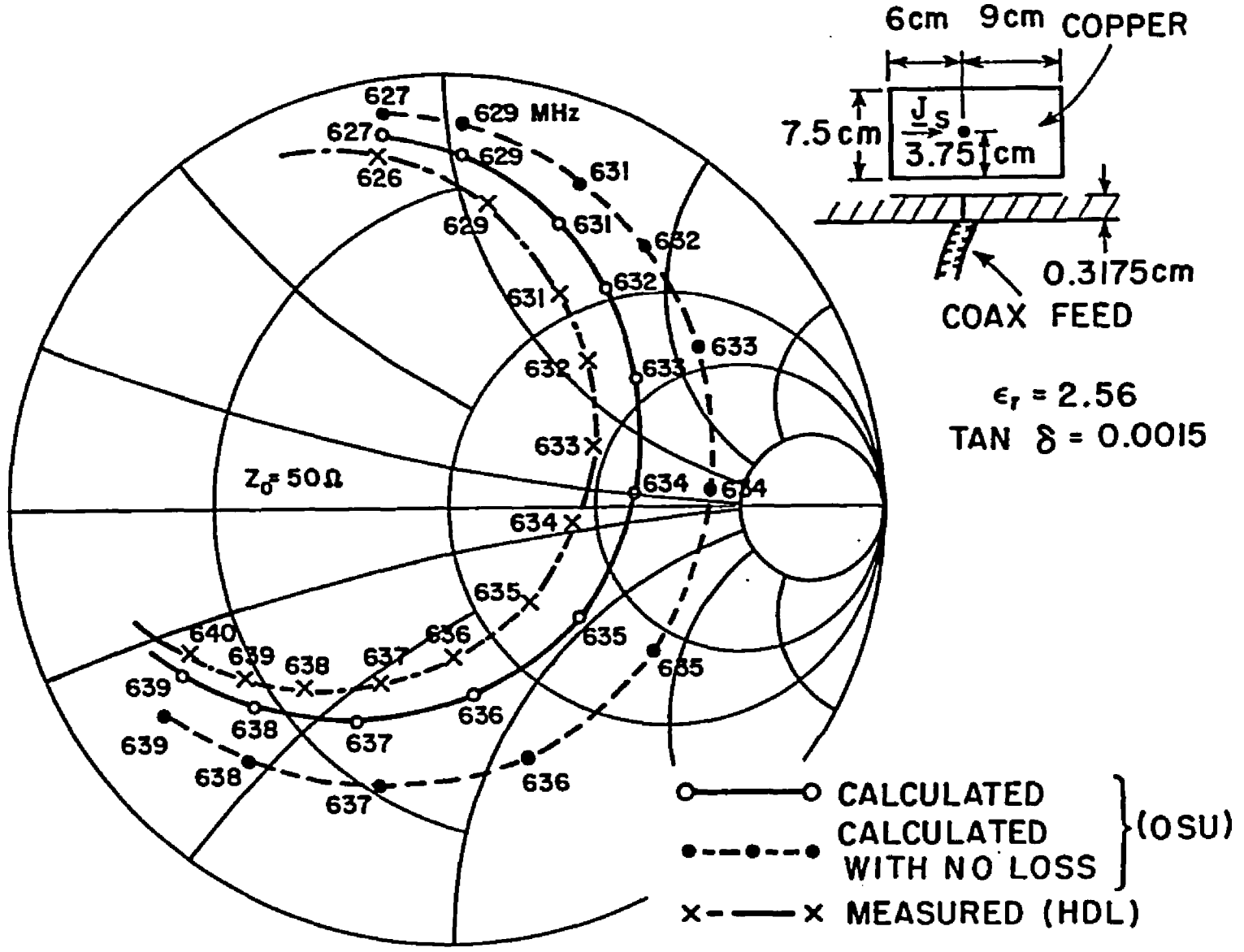


Figure 51. Input impedance of rectangular microstrip antenna.

TABLE 1

ELEMENTS IN THE FREE SPACE LOSSLESS MICROSTRIP IMPEDANCE MATRIX

f(MHz)	Z_{tt}	Z_{tb}	$Z_{tt}-Z_{tb}$
952.0	58.91+j5.80	58.71+j6.32	.21-j.52
963.0	60.76+j7.80	60.54+j7.80	.22+j0
974.0	62.65+j9.78	62.43+j9.27	.22+j.53

TABLE 2

ELEMENTS IN MICROSTRIP IMPEDANCE MATRIX INCLUDING DIELECTRIC SLAB (LOSSLESS CASE)

f(MHz)	Z_{tt}	Z_{tb}	$Z_{tt}-Z_{tb}$	$\Delta Z_{tt}=-\Delta Z_{tb}$	$Z_{tt}+\Delta Z_{tt}$	$(Z_{tt}+\Delta Z_{tt})$ $-(Z_{tb}+\Delta Z_{tb})$
630.0	21.81-j62.74	21.78-j45.81	.03-j16.93	j8.39	21.81-j54.35	.03-j.15
634.0	22.12-j61.69	22.08-j44.99	.04-j16.69	j8.35	22.12-j53.34	.04+j0
638.0	22.43-j60.63	22.40-j44.18	.03-j16.45	j8.30	22.43-j52.33	.03+j.15

is nearly equal to $Z_{tb} + \Delta Z_{tb}$ near resonance. At resonance $(Z_{tt} + \Delta Z_{tt}) - (Z_{tb} + \Delta Z_{tb})$ is purely real and equal to about 0.03 ohms.

Tables 1 and 2 illustrate the accuracy required to obtain accurate current or impedance data. In Table 2, the self and mutual resistance must be evaluated to an accuracy of about 0.05 percent or better, in order that their difference of 0.04 ohms be reasonably accurate. Also, Table 2 shows that a combined error of 1 ohm in Z_{tt} , Z_{tb} , and ΔZ_{tt} will lead to a shift in the resonant frequency of about 27 MHz, or about a four percent shift.

Losses in the finitely conducting patches and in the dielectric can significantly effect the current and impedance level and bandwidth of the microstrip antenna. The finite conductivity of the patches, whose treatment is analogous to that of thin wires[19], increases the self resistance while leaving the mutual resistance unchanged. Losses in the dielectric are treated by simply allowing ϵ to be complex in Equation (41). The result is to increase the self resistance and decrease the mutual resistance by equal amounts. Thus, in both cases, the losses increase the difference between the self and mutual resistances. For reasonably low loss materials, the changes will be a tiny fraction of an ohm. However, this change will be significant, to the current and input impedance, if it is comparable to the difference between the self and mutual resistance for the lossless antenna; i.e. for the example shown in Table 2, 0.04 ohms. Note that this strong dependence of the current level on the losses suggests that it may be inaccurate to use the loss free currents and fields in perturbation technique to evaluate the losses in the plates and dielectric.

C. Numerical Results

In this section, computations, based upon the results of the previous section, will be presented and compared to measurements and previous computations. All of the present results were made using the same user oriented computer code. The computations in Figures 51 through 53 were made with one unknown, while two unknowns were required in Figure 54.

Figure 51 shows a coaxially fed rectangular microstrip of length 15 cm. and width 7.5 cm. The dielectric slab is 1/8 inch thick and with relative permittivity $\epsilon_r = 2.56$. Figure 51 shows good agreement for the measured and computed input impedance in terms of impedance level, resonant frequency, and bandwidth (note: the measurements in Figures 51 and 52 were made by D.H. Schaubert at Harry Diamond Laboratories). Also shown in Figure 51 is the computed impedance for the same antenna, except all losses are removed (i.e. plates have perfect conductivity and dielectric $\tan \delta = 0$). Note the substantial increase in impedance level. Figure 52 shows a trapezoidal microstrip patch, identical to that in Figure 51, except that the width varies from 2.5 to 10 cm. Note that the theoretical model accurately predicts

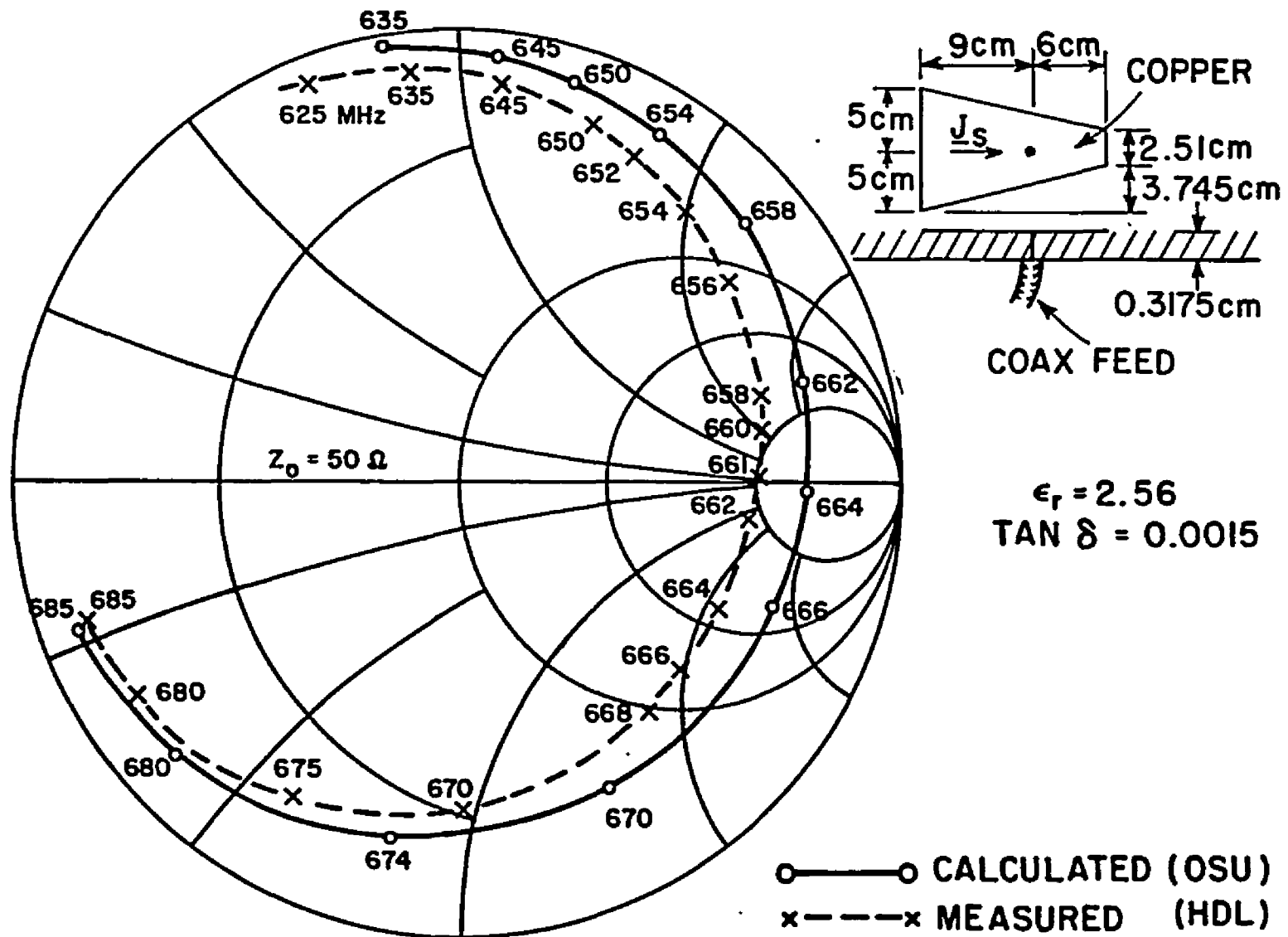


Figure 52. Input impedance of trapezoidal microstrip antenna.

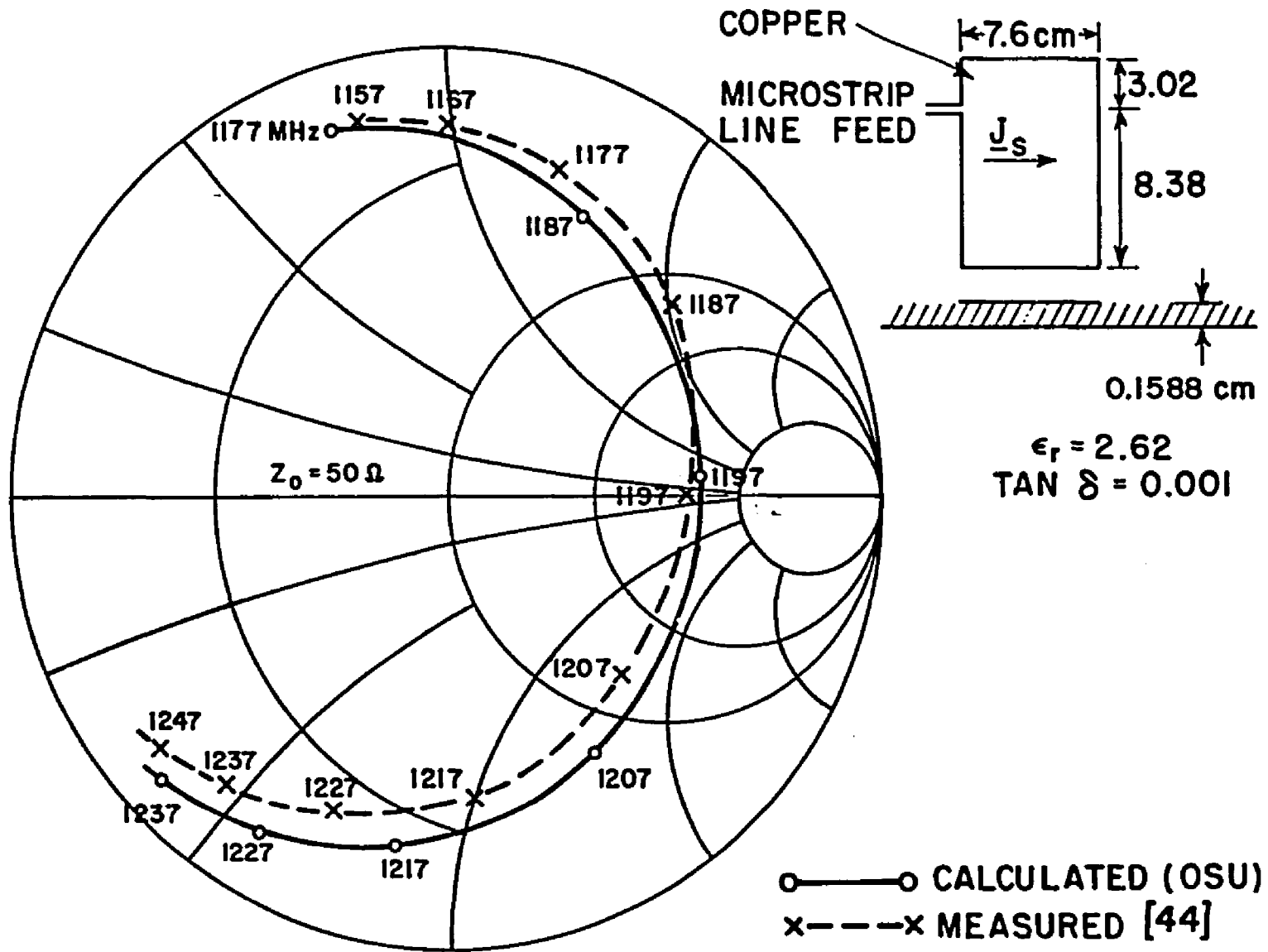


Figure 53. Input impedance of rectangular microstrip antenna.

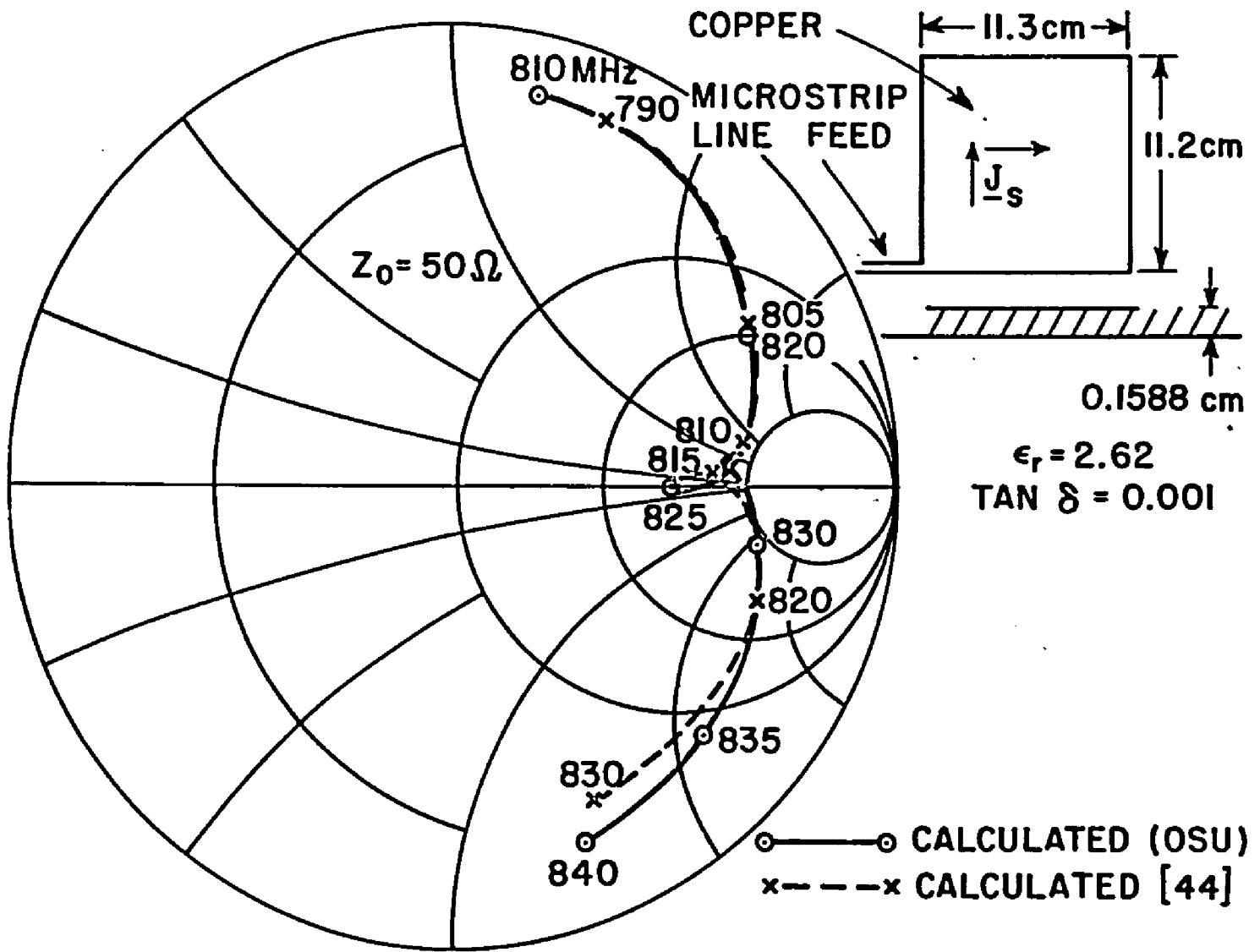


Figure 54. Input impedance of almost square microstrip antenna.

the upward shift in resonant frequency. Figure 53 compares the input impedance of a rectangular edge fed microstrip of length 7.6 cm. and width 11.4 cm. computed by the present theory to that measured by Lo, et al., [44]. The dielectric slab is 1/16 inch thick with relative permittivity $\epsilon_r = 2.62$. Finally, Figure 54 shows the input impedance for a nearly square corner fed microstrip of dimension 11.3 by 11.2 cm., and with the same slab as Figure 53. The cusp in the curve is caused by the resonance associated with the 11.3 cm. side being at 823 MHz, while that of the 11.2 cm. side is nearly the same at 829.5 MHz.

D. Discussion

A surface patch moment method solution for the microstrip antenna has been presented. The microstrip plates or patches are modelled by equivalent surface currents, while the dielectric slab is modelled by equivalent volume polarization currents. Numerical examples illustrate that the technique can predict with good accuracy the input impedance of edge and coaxially fed rectangular and nonrectangular microstrip antennas. Losses in the plates and in the dielectric are included and have a significant effect on the bandwidth and impedance level.

An interesting feature of the moment method solution is the unusual precision required in the computation of the elements in the impedance matrix. It is felt that this is, in part, a consequence of the nature of the moment method model. In particular, the fields and currents in a microstrip antenna are very nearly those of a closed cavity. In the moment method, the structure is modelled by a number of plates, which are basically open radiators. It is hoped that by enforcing boundary conditions on the plates that the solution will "see" the closed or cavity nature of the structure. In fact, it does; however, the description of the plates and their location is required to be very precise. A second explanation comes from consideration of Equations (53) and (54). Equation (53) enforces (in an approximate sense) the boundary condition that the tangential electric field vanishes on the bottom or image plate. Equation (54) enforces the boundary condition that the tangential electric field vanishes on the top plate. Since the top and bottom plates are separated by typically only 0.01λ , Equations (53) and (54) are enforcing, to a large extent, the identical conditions. Yet accurately solving Equations (53) and (54) is dependent upon them "seeing" the relatively small difference between these conditions. The result, illustrated in Equation (55), is that the solution is critically dependent upon the relatively small differences between the self and mutual impedances.

Considerable comparisons have been made between the moment method solution presented here and transmission line and modal solutions for planar rectangular microstrips. Although the moment method solution is more complex, it is not significantly more accurate. The

advantage of the moment method solution may be in its adaptability to the more involved problems of conformal or coupled microstrip antennas.

CHAPTER VI

CONCLUSION

A formulation, based on the RIE with electric test source, for analyzing electromagnetic antenna and scattering problems has been presented. The use of quadrilateral piecewise sinusoidal surface patch modes, thin-wire modes, and the wire/plate attachment modes allows a large class of problems associated with arbitrarily shaped surfaces to be analyzed. Special attention has also been given to the problem of automatically setting the surface-patch dipole modes for a general polygon. The applicability and versatility of this formulation has been demonstrated for a wide range of problems, including monopole antenna on a disk, scattering from polygonal plates, and analysis of microstrip antennas.

A. Topics for Further Work

Although the computer code developed for this work can handle any plate geometry, considerable reduction in the computation time could result if this code is integrated into the well developed and efficient user oriented code for rectangular patches. This savings in time is obtained by the new code's ability to identify the rectangular plates and applying the topelitz-like properties of the rectangular surface-patches in evaluating the mutual impedances.

Another topic for further investigation is the use of Sommerfeld's method to find the Green's function of a surface-patch on a dielectric substrate. This formulation is more general than the method presented in the analysis of the microstrip antenna in that it can treat electrically thick, as well as thin, dielectric slabs and the patch can be on the slab or imbedded in the slab.

BIBLIOGRAPHY

1. V.H. Rumsey, "Reaction Concept in Electromagnetic Theory," *Physical Review*, Vol. 94, June 15, 1954, pp. 1483-1491.
2. A.J. Poggio and E.K. Miller, "Integral Equation Solutions of Three-Dimensional Scattering Problems," in Computer Techniques for Electromagnetics, R. Mittra, editor, New York: Pergamon, 1973, Chapter 4.
3. J.H. Richmond, "Computer Program for Thin-wire Structures in a Homogeneous Conducting Medium," Technical Report 2902-12, August 1973, The Ohio State University ElectroScience Laboratory, Department of Electrical Engineering; prepared under Grant No. NGL 36-008-138 for National Aeronautics and Space Administration (NASA-CR-2399).
4. H.H. Cho and B.S. Strait, "Computer Programs for Radiation and Scattering by Arbitrary Configurations of Bent Wires," Scientific Report No. 7, AFCRL-70-0374, Syracuse University, Syracuse, New York, September 1970.
5. G.J. Burke and A.J. Poggio, "Numerical Electromagnetic Code (NEC) - Method of Moments," Naval Ocean System Center, Technical Document 116, AFWL-TR-76-320, July 1977.
6. J.H. Richmond, "A Wire-Grid Model for Scattering by Conducting Bodies," *IEEE Trans. Antennas and Propagation*, Vol. AP-14, November 1966, pp. 782-786.
7. E.K. Miller and F.J. Deadrick, "Some Computational Aspects of Thin-Wire Modelling," in Numerical and Asymptotic Techniques in Electromagnetics, R. Mittra, editor, New York: Springer-Verlag, 1975, Chapter 4.
8. F.K. Oshiro, "Source Distribution Techniques for the Solution of General Electromagnetic Scattering Problems," *Proceedings First GISAT Symposium*, Mitre Corp., Vol. I, 1965, pp. 83-107.
9. D.L. Knepp and J. Goldhirsh, "Numerical Analysis of Electromagnetic Radiation Properties of Smooth Conducting Bodies of Arbitrary Shape," *IEEE Trans. Antennas and Propagation*, Vol. AP-20, May 1972, pp. 383-388.

10. N.C. Albertsen, J.E. Hansen, and N.E. Jensen, "Computation of Radiation from Wire Antennas on Conducting Bodies," IEEE Trans. Antennas and Propagation, Vol. AP-22, March 1974, pp. 200-206.
11. G.J. Burke and A.J. Poggio, "Numerical Electromagnetic Code (NEC) - Method of Moments," Naval Ocean Systems Center, Technical Document 116, AFWL-TR-76-320, July 1977.
12. J.J.H. Wang, "Numerical Analysis of Three-Dimensional Arbitrarily-Shaped Conducting Scatterers by Trilateral Surface Cell Modelling," Radio Science, Vol. 13, November-December 1978, pp. 947-952.
13. N.N. Wang, J.H. Richmond, and M.C. Gilreath, "Sinusoidal Reaction Formulation for Radiation and Scattering from Conducting Surfaces," IEEE Trans. Antennas and Propagation, Vol. AP-23, May 1975, pp. 376-382.
14. A. Sankar and T.C. Tong, "Current Computation on Complex Structures by Finite-Element Method," Electronics Letters, Vol. 11, October 1975, pp. 481-482.
15. D.R. Wilton, S.S.M. Rao, and A.W. Glisson, "Electromagnetic Scattering by Surfaces of Arbitrary Shape," RADC-TR-79-325, University of Mississippi, March 1980.
16. E.H. Newman and D.M. Pozar, "Electromagnetic Modelling of Composite Wire and Surface Geometries," IEEE Trans. Antennas and Propagation, Vol. AP-26, November 1978, pp. 784-789.
17. J. Singh and A.T. Adams, "A Nonrectangular Patch Model for Scattering from Surfaces," IEEE Trans. Antennas and Propagation, Vol. AP-27, July 1979, pp. 531-535.
18. S.A. Schelkunoff, "On Diffraction and Radiation of Electromagnetic Waves," Physical Review, Vol. 56, August 15, 1939, pp. 308-316.
19. J.H. Richmond, "Radiation and Scattering by Thin-Wire Structures in the Complex Frequency Domain," Report 2902-10, July 1973, The Ohio State University ElectroScience Laboratory, Department of Electrical Engineering; prepared under Grant No. NGL 36-008-138 for National Aeronautics and Space Administration (NASA-CR-2396).
20. W.A. Davis and R. Mittra, "A New Approach to the Thin Scatterer Problem Using the Hybrid Equations," IEEE Trans. Antennas and Propagation, Vol. AP-25, May 1977, pp. 402-406.
21. E.H. Newman and D.M. Pozar, "Considerations for Efficient Wire/Surface Modelling," IEEE Trans. Antennas and Propagation, Vol. AP-28, January 1980, pp. 121-125.

22. J.H. Richmond and N.H. Geary, "Mutual Impedance of Nonplanar-Skew Sinusoidal Dipoles," IEEE Trans. Antennas and Propagation, Vol. AP-23, May 1975, pp. 412-414.
23. W.J. Gordon and C.A. Hall, "Construction of Curvilinear Coordinate Systems and Applications to Mesh Generation," International Journal for Numerical Methods in Engineering, Vol. 7, 1973, pp. 461-477.
24. D.S. Jones, The Theory of Electromagnetism, New York: Pergamon, 1964, pp. 566-569.
25. D.M. Pozar and E.H. Newman, "Analysis of a Monopole Mounted Near or At the Edge of a Half-Plane," submitted for publication in the IEEE Trans. Antennas and Propagation.
26. J.H. Richmond, "On the Edge Mode in the Theory of TM Scattering by a Strip or Strip-Grating," IEEE Trans. Antennas and Propagation, Vol. AP-28, November 1980, pp. 883-887.
27. E.E. Okon and R.F. Harrington, "The Capacitance of Discs of Arbitrary Shape," Technical Report No. 10, April 1979. The Department of Electrical and Computer Engineering, Syracuse University; prepared under Contract No. N00014-76-C-0225 for the Office of Naval Research, Department of the Navy.
28. J.H. Richmond, "Monopole Antenna on Circular Disk," Technical Report 711639-1, July 1979, The Ohio State University ElectroScience Laboratory, Department of Electrical Engineering; prepared under Contract MDA 904-79-C-0407 for Maryland Procurement Office, Fort George G. Meade, Maryland.
29. D.B. Hodge, "Scattering by Circular Metallic Disks," IEEE Trans. Antennas and Propagation, Vol. AP-28, September 1980, pp. 707-712.
30. C.E. Ryan and L. Peters, "Evaluation of Edge-Diffracted Fields Including Equivalent Currents for the Caustic Regions," IEEE Trans. Antennas and Propagation, Vol. AP-17, May 1969, pp. 292-299.
31. F. Sikta, personal communication.
32. H.D. Weinschel, "A Cylindrical Array of Circularly Polarized Microstrip Antenna," IEEE Group on Antennas and Propagation, International Symposium, June 1975, pp. 177-180.
33. Proceedings of the Workshop on Printed Circuit Antenna Technology, New Mexico State University, Las Cruces, New Mexico, October 17-19, 1979.
34. G.A. Deschamps, "Microstrip Microwave Antennas," presented at the Third USAF Symposium on Antennas, 1953.

35. J.Q. Howell, "Microstrip Antennas," IEEE Group on Antennas and Propagation, International Symposium, December 1972, pp. 177-180.
36. J.Q. Howell, "Microstrip Antennas," IEEE Trans. Antennas and Propagation, Vol. AP-23, January 1975, pp. 90-93.
37. L.C. Shen, S.A. Long, M.R. Allerdig, and M.D. Walton, "Resonant Frequency of a Circular Disc, Printed-Circuit Antenna," IEEE Trans. Antennas and Propagation, Vol. AP-25, July 1977, pp. 595-596.
38. R.E. Munson, "Conformal Microstrip Antennas and Microstrip Phased Arrays," IEEE Trans. Antennas and Propagation, Vol. AP-22, January 1974, pp. 74-78.
39. A.G. Derneryd, "Linearly Polarized Microstrip Antennas," IEEE Trans. Antennas and Propagation, Vol. AP-24, November 1976, pp. 846-851.
40. A.G. Derneryd, "A Theoretical Investigation of the Rectangular Microstrip Antenna Element," IEEE Trans. Antennas and Propagation, Vol. AP-26, July 1978, pp. 532-535.
41. S.A. Long, L.C. Shen, and P.B. Morel, "Theory of the Circular Disc Printed-Circuit Antenna," Proceedings of the IEE, Vol. 125, October 1978, pp. 925-928.
42. A.G. Derneryd, "Analysis of the Microstrip Disk Antenna Element," IEEE Trans. Antennas and Propagation, Vol. AP-27, September 1979, pp. 660-664.
43. A.G. Derneryd and A.G. Lind, "Extended Analysis of Rectangular Microstrip Resonator Antennas," IEEE Trans. Antennas and Propagation, Vol. AP-27, November 1979, pp. 846-849.
44. Y.T. Lo, D. Solomon, and W.F. Richards, "Theory and Experiment on Microstrip Antennas," IEEE Trans. Antennas and Propagation, Vol. AP-27, March 1979, pp. 137-145.
45. K.R. Carver and E.L. Coffey, "Theoretical Investigation of the Microstrip Antenna," Technical Report No. PT-00929, January 1979, Physical Science Laboratory, New Mexico State University; prepared under ARO Grant DAAG29-78-G-0082 for the Army Research Office, Research Triangle Park, Durham, North Carolina.
46. P.K. Agrawal and M.C. Bailey, "An Analysis Technique for Microstrip Antennas," IEEE Trans. Antennas and Propagation, Vol. AP-25, November 1977, pp. 756-759.
47. E.H. Newman and P. Tulyathan, "Wire Antennas in the Presence of a Dielectric/Ferrite Inhomogeneity," IEEE Trans. Antennas and Propagation, Vol. AP-26, July 1978, pp. 587-593.

48. J.H. Richmond and E.H. Newman, "Dielectric Coated Wire Antennas," *Radio Science*, Vol. 11, January 1976, pp. 13-20.
49. E.H. Newman, "Strip Antennas in a Dielectric Slab," *IEEE Trans. Antennas and Propagation*, Vol. AP-26, September 1978, pp. 647-653.
50. N.K. Uzunoglu, N.G. Alexopoulos, and J.G. Fikioris, "Radiation Properties of Microstrip Dipoles," *IEEE Trans. Antennas and Propagation*, Vol. AP-27, November 1979, pp. 853-858.
51. Schneider, M.V., "Microstrip Dispersion," *Proceedings of the IEEE*, Vol. 60, January 1972, pp. 144-146.
52. J.H. Richmond, personal communication.
53. E. Weber, Electromagnetic Theory, Static Fields and Their Mapping, New York: Dover Publications, Inc., 1965.
54. P. Silvester, "TEM Wave Properties of Microstrip Transmission Lines," *Proceedings of the IEE*, Vol. 115, January 1968, pp. 43-48.
55. C.M. Kaloi, "Microstrip Antennas, Design Equations," *IEEE Group on Antennas and Propagation, International Symposium*, June 1979, pp. 122-125.

APPENDIX A

EFFICIENT EVALUATION OF PWS FILAMENT-TO-FILAMENT IMPEDANCE

The mutual impedance between filamentary monopoles with PWS currents can be evaluated from the rigorous closed form expression [22] or numerical integration. Reference [22] refers to subroutine GGMM which can be used to compute the mutual impedance of general skew PWS filamentary monopoles with complex propagation constant, γ , (i.e. lossy homogenous medium). If free space is assumed, then γ becomes pure imaginary and some of the exponential integrals in expression for the mutual impedance reduce to cosine integrals which are simpler to evaluate. A subroutine with this simplification [52] is used in this work when the exact mutual impedance is needed. Since the near field expression from a PWS filament is known, only a one-dimensional integration (on the expansion filament) is required to evaluate the mutual impedance. For parallel filaments, the computation time required for the exact evaluation and numerical integration (INT=2) is about the same, but the latter is not accurate at very small filament separation. Although numerical integration is also less accurate than the exact evaluation when two nonparallel filaments are close to each other, it is much faster. For the nonparallel case, a five-point (INT=4) and three-point (INT=2) Simpson rule integration is about twice and three times faster than the exact evaluation (INT=0), respectively.

A simple test to decide on the type of integration (for the nonparallel case) is to find the distance between the midpoints of the two filaments (D_m) and use the following decision rule:

$$\begin{array}{lll} D_m > 0.25\lambda & \text{use} & \text{INT}=2 \\ D_m \leq 0.25\lambda & \text{use} & \text{INT}=0. \end{array}$$

However, even within the $D_m < 0.25\lambda$ radius there are many filament orientations which require only INT=2. The following describes a more stringent test which can substantially reduce the overall computation time. Figure 55 shows the reactances and computation times using INT=0, INT=2 and different INT's chosen by the following decision rule.

Figure 56 shows two filamentary monopoles, M and N, with endpoints 1, 2 and A, B, respectively. Assuming that M and N are not parallel, the minimum distance, D_{min} , between the two filaments are determined by one of the following:

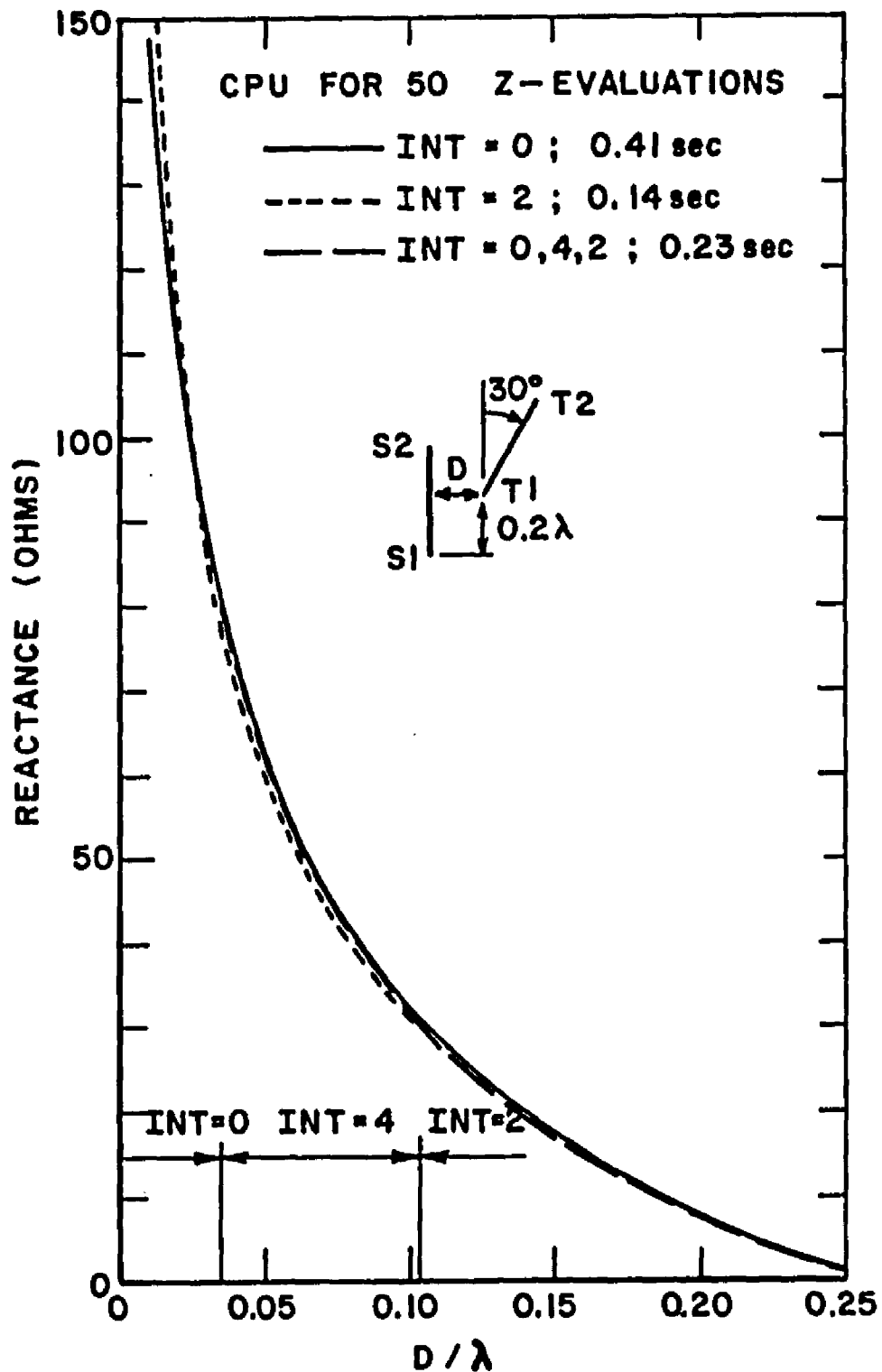


Figure 55. Reactance of two PWS filamentary monopoles. The lengths of the filaments are 0.25λ . S1 and S2 denote the terminal and end points of the test monopole, respectively. T1 and T2 denote the terminal and end points of the expansion monopole, respectively.

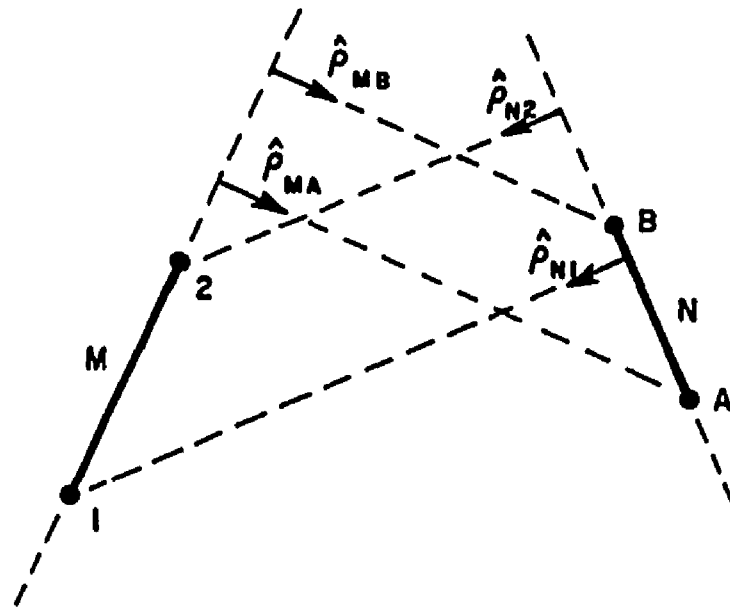


Figure 56. The geometry used to find the smallest distance between two filaments.

- a. If $\hat{\rho}_{MA} \cdot \hat{\rho}_{MB} < 0$ and $\hat{\rho}_{N1} \cdot \hat{\rho}_{N2} < 0$, then the filaments cross each other. D_{min} is the perpendicular distance between the two parallel planes formed by the two filaments.
- b. If $\hat{\rho}_{MA} \cdot \hat{\rho}_{MB} < 0$ and $\hat{\rho}_{N1} \cdot \hat{\rho}_{N2} \geq 0$, then D_{min} is the minimum value of $(|\hat{\rho}_{N1}|, |\hat{\rho}_{N2}|)$.
- c. If $\hat{\rho}_{N1} \cdot \hat{\rho}_{N2} < 0$ and $\hat{\rho}_{MA} \cdot \hat{\rho}_{MB} \geq 0$, then D_{min} is the minimum value of $(|\hat{\rho}_{MA}|, |\hat{\rho}_{MB}|)$.
- d. If $\hat{\rho}_{MA} \cdot \hat{\rho}_{MB} \geq 0$ and $\hat{\rho}_{N1} \cdot \hat{\rho}_{N2} \geq 0$, then D_{min} is the minimum of the distances from points 1 to A, 1 to B, 2 to A, and 2 to B.

D_{min} is then used in the following decision rule:

$0 \leq D_{min} \leq 0.03\lambda$	choose	INT=0
$0.03\lambda < D_{min} \leq 0.1\lambda$	choose	INT=4
$D_{min} > 0.1\lambda$	choose	INT=2.

APPENDIX B

EVALUATION OF R BY THE METHOD OF DIELECTRIC IMAGES

The assymetry of D_1 and D_2 (see Figures 49 and 50) due to the dielectric slab is accounted for by a constant R. This constant is the ratio of two average values:

$$R = \frac{\iiint_{V_2} E_n^{dz} \cdot E_m^Z dv}{\iiint_{V_2} E_n^Z \cdot E_m^Z dv} \quad (56)$$

where E_n^{dz} and E_n^Z are the fields of the n^{th} expansion mode evaluated in the presence of the dielectric slab and free-space, respectively. E_m^Z is the field from the m^{th} test mode evaluated in free space. V_2 is the common volume shared by the modes m and n . For electrically thin dielectric slab, the fields are constant along the z -coordinate and the integrals in Equation (56) reduce to surface integrals. In practice, the surface integration is done inside V_2 and close to the surface of the m^{th} mode. Note that the integrals in Equation (56) are the same as those used to determine Δz_{mn} in Equation (41).

Since R is a ratio of the field averages, the static approximation is used to calculate these fields. Consider a finite line charge, as shown in Figure 57, with a uniform charge distribution of density Q/h . The potential distribution of this line charge is [53, p. 107]

$$\phi = \frac{1}{4\pi\epsilon} \frac{Q}{h} \left[\ln \left(\frac{U + r_{2n}}{U - h + r_{2n}} \right) \right] \quad (57)$$

$$\text{where } r_{1n} = \sqrt{(x-x_1)^2 + (y-y_1)^2 + (z+2nd)^2}$$

$$r_{2n} = \sqrt{(x-x_2)^2 + (y-y_2)^2 + (z+2nd)^2}$$

n are the intergers (... -2, -1, 0, 1, 2, ...)

d is the dielectric thickness ($2T$)

U is the distance from (x_2, y_2, z_2) to the projection of (x, y, z) on to the line formed by extending the line charge, i.e.:

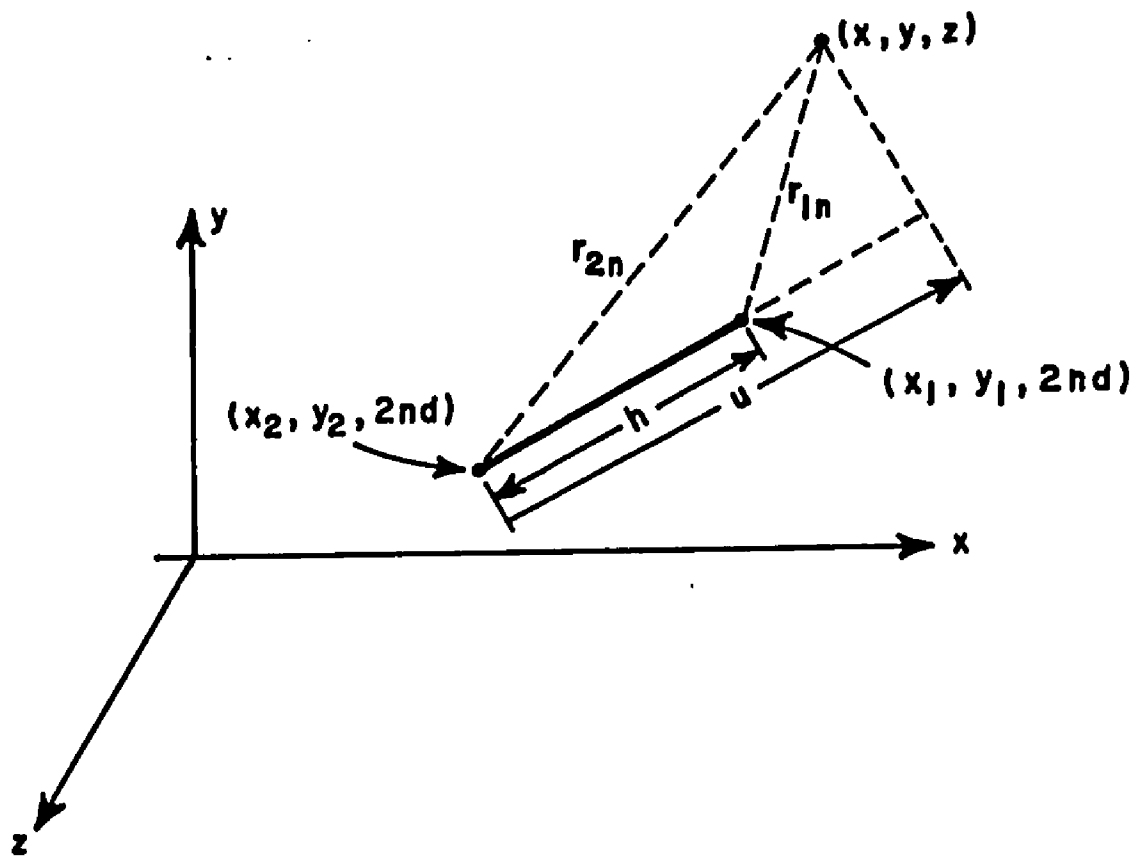


Figure 57. A line charge, Q , with the associated coordinates.

$$\begin{aligned}
 U &= (x-x_2) * CAS + (y-y_2) * CBS + (z-z_2) * CGS \\
 CAS &= (x_1-x_2)/h \\
 CBS &= (y_1-y_2)/h \\
 CGS &= (z_1-z_2)/h.
 \end{aligned}$$

E^z is found by:

$$\begin{aligned}
 E^z &= -\frac{\partial}{\partial z} \phi \\
 &= \frac{-1}{4\pi\epsilon} \frac{Q_n}{h} \left[\frac{z+2nd}{(U+r_{2n})r_{2n}} - \frac{z+2nd}{(U-h+r_{1n})r_{1n}} \right] \quad (58)
 \end{aligned}$$

Equation (58) is the expression for E^z from a line charge and can be integrated to find the field of a surface charge E_m^z and E_n^z . Note that Equation (56) is used only when V_2 is the common area shared only by a monopole from each mode m and n . If both monopoles of modes m and n overlap, then E^z must be the field from a dipole with $+Q$ on one monopole and $-Q$ on the other. The field from a line charge $-Q$ can be found by the same method outlined above and this is added to Equation (58) to form the field from a dipole. The fields of the line charges are integrated to find the field due to a surface charge.

E^z due to a surface charge radiating in a homogenous medium with permittivity ϵ has been derived. The method of dielectric images [54] is now used to find E_n^z , the field in the presence of a dielectric slab. Figure 58 shows the images of a charge Q close to a dielectric slab and the regions in which the equivalent images are applicable. That is, if the field point is in a region, then the fields from the images (applicable to that particular region) are added. This technique was also used to generate the relative D_z in Figure 50.

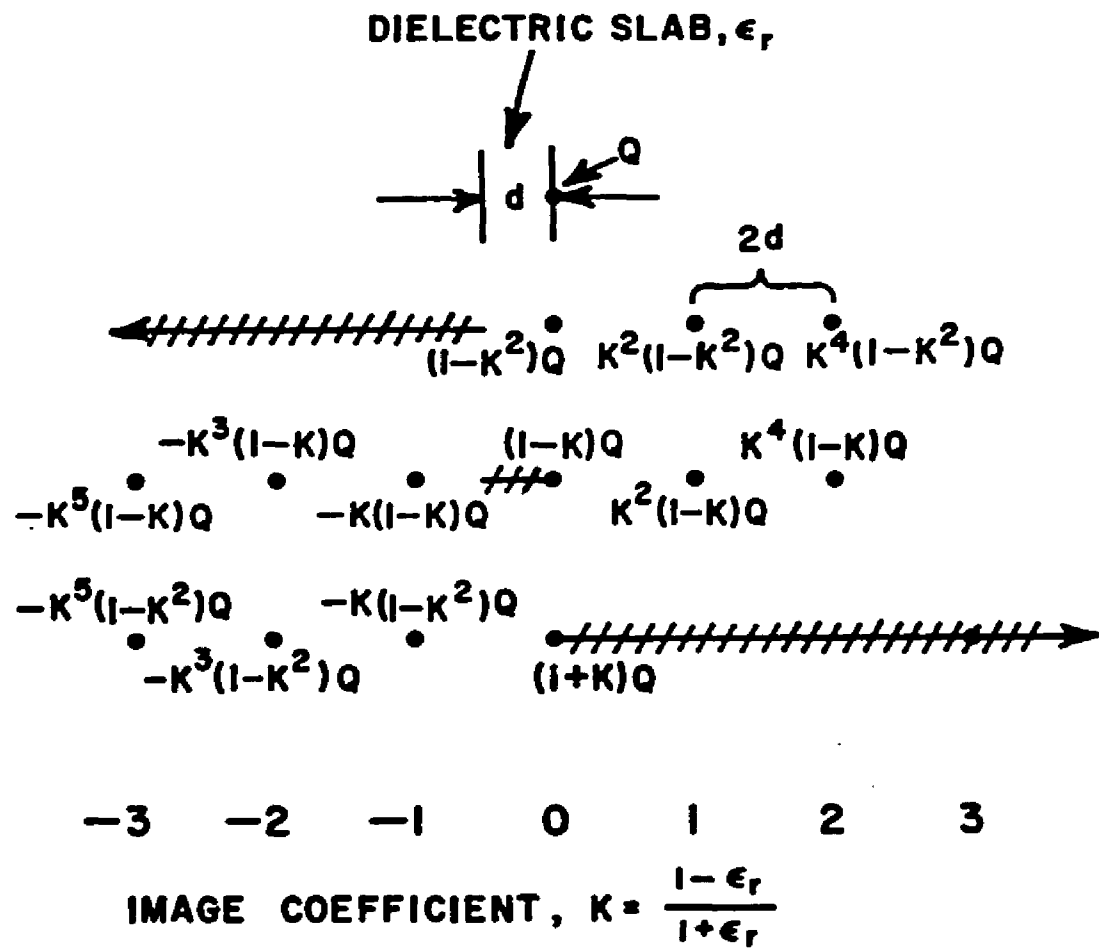


Figure 58. The images of a charge, Q , located near a dielectric slab.

APPENDIX C

BASIC APPROACHES USED IN SUBDIVISION METHODS 1 AND 2

The rectangle is the simplest shape that can be subdivided into rectangular surface-patch modes which satisfy all the criteria given in Chapter Three. Determination of the set of modes for a rectangular plate like the one shown in Figure 59 is the motivation for the general approach used in subdivision methods 1 and 2. The rectangular is first divided into long strips (Figure 60) and these strips are then sectioned to form rectangular blocks (Figure 61). These small blocks become the monopoles of the overlapping PWS surface-patch modes.

A general polygon can be subdivided in a similar manner. The polygon is first divided into trapezoidal strips. These strips are then divided into blocks. It is the strategies used to subdivide the strips in which method 1 differs from method 2. In method 1, all the strips are divided into the same number of blocks and, thus, generate a grid for the two current polarizations as shown in Figures 16 and 18. Realizing that the shorter strips do not require as many blocks as the longer strips, method 2 segments each strip by a minimal number of blocks. Also, the sides of the blocks that do not coincide with the plate boundary are manipulated so that these blocks can become rectangular blocks. In this way, subdivision method 2 can generate a large percent of rectangular modes and this becomes more evident in electrically large plates. Examples of mode layout using subdivision method 2 are shown in Figures 23, 34, 38, and 39. Both subdivision schemes are discussed in more detail in Chapter Three.

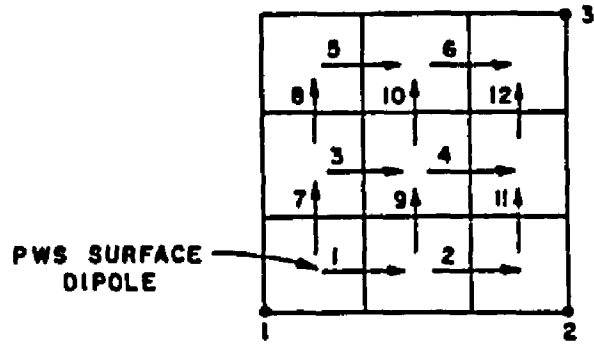


Figure 59. Overlapping surface-patch dipole layout on a rectangular plate.

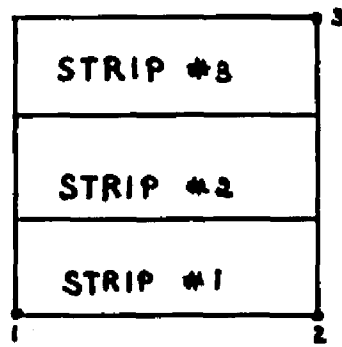


Figure 60. A rectangle divided into strips.

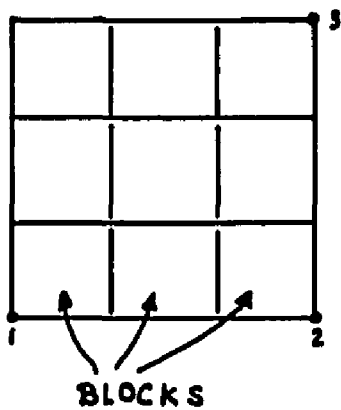


Figure 61. A rectangle divided into strips and then into blocks.